AFRL-PR-WP-TR-2003-2011

DEVELOPMENT OF MICRO HEAT PIPES EMBEDDED IN LAMINATE SUBSTRATES FOR ENHANCED THERMAL MANAGEMENT (TM) FOR PRINTED WIRING BOARDS (PWBs)

K. Jones
Y. Cao
M. Gao

Florida International University
Department of Mechanical Engineering
EAS 3462 University Park
Miami, FL 33199

JUNE 2002

Final Report for 03 May 2000 – 31 May 2002

Approved for public release; distribution is unlimited.

PROPULSION DIRECTORATE
AIR FORCE RESEARCH LABORATORY
AIR FORCE MATERIEL COMMAND
WRIGHT-PATTERSON AIR FORCE BASE, OH 45433-7251

NOTICE

USING GOVERNMENT DRAWINGS, SPECIFICATIONS, OR OTHER DATA INCLUDED IN THIS DOCUMENT FOR ANY PURPOSE OTHER THAN GOVERNMENT PROCUREMENT DOES NOT IN ANY WAY OBLIGATE THE US GOVERNMENT. THE FACT THAT THE GOVERNMENT FORMULATED OR SUPPLIED THE DRAWINGS, SPECIFICATIONS, OR OTHER DATA DOES NOT LICENSE THE HOLDER OR ANY OTHER PERSON OR CORPORATION; OR CONVEY ANY RIGHTS OR PERMISSION TO MANUFACTURE, USE, OR SELL ANY PATENTED INVENTION THAT MAY RELATE TO THEM.

THIS REPORT IS RELEASABLE TO THE NATIONAL TECHNICAL INFORMATION SERVICE (NTIS). AT NTIS, IT WILL BE AVAILABLE TO THE GENERAL PUBLIC, INCLUDING FOREIGN NATIONS.

THIS TECHNICAL REPORT HAS BEEN REVIEWED AND IS APPROVED FOR PUBLICATION.

Brian D. Donovan

BRIAN D. DONOVAN
Mechanical Engineer
Energy Storage & Thermal Sciences Branch

Brian G. Hager

BRIAN G. HAGER
Chief
Energy Storage & Thermal Sciences Branch

Richard T. Fingers, PhD
Deputy Chief
Power Division

Do not return copies of this report unless contractual obligations or notice on a specific document requires its return.

REPORT DOCUMENTATION PAGE

Form Approved
OMB No. 0704-0188

The public reporting burden for this collection of information is estimated to average 1 hour per response, including the time for reviewing instructions, searching existing data sources, searching existing data sources, gathering and maintaining the data needed, and completing and reviewing the collection of information. Send comments regarding this burden estimate or any other aspect of this collection of information, including suggestions for reducing this burden, to Department of Defense, Washington Headquarters Services, Directorate for Information Operations and Reports (0704-0188), 1215 Jefferson Davis Highway, Suite 1204, Arlington, VA 22202-4302. Respondents should be aware that notwithstanding any other provision of law, no person shall be subject to any penalty for failing to comply with a collection of information if it does not display a currently valid OMB control number. **PLEASE DO NOT RETURN YOUR FORM TO THE ABOVE ADDRESS**.

1. REPORT DATE *(DD-MM-YY)*	2. REPORT TYPE	3. DATES COVERED *(From - To)*
June 2002	Final	05/03/2000 – 05/31/2002

4. TITLE AND SUBTITLE
DEVELOPMENT OF MICRO HEAT PIPES EMBEDDED IN LAMINATE SUBSTRATES FOR ENHANCED THERMAL MANAGEMENT (TM) FOR PRINTED WIRING BOARDS (PWBs)

5a. CONTRACT NUMBER
F33615-99-1-2973

5b. GRANT NUMBER

5c. PROGRAM ELEMENT NUMBER
62173C

6. AUTHOR(S)
K. Jones
Y. Cao
M. Gao

5d. PROJECT NUMBER
1660

5e. TASK NUMBER
03

5f. WORK UNIT NUMBER
00

7. PERFORMING ORGANIZATION NAME(S) AND ADDRESS(ES)
Florida International University
Department of Mechanical Engineering
EAS 3462 University Park
Miami, FL 33199

8. PERFORMING ORGANIZATION REPORT NUMBER

9. SPONSORING/MONITORING AGENCY NAME(S) AND ADDRESS(ES)
Propulsion Directorate
Air Force Research Laboratory
Air Force Materiel Command
Wright-Patterson Air Force Base, OH 45433-7251

10. SPONSORING/MONITORING AGENCY ACRONYM(S)
AFRL/PRPS

11. SPONSORING/MONITORING AGENCY REPORT NUMBER(S)
AFRL-PR-WP-TR-2003-2011

12. DISTRIBUTION/AVAILABILITY STATEMENT
Approved for public release; distribution is unlimited.

13. SUPPLEMENTARY NOTES

14. ABSTRACT *(Maximum 200 Words)*
The objective of this work is the development of a process to fabricate an axial grooved heat pipe embedded in printed wiring board (PWB) technology and to evaluate is thermal, mechanical performance, and reliability. The results clearly show that the embedded heat pipe was operable and the heat transfer through the substrate was enhanced. However, the heat pipe was limited in the power input it could handle, as heat pipe failure occurred around 10 W by delamination of the PWB and subsequent loss of hermeticity and loss of the working fluid. After failure occurs, the heat pipe begins to behave as an uncharged heat pipe for the corresponding input the whole PWB starts increasing until it reaches the temperature distribution of the uncharged heat pipe for the corresponding input power. The development of a hermetic structure within the channel structure. Since the operation of the wick in the heat pipe is strongly dependent on the ability of the working fluid to wet the wick, the wetting angle of the plating material was measured for the various materials options available (bare laminate, copper plating, other plating). The physical structure of the embedded heat pipes was analyzed by finite element analysis (FEA). The FEM results were compared with the experimental data to determine failure mode.

15. SUBJECT TERMS
Ceramic Heat Pipes, Electronic Cooling, Heat Pipe Fabrication, Liquid Charging, Heat Transfer

16. SECURITY CLASSIFICATION OF:			17. LIMITATION OF ABSTRACT:	18. NUMBER OF PAGES	19a. NAME OF RESPONSIBLE PERSON (Monitor)
a. REPORT	b. ABSTRACT	c. THIS PAGE			Brian Donovan
Unclassified	Unclassified	Unclassified	SAR	128	19b. TELEPHONE NUMBER *(Include Area Code)* (937) 255-5735

Standard Form 298 (Rev. 8-98)
Prescribed by ANSI Std. Z39-18

TABLE OF CONTENTS

TABLE OF CONTENTS (CONTINUED)

Section Page

LIST OF FIGURES

Figure Page

LIST OF FIGURES

Figure Page

LIST OF FIGURES

Figure Page

LIST OF TABLES

Table Page

LIST OF SYMBOLS

SYMBOL	DESCRIPTION	UNITS
D_g	Groove depth	m
$D_{l,h}$	Hydraulic diameter of the liquid groove	m
$D_{v,h}$	Hydraulic diameter of the vapor space	m
F_l	Liquid frictional coefficient	
F_v	Vapor frictional coefficient	
f	Skin-friction coefficient	
h_{fg}	Latent heat of evaporation	J/kg
K_g	Permeability of the wick structure	m^2
L_a	Adiabatic section length	m
L_c	Condenser section length	m
L_e	Evaporation section length	m
L_{eff}	Effective length	m
N_g	Number of grooves	
Q	Input power	W
Q_{CAP}	Capillary Limit	W
$Re_{l,h}$	Hydraulic liquid Reynolds number	
$Re_{v,h}$	Hydraulic vapor Reynolds number	
S_g	Groove spacing	m
t_v	Vapor space height	m
W_v	Vapor space width	m
μ	Dynamic viscosity	kg/m-s
υ	Kinematic viscosity	m^2/s
ρ	Density	Kg/m^3
σ	Surface tension	N/m
ϕ	Porosity of the wick structure	
A_o	Original tensile specimen cross-sectional area	in^2
E	Modulus of elasticity	lb_f/in^2
P_y	Yield load	lb_f
P_f	Fracture load	lb_f
σ_y	Yielding strength	lb_f/in^2
σ_f	Fracture strength	lb_f/in^2
$\Delta\epsilon$	Change in strain	
$\Delta\sigma$	Change in stress	lb_f/in^2

Section 1

1.0 Executive Summary

The objective of this work is the development of a process to fabricate an axial grooved heat pipe embedded in printed wiring board (PWB) technology and to evaluate its thermal, mechanical performance, and reliability. The results clearly show that the embedded heat pipe was operable and the heat transfer through the substrate was enhanced (see section 3). However, the heat pipe was limited in the power input it could handle, as heat pipe failure occurred around 10 W by delamination of the PWB and subsequent loss of hermeticity and loss of the working fluid. The failure was detected visually. After failure occurs, the heat pipe begins to behave as an uncharged heat pipe. The temperatures in the whole PWB starts to increase until it reaches the temperature distribution of the uncharged heat pipe for the corresponding input power.

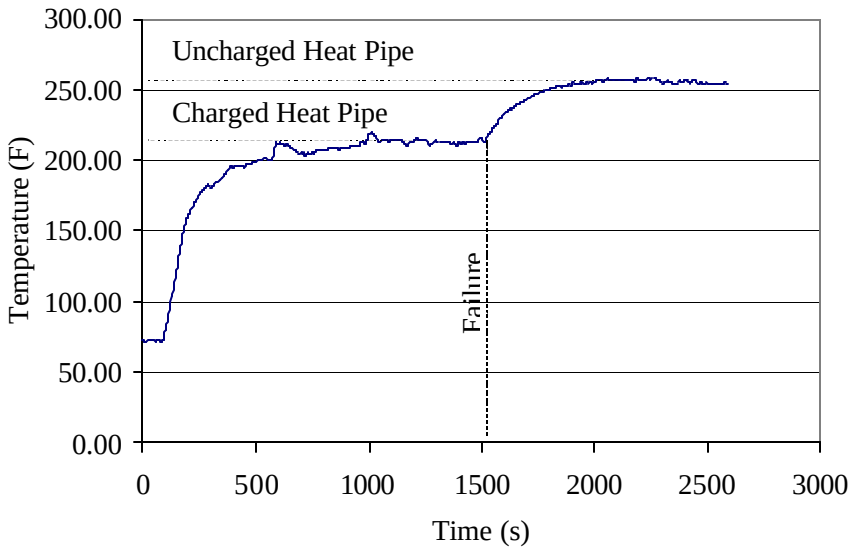

Temperature behavior after failure at point T1.

The development of a hermetic structure within the heat pipe structure to contain the working fluid required development of a plating system that allows plating within the channel structure. Since the operation of the wick in the heat pipe is strongly dependent on the ability of the working fluid to wet the wick, the wetting angle of the plating material was measured for the various materials options available (bare laminate, copper plating, other plating). After the copper plating the wetting angle of the inner surface of the embedded heat pipe has been reduced from 104 degrees (FR404 Epoxy with DI water) to 56 degrees (plated copper with DI water).

Plating chemistries are available from the PWB industry including both electroless and electroplating solutions. To accomplish this, a microplating system was fabricated which pumped plating solutions thru the microchannel from a recirculating chamber. The microplating container was designed, with control on flow speed and anode position. Additionally, the pumping mechanism was chosen to ensure the fluid in the microchannel is not electrically isolated from the plating container. Five configurations of plating cells/ structures were evaluated.

The mechanical properties of the copper plated film was determined by tensile testing as these properties were required to model the mechanical performance (i.e. thermally induced stresses and strains) over the environmental stress exposure. The approach to measuring the stress-strain curve is similar to the standardized ASTM E 345-86. The electrodeposited copper, which is 4.7 mils thick, has brittle material behavior. The

copper tested here shows that the initial elastic portion of the stress-strain curve is not linear and to determine the modulus of elasticity the secant modulus method was used.

The modulus of elasticity measured perpendicular to the deposition direction is 5720 ksi, which is lower than the typical material value (16700 ksi). It has a large standard deviation (13 %).

The yield strength (12.946 ksi) and percent of elongation (48) are very close to the typical material values (10 ksi and 45 respectively). The typical material value is a factor of two larger than the fracture strength.

Comparison of results from tensile test and typical properties

	E (psi)	**s_y (psi)**	**s_f (psi)**	**Elongation (%)**
Experimental Properties	5.720×10^6	12946	16775	48
Typical Properties	16.7×10^6	10000	34075	45

The results of tension tests from selected portions of the electrodeposited copper material may not totally represent the strength and ductility of the entire plated surface of the embedded heat pipe of its in-service behavior in different environment.

The physical structure of the embedded heat pipes was analyzed by finite element analysis (FEA). (see section 4) Figure 4. 12 to Figure 4.17 compare the FEM results with the experimental data. The thermal-stress finite element analysis of the embedded heat pipe resulted in data that provide information of the strain and stress generated in the substrate for different level of input power at different points along the heat pipe, with

this information the temperature, stress, and location were the heat pipe could fail is inferred.

1.1 Overview of Micro Heat Pipe Technology

Thermal management is becoming a limiting factor in system applications due to the increased power of semiconductor device. The Semiconductor Industries Association (SIA) roadmap projects operating power level of advanced microprocessors at over 200 W/die by 2005. This is further compounded by the increased complexity at the system level and the development of new high power technologies, such as SiC, which are projected to operate at power levels far exceeding current devices. These requirements are placing thermal demands that cannot be handled by current technology or require technologies that add great cost and weight at the system level.

To provide thermal management for high heat dissipating devices mounted on laminate boards when air-cooling is not an option requires that a conduction path for the dissipated heat must be provided directly from the device to the sink. For power devices, this is typically accomplished by bonding a metal heat sink to the circuit card and mounting the component directly on the heat sink. For the heat sinks to work adequately, the heat sinks are usually 3 mm thick or greater, and need to be machined and finished and the heat path still must travel down the length of the heat pipe to the thermal sink unless direct fluid cooling is used. With the project heat fluxes of new high power components, conduction thermal paths will not be able to handle the thermal loads without incurring a large temperature rise from the component to the heat sink.

Previous works in Florida International University has addressed the need for system level integration of thermal management tools by the development of micro heat pipes fabricated within a ceramic co-fired interconnect substrate. Micro heat pipes, capable of transporting large amounts of heat (40 W) over relative long distances (10 cm demonstrated) have been fabricated in both high temperature alumina and low temperature cofire ceramic (HTCC and LTCC). The heat pipe was found to have an effective thermal conductivity greater than 10,000 W/m-°K, approximately five times than diamond and over 1000 times higher than the ceramic it replaced within the substrate. This allows an entirely new set of thermal management options in a technology, such as LTCC, where the thermal conductivity of the material is less than 4 W/m-°K.

Heat pipes are designed to transport heat over relatively long distances with no additional input power (i.e. passive function). A heat pipe consists of a sealed, hermetic enclosure, with three distinct regions: an evaporator, a condenser, and an adiabatic region separating these two regions. The enclosure contains a working fluid, which absorbs heat by evaporation at the evaporator, travels as a vapor in the adiabatic region to the condenser, where the heat is removed. The working fluid returns to the evaporator section by the capillary action of a wick structure. The total heat energy (W or J/s) that the pipe could transport relates to the heat of vaporization (J/kg) and the amount of fluid undergoing evaporation (kg/s). The heat pipe used an axially grooved wick structure to provide transport of the working fluid from the condenser to the evaporator. The design of the wick is the most critical aspect to insure high fluid transport and thus high heat transport

capability. Different designs of wicks have been developed by researchers, the most common types of homogeneous wicks included wrapped screen, sintered metal, and small axial grooves along the inner walls of the heat pipe [1].

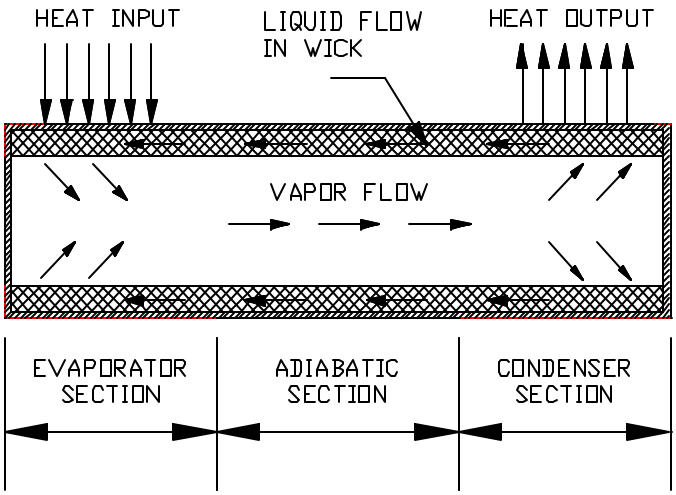

Figure 1.1 Heat pipe structure and operation.

Initial efforts in the ceramic heat pipes used water as the working fluid, although other working fluids are also available based on the desired operating temperature and other systems requirements [2].

The most significant limiting factor in the power handling capability of miniature heat pipes is the capillary limit, which is the point at which the wick cannot deliver working fluid at the same rate at which it is evaporated. This condition leads to evaporator dry-out, indicated by a rapid increase in the local temperature of the evaporator. The capillary limit is a function of the surface tension of the working fluid and the frictional forces caused by the interaction of the working fluid with the wick material and with the opposing vapor flow. For axially grooved heat pipes, the capillary limitation has been

well developed by others [3], and has been reviewed for miniature embedded heat pipes by [4].

The design of an optimized miniature heat pipe for the thermal management of electronics involves a complex balance of system requirements, and the thermophysics of heat pipes, which involve capillary forces, phase change, two-phase flow interaction, and porous media and/or channel, flow. The relevant issues will be discussed starting from the evaporator end of the heat pipe where the heat is generated, and will end at the condenser end where heat is removed.

1.1.1 The Capillary Limit

To understand the capillary limitation with respect to both width (W_g) and depth (D_g) of straight rectangular grooves for a given internal height and width of the housing, it is opportune to refer to the following analysis developed by Zampino [2].

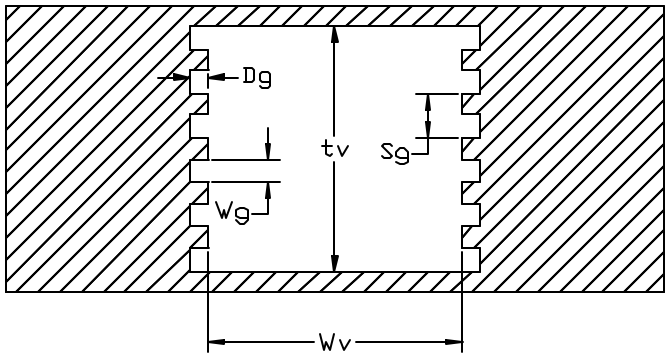

Figure 1.2 Heat pipe cross section.

The capillary limit is a function of the surface tension of the working fluid and the frictional forces caused by the interaction of the working with the wick material and with the opposing vapor flow. For axially grooved heat pipes, the capillary limitation is given in Equation 1.1 [3], which relates the pumping action of the working fluid due to surface tension, σ, and the frictional forces, F_l and F_v, to flow of the working fluid from the condenser back to evaporator. The frictional forces are described by two components, F_l, which represents the interaction of the working fluid and the wick material (structure), and F_v, which represents the resistance to the vapor flow due to the geometry of the vapor space. L_{eff} is the effective length of the heat pipe, which is equal to $L_a + 0.5 (L_e + L_c)$.

$$Q_{CAP} = \frac{2s}{W_g L_{eff} (F_l + F_v)} \qquad (1.1)$$

The liquid and vapor frictional coefficient are given in Equations (1.2) and (1.3). Referring to Equation (1.2), it is seen that the permeability of the wick, K_g, is inversely proportional to the liquid frictional coefficient. A_w is the cross-sectional area of the wick structure. Referring to Equation (1.3), it is seen that the vapor frictional coefficient is proportional to the friction factor, $f(\mathrm{Re}\,vh)$ which is given in equation (1.7) [5].

$$F_l = \frac{m_l}{r_l A_w K_g h_{fg}} \qquad (1.2)$$

$$F_v = \frac{(f \mathrm{Re}_{v,h}) m_v}{2pR_{v,h}^4 r_v h_{fg}} \qquad (1.3)$$

The hydraulic diameter for the vapor flow space $D_{v,h}=2R_{v,h}$, and that of the axially grooved wick structure $D_{l,h}$, can be evaluated, respectively, by the following relations:

$$D_{v,h} = 2\, t_v W_v/(t_v + W_v) \qquad (1.4)$$

$$D_{l,h} = 4D_g W_g/(2D_g + W_g) \qquad (1.5)$$

The permeability of the axial grooved wick is given in Equation (1.6), which shows a ratio between the flow area and the friction to the flow. The friction factor, $(f\,\mathrm{Re}_{l,h})$, is determined using Equation (1.8) and (1.9) which include the shear stress interaction between the vapor flow and the liquid [6].

$$K_g = \frac{D_{lh}^2 f}{2(f\,\mathrm{Re}_{l,h})} \qquad (1.6)$$

where f can be calculated by $f = Wg / Sg$

$$(f\,\mathrm{Re}_{v,h}) = 24(1-1.3553a+1.9467a^2-1.7012a^3+0.9564a^4-0.2537a^5) \qquad (1.7)$$

where $a = W_v/t_v$, when $W_v < t_v$ or $a = t_v/W_v$, when $W_v > t_v$

$$(f\,\mathrm{Re}_{l,ho}) = 8D_g^2\left\{\frac{W_g^2}{4}\left[1+2\frac{D_g}{W_g}\right]^2\left[\frac{1}{3}-\frac{32W_g}{p^5 D_g}\tanh\left(p\,\frac{D_g}{W_g}\right)\right]\right\}^{-1} \qquad (1.8)$$

$$(f\,\mathrm{Re}_{l,h}) = \mathrm{Re}_{lho}\left\{1+N_g\,\frac{W_g^3}{6pD_{vh}^3}\mathrm{Re}_{vh}\,\frac{v_v}{v_l}\left[1-1.971\exp\left(\frac{-pD_g}{W_g}\right)\right]\right\} \qquad (1.9)$$

All the equations thus far show the paradox of miniature heat pipe design, that is, the heat transport capability is increased by increasing the flow rates of vapor and fluid, however, large flow rates through small channels leads to high frictional losses which decrease the heat transport. Hence, the optimization of the design parameters must be performed to

provide an efficient design. Insight into an optimal design can be gained by showing the effect of the groove depth, D_g, and width, W_g (see Figure 1.6), on the capillary limit as shown in Figure 1. 3. From this figure it is clear that an optimal groove width exists which is approximately the same for various groove depths (all other parameters held constant), and as the groove depth increases, so does the capillary limit.

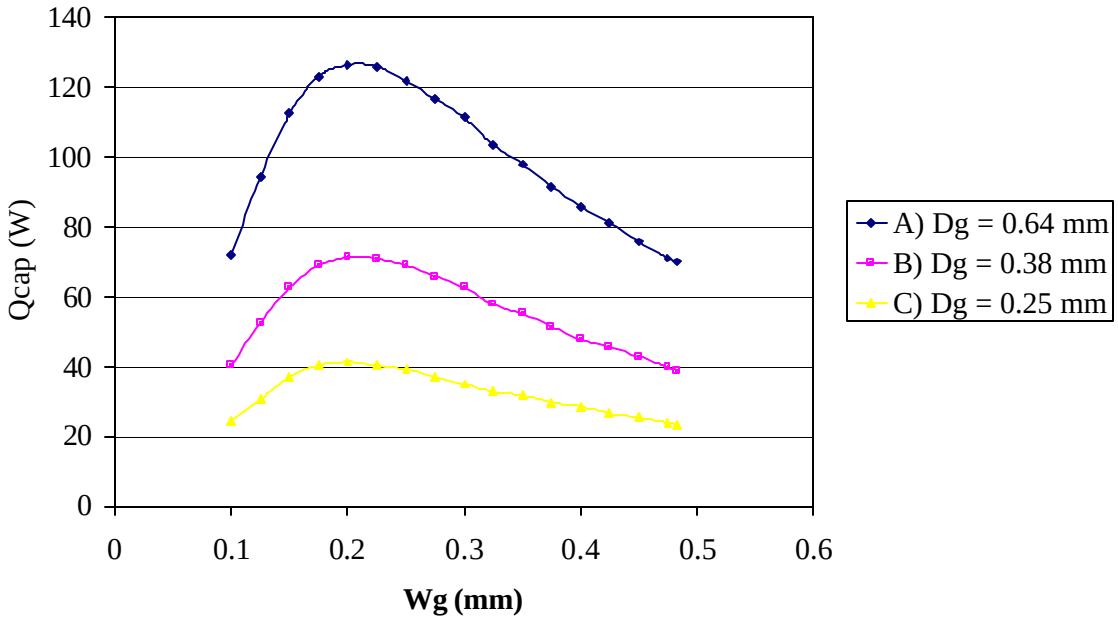

Figure 1. 3 The effect on the capillary limit due to variation in groove width for groove depths of: (A) 0.64 mm, (B) 0.38 mm, and (C) 0.25 mm.

In an effort to minimize the thickness of the heat pipe, it is desirable to minimize the height of the vapor space. The effect of the vapor space height is shown in Figure 1. 4, which shows that the capillary limit initially increases sharply with increasing vapor space height and then becomes relatively constant. Again, the effect of the groove depth is seen and follows the same trend as discussed for Figure 1. 3. An important conclusion drawn from the figure is that the minimum vapor space height is closely related with the

depth of the grooves, and that additional vapor space height will not have significant effect.

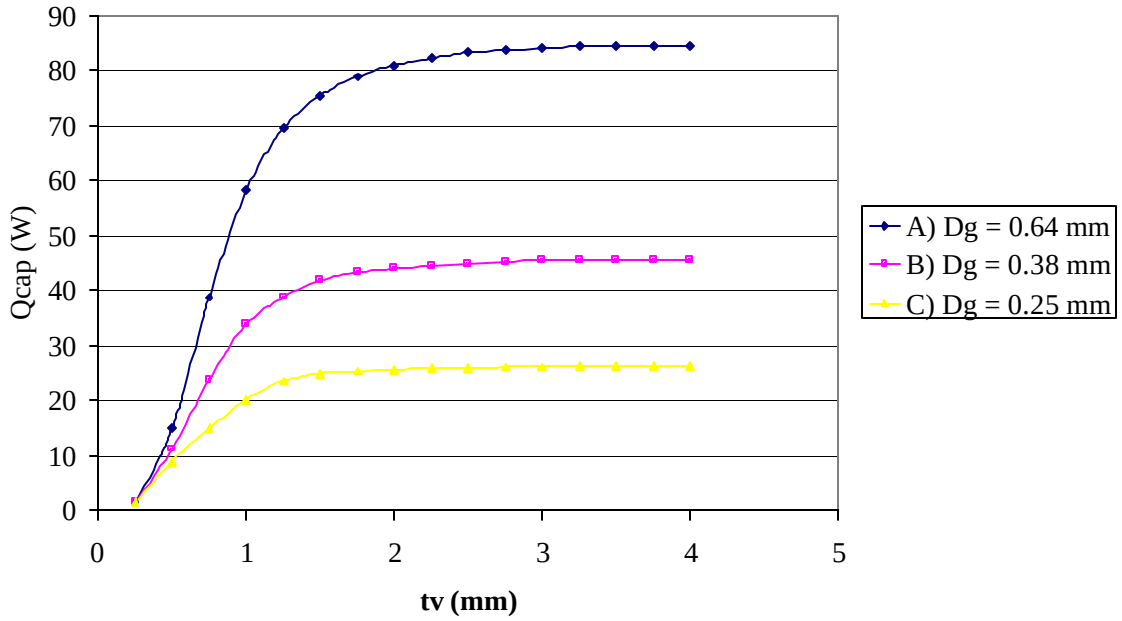

Figure 1. 4 The effect on the capillary limit due to variations in vapor space height for groove depths of: (A) 0.64 mm, (B) 0.38 mm, and (C) 0.25 mm.

The effect of the interaction between the groove width and the vapor space height is made clearer by holding the depth of the grooves constant and varying the other two parameter as shown in Figure 1. 5. The curves in the figure show that for small vapor space heights, smaller groove widths provide the highest capillary limit, but as the height of the vapor space increases, increases in the capillary limit are obtained with larger groove widths. The "crossing-over" effect shown by the curves indicates that there is a competition between the shear stress interaction between the vapor and liquid flows and the ability of the wick to provide adequate mass of working fluid.

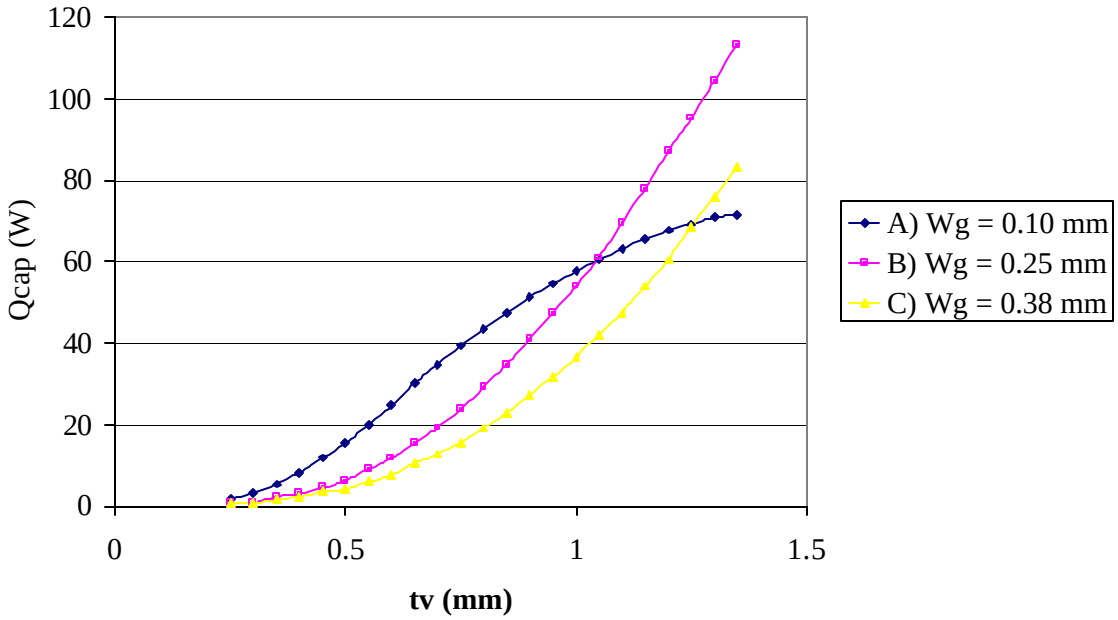

Figure 1. 5 The effect on the capillary limit due to variations in vapor space height for groove widths of: (A) 0.10 mm, (B) 0.25 mm, and (C) 0.38 mm.

Small vapor space heights cause greater shear stress interaction. Hence, only smaller groove widths can minimize the surface area of the working fluid interacting with the vapor flow. However, at some point, when vapor height exceed certain value the shear stress interaction will become negligible and the capillary limit becomes strongly dependent on the cross-sectional area through which the working fluid can flow.

1.1.2 Surface Tension and Surface Wetting

As discussed earlier, the operation of the wick in the heat pipe is strongly dependent on the ability of the working fluid to wet the wick. The better the working fluid wets the wick material, the greater the surface tension forces will be on the working fluid. The

capillary limit as described is a balance between the surface forces due to capillary action and the retarding forces due to gravity and friction. Therefore, any enhancement of the wick's surface that increases the wetting of the working fluid will increase the performance of the heat pipe.

The most basic model for determining the surface tension forces was introduced early in this century by Washburn and Rideal [7, 8] as

$$F_s = 2\pi r s \cos(\theta) \qquad (1.10)$$

This equation shows the relationship of the main parameter affecting the wetting of a fluid to a capillary groove, specifically, the size of the capillary, the surface tension, and the wetting angle. The capillary radius is mainly driven by the geometry of the heat pipe and the fabrication technologies used. Likewise, the selection of working fluid is limited to a few fluids that are compatible with the environmental requirements of the system. Therefore, the only parameter left which can be optimized is the wetting angle, which is a function of the working fluid and the heat pipe material selection. Again the selection of the heat pipe's material depends on the fabrication technologies employed and is limited. However, surface treatments can be employed to the selected materials to affect the wetting angle. Liquids such as water have relatively low wetting angles on materials such as gold (approximately 12 degrees). From equation 1.10 it can be seen that small wetting angles will increase the surface tension force.

An advantage that laminate technology has over ceramic is the wider choice of materials that can be plated. Ceramic technology, due to the need for high temperature firing, is limited to metal organics, which can be used to coat the channel. However, plating

compositions compatible with printing wiring board (PWB) technology include the precious metals (Au, Pt, Ag, Pd, Rh, etc.), metals such as Ni, Cr, Pb, Sn, Zn, etc., and their alloys. This provides a wide range of possible materials to optimize wetting performance in this technology.

As mentioned previously, the predominate technology for interconnect boards is laminate technology. This work considers extending the development of micro heat pipes into laminate interconnect board (printed wiring board). A major drawback of laminate technology is the inherent low thermal conductivity of the polymer laminate materials, typically in the range of 0.1 W/m^{o}K. This development will utilize the laminate structure of printed wiring boards to develop the wick structure.

The vapor space (t_v) for the heat pipe can be easily formed in the laminate stack by punching slots in each layer of material. Stacking several layers of laminate material with the slots cut into them forms a long rectangular duct within the substrate. The fabrication of the axial grooves for the wick structure is shown schematically in Figure 1.6.

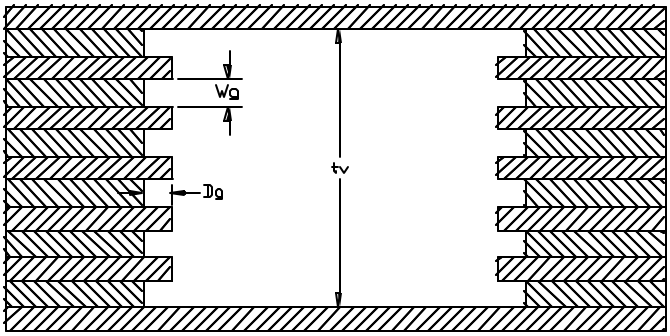

Figure 1.6 Schematic representation of heat pipe section showing axial groove construction

Axial grooves in the top and bottom interior surface of the heat pipe could be fabricated by numerically machining small grooves into the laminate layers of the top and bottom layers of the microchannel or plating up grooves in these copper coated laminate layers. The first process requires the use of micro end-mills and numerically controlled three axis machining system with a precision of at least 0.025 mm, while the second requires relatively thick plating structures with fine line resolution. In contrast, the fabrications of axial grooves in the sidewalls of the heat pipe are relatively easy. Varying the width of the rectangular slot cut into each laminate layer to form the vapor space forms these grooves. The variation in the width of the slots on alternating layers provides control over the depth (D_g) of grooves. However, the width (W_g) of each groove is dictated by the thickness of the tape layer. Fortunately, typical laminated material is 0.1 to 0.5 mm (0.004 to 0.020 in) in thickness, which allows for fine narrow grooves to be formed. Both types of grooves have been demonstrated in laminate construction in alumina co-

fire ceramic materials. However, the ease of manufacturing with sidewall grooves greatly reduces manufacturing cost with minimal performance impact.

The heat pipe will be assembled using patterned b-stage prepreg, which will be laminated using standard printed wiring board manufacturing processes. Initially, it is anticipated that the heat pipe will be manufactured at the completion of the PWB manufacturing (thru hole plating, solder mask, solder plating, OSP deposition, etc). It is envisioned that capture pads for the fill/scaling arrangement would be post drilled at both ends and the microchannel subsequently plated.

Section 2

Micro Heat Pipe Fabrication

The heat pipe is assembled using FR404 epoxy laminate layers and B15 prepreg bonding sheets, which is laminated using standard printed wiring board manufacturing processes. Initially, it is anticipated that the heat pipe will be manufactured at the completion of the PWB manufacturing (thru hole plating, solder mask, solder plating, OSP deposition, etc.). It is envisioned that capture pads for the charging/sealing arrangement would be post drilled at both ends and the micro channel subsequently plated.

Figure 2.1 shows the cross sectional view of the side walled grooved laminate heat pipe. The side walled grooves for the heat pipe are formed in the laminate stack by punching slots in each laminate layer of FR404 material. Stacking several layers of laminate material with the slots cut into them forms a long rectangular duct within the laminate

substrate. Varying the width of the rectangular slot cut into each layer to form the vapor space for these grooves. Variation in the width of the slots on alternating layers provides control over the depth (D_g) of the grooves. The width (W_g) of the grooves is controlled by the thickness of the tape layers (see Figure 2.1). The FR404 epoxy laminate layers with the slots cut into them were bonded together during lamination process by B15 prepreg bonding sheet to form the heat pipe.

Fabrication of the heat pipe involves critical steps including etching, lamination, electroplating, and fluid charging.

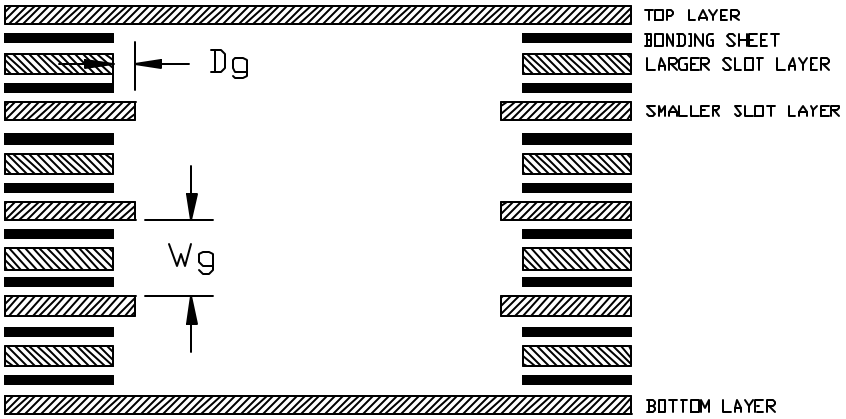

Figure 2.1 Laminate layers setup.

The laminate layers itself and its rectangular slots were cut using a numerically controlled three-axis machine system (OZO system). The OZO system supports the ANSI/IPC-NC-349 computer numerical control format for drills and routers. See appendix B for the cutting computer program. It is necessary that original prepreg bonding sheets have a

larger slot than the larger slot layer (see Figure 2.2) because during the lamination the bonding sheet material will flow and reach its final dimension similar to the larger slot layer dimension (see Figure 2.1).

It is important to state that US Units are used in the rest of this work but keeping watts (W) as the power unit, since it is the power unit most generally used in the microelectronics industry.

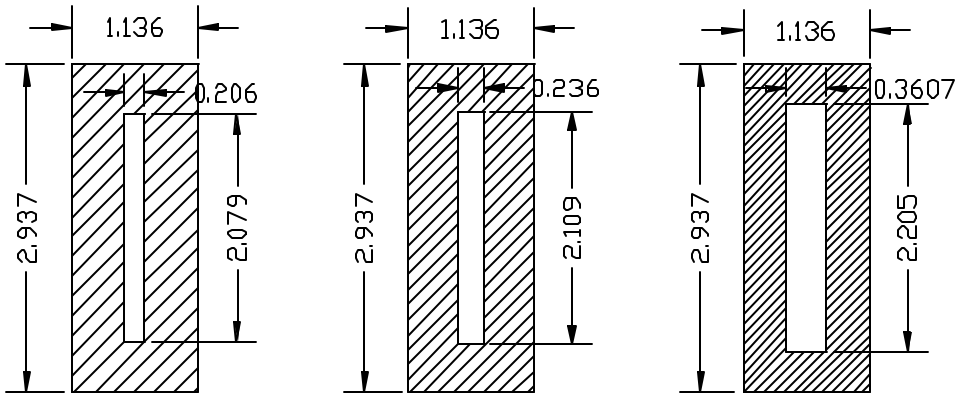

Figure 2.2 Laminate layers dimensions (inches): (a) smaller slot layer (17 mils thick), (b) larger slot layer (7 mils thick), (c) bonding sheet (3 mils thick).

2.1 Etching

Etching of the FR404 laminate layers is necessary to ensure good bonding to the prepreg sheets during lamination. The laminate layers to be etched are immersed in copper cleaner to remove any surface contaminants like dust, stains, organic particles, etc., that may have deposited during handling and routing. These surface contaminants result in

poor adhesion of the photoresist during the photolithography process and/or affect the subsequent processes like etching and lamination [9].

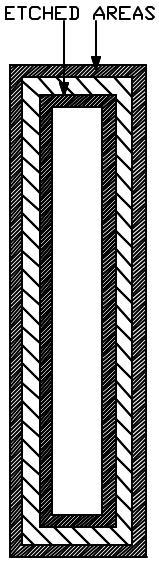

Figure 2.3 FR404 Laminate layer after etching.

The master artwork of the desired pattern is generated using computer-aided design (CAD) package. The artwork generated was transferred on to a transparency, which served as the mask.

The laminate layers are patterned using standard *photolithography process* for selective removal of materials. The Patterning is done by spinning a film of KPR-3 photoresist on the surface of FR404 laminated layers. The speeds ranged from 3000 to 4000 rpm, 40 sec. An alternate method to obtain a uniform coat of photoresist on the part is by dipping the part in the photoresist and drawing it out of at a constant rate (approximately 1in/min) [10].

The resist-coated part is soft baked for 5 min. at 250 ^{o}F in a conventional oven. The purpose of the soft bake step is to removes any solvents on the surface and dry the photoresist.

The negative artwork and a negative photoresist were used for the fabrication process. Negative acting photoresists polymerize when exposed to an ultra violet light source. The artwork is sandwiched between the piece of glass and copper clad board and exposed to an ultra-violet light source through a photo mask. For good results the exposure time lies between 4 and 5 min.

The parts are dipped in a developer to get a precise definition of the desired image. Then laminated layers are rinsed, dried and post- baked at 250 ^{o}F for 10 min.

The patterned FR404 laminated layers are etched at room temperature (70°F) using chemical etching. The patterned board is immersed in the Ferric Chloride solution (copper etchant) for 25 to 40 min. Continual agitation is essential to achieve a uniform etching rate. The board is immersed in stripper solution to remove the residual photoresist film, rinsed in cold water, and dried [10].

2.2 Lamination

The manufacturing recommended press cycle for FR404 is as follows [11]:

1. Pre-heat plate to 350 to 360 °F.
2. Load and center all layers as quickly as possible.
3. Close press to 300-350 psi.
4. When center temperature of staked layers reaches 350 °F, cure for 50 min.

5. Cool material under moderate to normal pressure slowly (5 °F/min) through 250 °F. Cooling rate can be increased when temperature lower than 250 °F.

Since the press time is depend on the stack height, number of bonding prepreg sheets, and temperature used, in practical application, the above recommended lamination parameters can be varied in order to obtain the best results for the specific application. In this work, several lamination procedures were used and tested, the result is summarized in Table 2.1.

Table 2.1 Summary of the lamination process

Lamination No.	**Temp. (°F)**	**Time (min)**	**Pressure (psi)**	**Result**
1	300	60	300	Good bonding, bad dimensional accuracy
2	210	180	300	Bad bonding, good dimensional accuracy
3	260	60	300	Bad bonding, good dimensional accuracy
4	260	180	300	Bonding is not very strong, good dimensional accuracy
5	280	180	300	Bonding is not very strong, good dimensional accuracy
6	300	120	300	Good bonding, bad dimensional accuracy
7	300	180	300	Good bonding, good dimensional accuracy

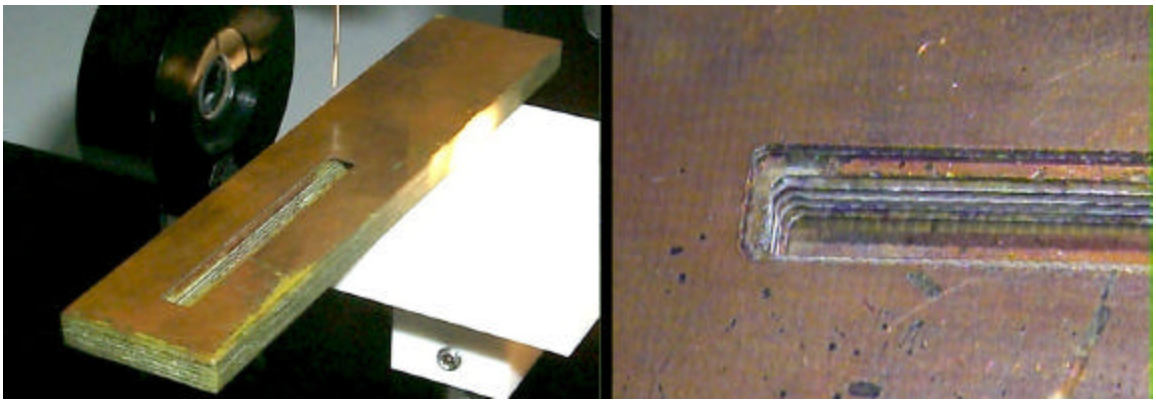

Figure 2.4 PWB with embedded heat pipe.

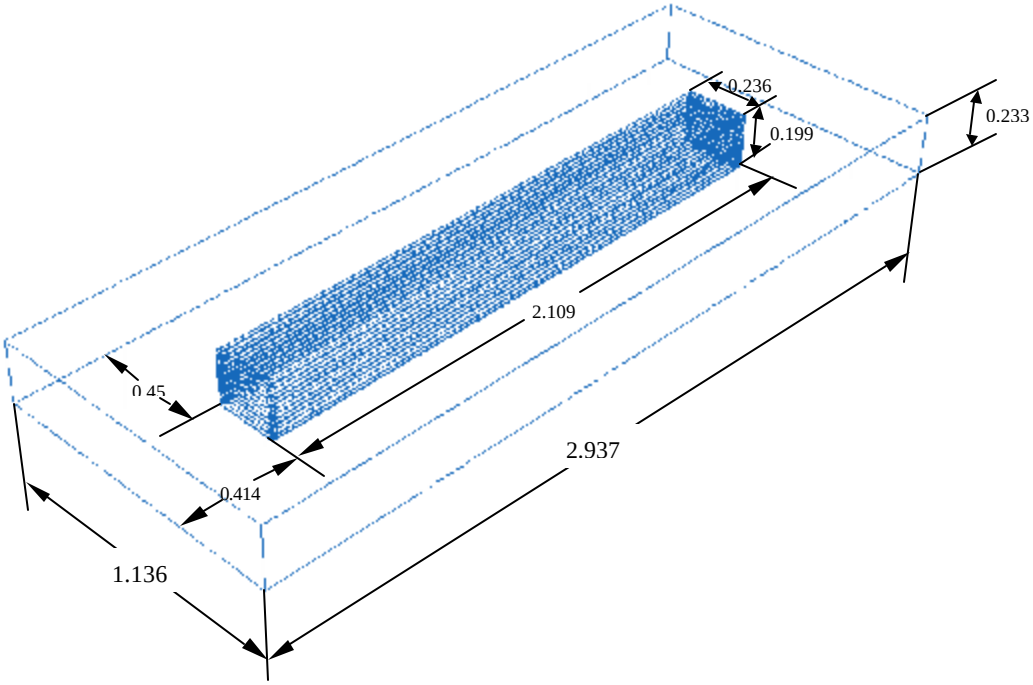

Figure 2. 5 External dimensions (inches) of the PWB.

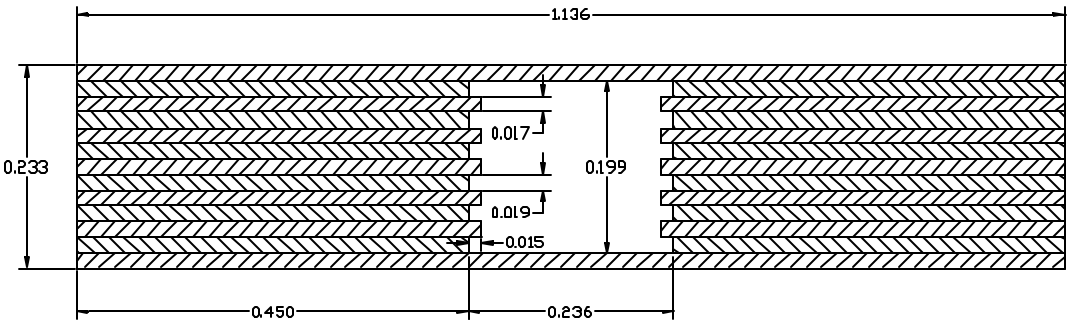

Figure 2.6 Dimensions (inches) of the PWB cross-section with embedded heat pipe.

2.3 Smear Removal

Routing smear refers to the epoxy resin that coats the inner layer copper surface in the side walled grooves formed in the laminate stack and occurs during the routing operation. This smear must be removed before plating to get a continuous and regular-coated metallization.

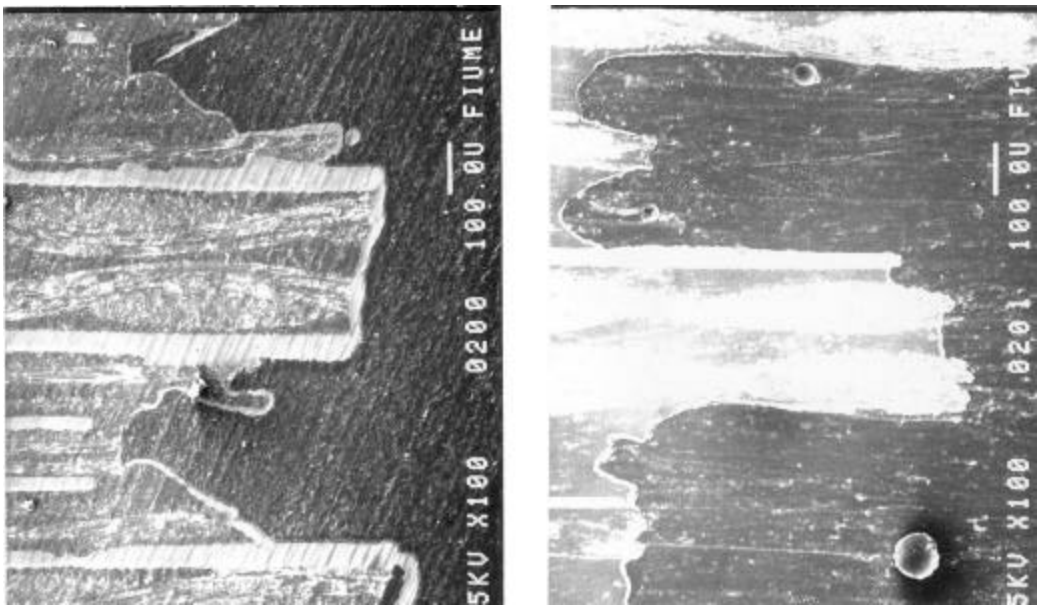

(a) (b)

Figure 2.7 Grooves: (a) without smear removal, (b) with smear removal.

The Sulfuric Acid method was used. This process is used extensively because of its ease of operation and reliability of results. A major disadvantage is a lack of control, which leads to wall pull away. Operator safety is crucial since concentrated sulfuric must be used. The method process is as follows[12]:

Sulfuric Acid, 96 %

20 s dwell, 15 s drain, room temperature

Neutralizer

8 min, 125^{o}F

Ammonium bifluoride

3 min, room temperature

High-pressure hole cleaning

2.4 Copper Plating

To make the microchannel hermetic and have enhanced wetting performance, the inner surface of the channel must be coated with a metal that improves these properties. This required development of a plating system that allows copper plating within the channel structure.

Table 2.2 summarized the step by step procedure for Conductive Copper Deposition processing [13]. Each step is named and has its respective operational time listed. As noted in the chart, a total of 61 minutes is required to go through this process.

The experimental testing of the different plating setups were conduced under the following conditions:

Operating temperature: 80 ^{o}F

Solution flow: 6 mL/min

Current density: 700 mA

Agitation: Solution movement (ultrasonic vibration bath)

Table 2.2 Conductive copper deposition process

Step No.	**Functions**	**Time Required**	**Product Name**
1	Chemical Clean Holes	5 Min.	PTH Cleaner
2	Water Spray Rinse	1 Min.	H_2O
3	Chemical Clean Copper	30 Sec.	Ammon. Persol
4	Water Spray Rinse	1 Min.	H_2O

5	Acid Tread Panel	5 Min.	H_2SO_4
6	Water Spray Rinse	1 Min.	H_2O
7	Acid Tread Panel	5 Min.	HCL
8	Activate-Seed Hole	10 Min	Activator
9	Water Spray Rinse	1 Min.	H_2O
10	Accelerate Seeded Palladium	5 Min.	Accelerator
11	Water Spray Rinse	1 Min.	H_2O
12	Overflow Rinse	1 Min.	Deionized H_2O
13	Electroless Copper Plate	10 Min.	Electroless Cu
14	Water Spray Rinse	1 Min.	H_2O
15	Acid Treat Panel	1 Min.	H_2SO
16	Electroplate Copper	10 Min	Cu Electrolyte
17	Water Spray Rinse	1 Min.	H_2O
18	Dry Panel	1 Min	Air

The experimental setup for different systems is listed as follows:

1. Figure 2.8 shows the experimental setup for electroplate copper in a closed system with the anode outside of the heat pipe

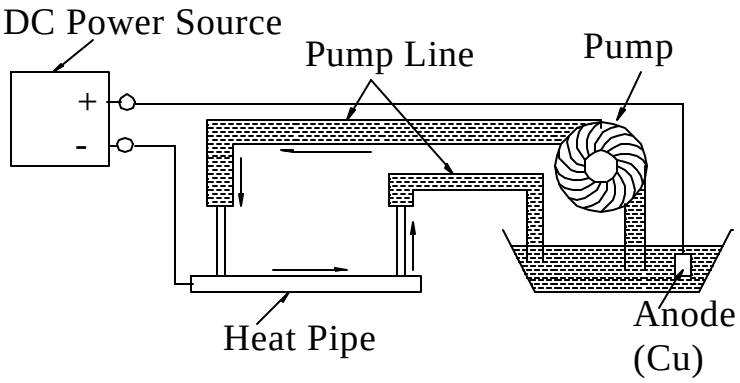

Figure 2.8 Experimental setup No. 1, electroplate copper in a closed system.

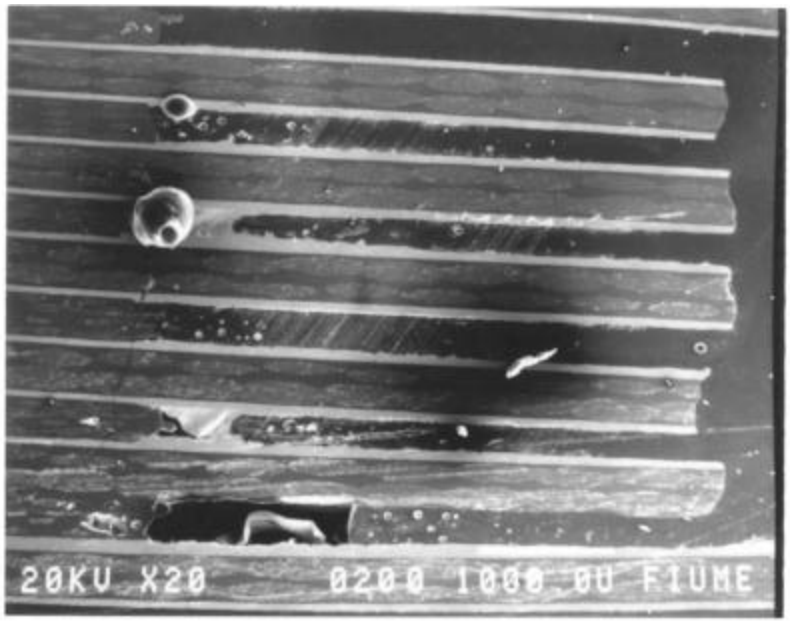

Figure 2.9 Electroplate setup No. 1, copper plated film.

2. Figure 2. 10 shows the experimental setup in a closed system with the anode inside the heat pipe. Prior to lamination, the copper anode is inserted inside the heat pipe. Wax is used as an insulator to separate the anode with the cathode.

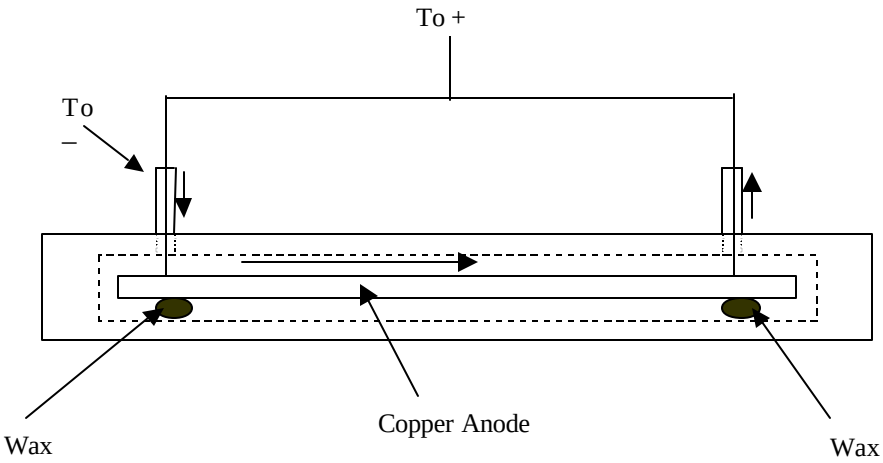

Figure 2. 10 Experimental setup No. 2, electroplate copper in a closed system.

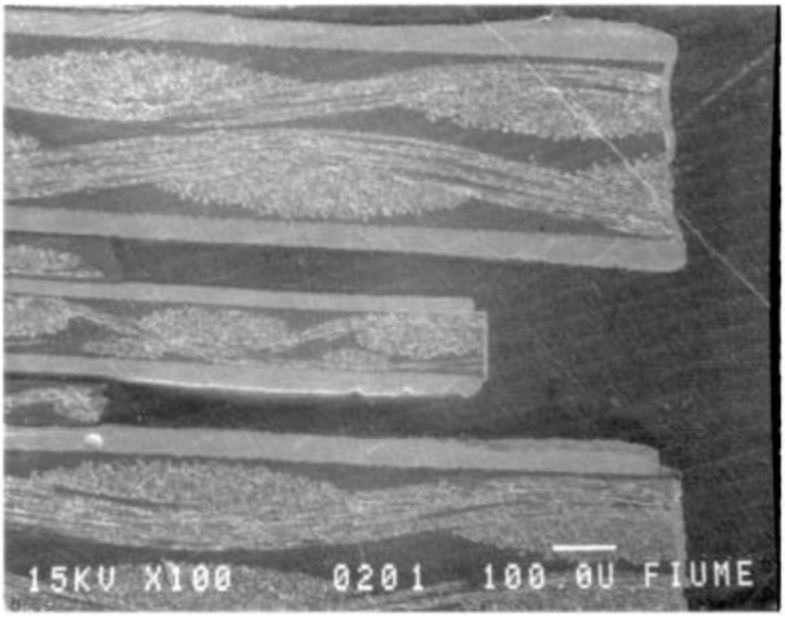

Figure 2.11 Electroplate setup No. 2, copper plated film.

3. Figure 2.12 shows the experimental setup for plating in a closed system with side holes in the heat pipe. In this method, the copper anode is inserted into the heat pipe through a hole on the side of it, and some insulating glue were used to separate the anode from the heat pipe. The electrolyte is pumped through the heat pipe from the

inlet. After plating, the side holes are sealed using epoxy materials, although metal plug could be soldered into the ends.

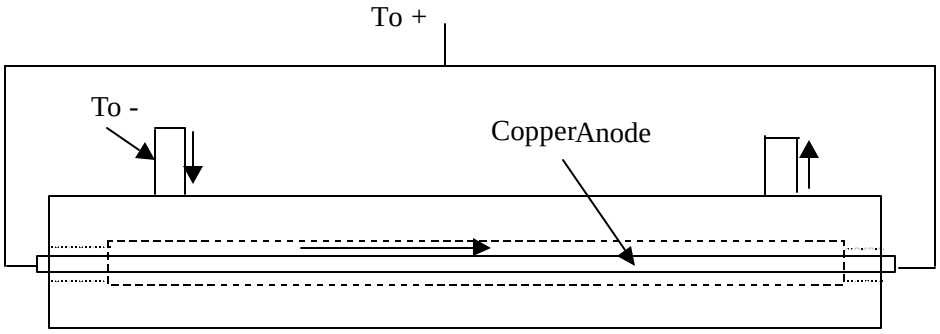

Figure 2.12 Experimental setup No. 3, electroplate copper in a closed system with side holes.

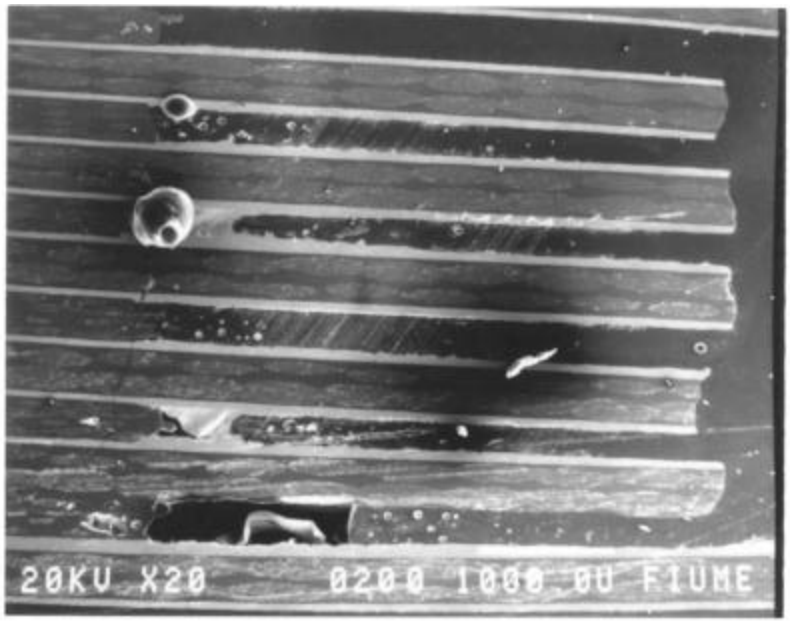

Figure 2.13 Electroplate setup No. 3, copper plated film.

4. Figure 2.14 shows the experimental setup for electroplate copper in an open system. The anode is a rectangular solid copper bar inside the heat pipe.

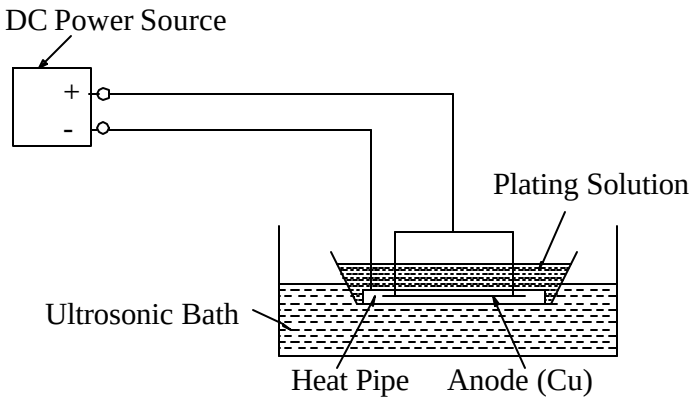

Figure 2.14 Experimental setup No. 4, electroplate copper in an open system.

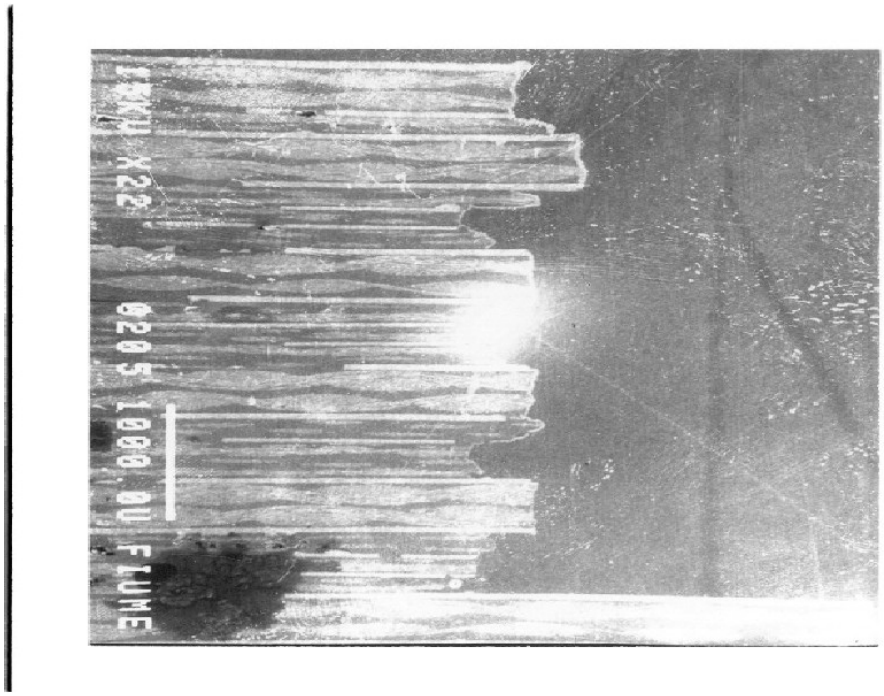

Figure 2.15 Electroplate setup No. 4, copper plated film.

5 This is an open system experimental setup (see Figure 2.16). The only difference between this setup and the previous setup is that the anode is a rectangular copper pipe with small holes on it. A pump is used to pump up the solution through the anode to inside the heat pipe.

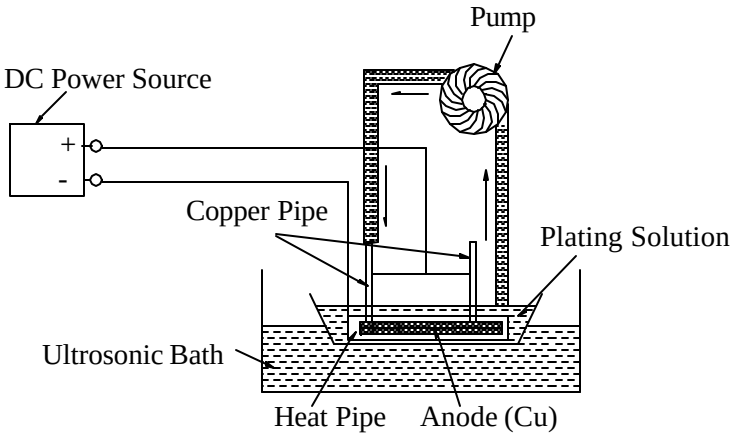

Figure 2.16 Experimental setup No. 5, electroplate copper in an open system

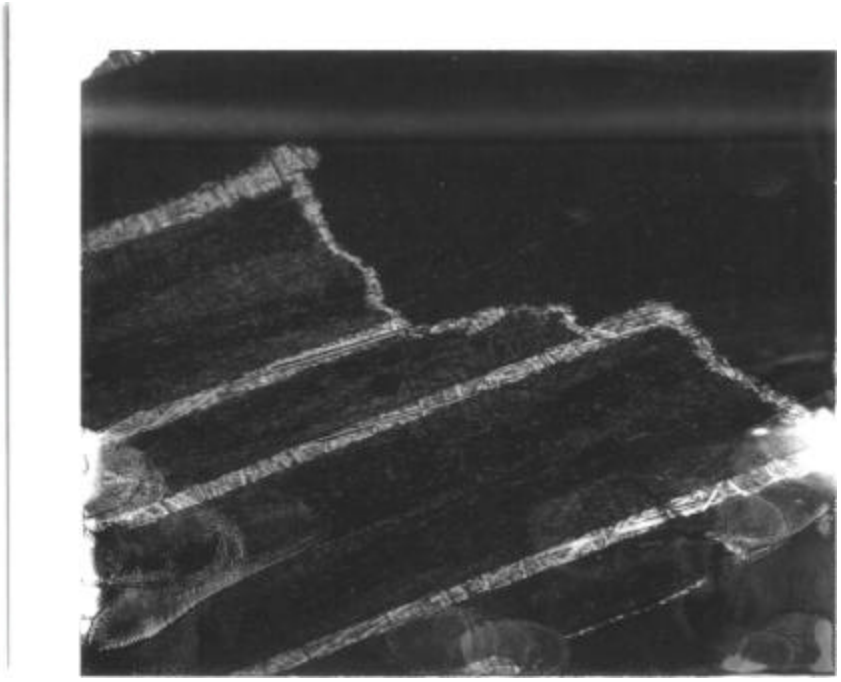

Figure 2.17 Electroplate setup No. 5, copper plated film.

Section 3

Processing and Testing

3.1 Plated Copper Film Tensile Test

The method used covers the recording of the complete stress-strain curve of copper plated film specimens under uniaxial tension at room temperature. The results of these tests provided the information on modulus of elasticity (E), yield tensile strength (s_y), fracture tensile strength (s_f), and elongation (%EL) of the copper plated film.

3.1.1 Specimen Preparation

Two different size specimens were fabricated by electroplating. The shape of the specimens was adopted from ASTM E 345-86, Standard Method of Tension Testing of Metallic Foil. Five samples were tested; specimen shape No. 1 from test 1 to test 4 and specimen shape No. 2 in test No. 5. The dimensions of the specimens are illustrated in Figure 3.1.

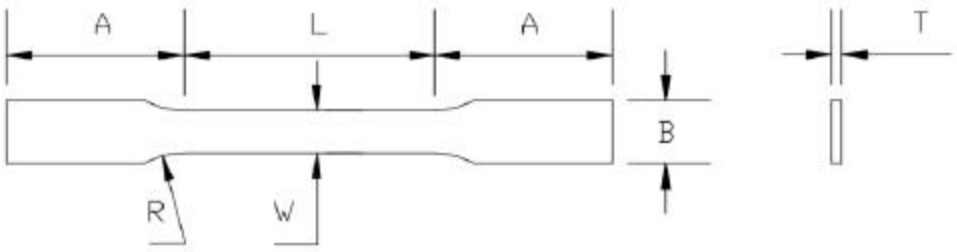

Specimen No.	A (in.)	B (in.)	L (in.)	T (in.)	W (in.)	R (in.)
1	0.750	0.025	1.0	0.0047	0.0169	0.3
2	0.750	0.060	1.0	0.0047	0.0394	0.3

Figure 3.1 Dimensions of the copper plated film specimens.

3.1.2 Testing Machine and procedure

An Instron Mini-Tester (1130) with 500-Gram Load Cell was used to evaluate the stress-strain behavior of the plated layer. The Mini-Tester has a highly sensitive electronic load weighing system with load cells employing strain gages for detecting the load applied to the specimen under test.

The specimen is fastened between two grips one attached to the load cell in the stationary crosshead and the other grip attached to the moving crosshead of the tester. The moving crosshead is operated by a vertical lead screw. A synchronous motor drives the lead screw through a gearbox that provides a variety of cross head speeds. The test results are present on a strip chart recorder. The load applied to the specimen under test is recorded by the trace of a pen on the chart. The crosshead displacement is recorded by the synchronous motion of the chart. Thus, the chart provides an accurate recording of load versus displacement.

3.1.3 Method of Determining Elongation

Chart speed: 3 in./min

Crosshead speed: 0.01 in/min

Gage length: 1 in.

$$Magnification = \frac{Chart\ \ speed}{Crossheat\ \ speed} \qquad (3.1)$$

$$Elongation(\%) = \frac{Chart\ \ displacement * 100}{Magnification\ \ ratio * Gage\ \ length} \qquad (3.2)$$

Table 3.1 Tensile test chart displacements.

	Test 1	**Test 2**	**Test 3**	**Test 4**	**Test 5**
Chart Displacement (in)	1.55	0.925	1.5	1.35	1.8
Magnification	300	300	300	300	300
Elongation (%)	0.517	0.3083	0.5	0.45	0.6

3.1.4 Mechanical Properties

Figure 3.2 shows that the initial elastic portion of the stress-strain curves are not linear. Hence, it is not possible to determine a modulus of elasticity from the slope of the linear segment. For this nonlinear behavior, either tangent or secant modulus is normally used [14].

In this analysis the secant modulus method is used. The secant modulus represents the slope of a secant drawn from the origin to a given point of stress-strain curve. The results are shown in the Table 3.1.

For those materials having a nonlinear elastic region, use of the strain offset method is not possible, and the usual practice is to define the yield strength as the stress required to produce some amount of strain [14]. In this work the yield strength is defined as the stress required to produce a strain equal to 0.003.

$$A_o = WT \qquad (3.3)$$

$$s_y = \frac{P_y}{A_o} \qquad (3.4)$$

$$s_f = \frac{P_f}{A_o} \qquad (3.5)$$

$$E = \frac{\Delta s}{\Delta e} \qquad (3.6)$$

Table 3.2 Tensile test results

	Test 1	**Test 2**	**Test 3**	**Test 4**	**Test 5**
A_o **10^{-4} (in^2)**	1.175	1.175	1.175	1.175	2.82
Elongation (%)	0.517	0.308	0.500	0.450	0.600
s_y **(psi)**	14250	12648	12358	12910	12564
s_f **(psi)**	20375	12750	15000	15250	20500
E **(psi)**	5.504 x 10^6	6.343 x 10^6	6.263 x 10^6	5.940 x 10^6	4.549 x 10^6

$$Coefficient \quad of \quad Variation = \frac{S\tan dard \quad Deviation}{Average} \qquad (3.7)$$

Table 3. 3 Results average, standard deviation, and coefficient of variation

	E **(psi)**	s_y **(psi)**	s_f **(psi)**	***Elongation (%)***
Average	5.720×10^6	12946	16775	0.475
Standard Deviation	7.330×10^5	755	3482	0.108
Coefficient of Variation	0.13	0.06	0.20	0.23

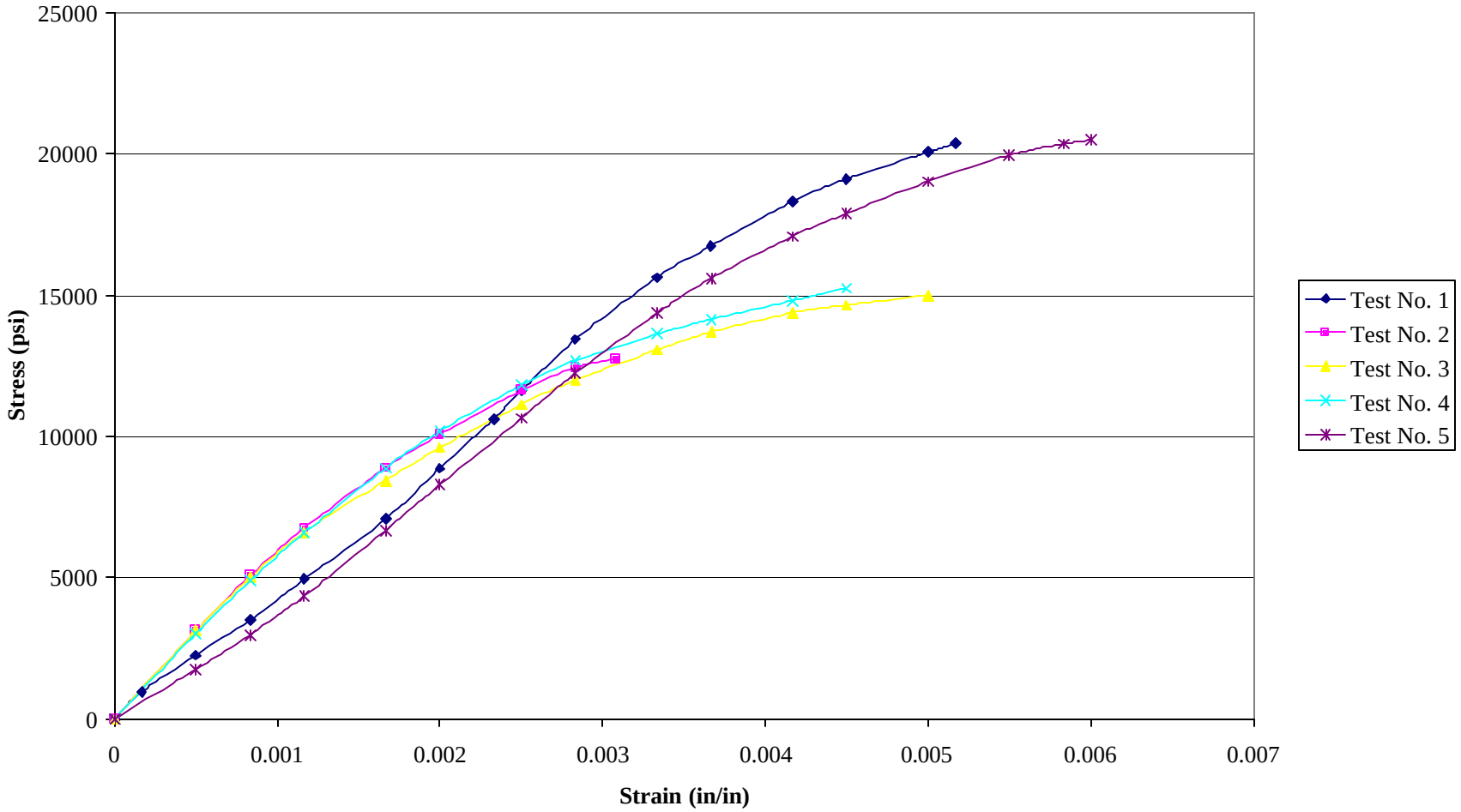

Figure 3.2 Stress-strain curves for copper plated film.

3.2 Wetting Angle

The wetting or contact angle between a fluid and solid boundary varies for a given fluid with the type of solid material, and the roughness and cleanliness of the surface. Methods typically used to determine the wetting angle are the titling plate (Spreece, 1957), the sessile drop (Bickerman, 1941), the porous plug method (Bartell, 1934), and the wetting balance method (Guastalla, 1957) [3]. The method used in this study is the sessile drop.

3.2.1 Equipment and procedure

Figure 3.3 Contact Angle Meter.

The equipment used is a Tantec Contact Angle Meter model CAM-Micro illustrated in Figure 3.3 and the procedure is the following [15]:

1. Focus the needle and deposit a 10 units drop over the surface.
2. Using the vertical adjustment knob, position the droplet's image so its base is on the horizontal cross-line.
3. Slide the measuring screen horizontally until the left edge of the droplet's image touches the vertical cross-line.
4. Determine the location of the droplet's apex.
5. Rotate the clear circular piece on the measuring screen until the hairline crosses the apex.
6. Read the contact angle on the scale.

Table 3.4 Contact angle measurement.

Surface	**Liquid**	**Surface Conditions**	**Contact Angle (Degrees)**
Plated copper	Tap water	Before copper cleaning	90
Plated copper	Tap water	After copper cleaning	74
Plated copper	DI water	Before copper cleaning	75
Plated copper	DI water	After copper cleaning	56
PWB copper layer	Tap water	Before copper cleaning	100
PWB copper layer	Tap water	After copper cleaning	78
PWB copper layer	DI water	Before copper cleaning	80
PWB copper layer	DI water	After copper cleaning	60
FR404 Epoxy	Tap water	Clean	120
FR404 Epoxy	DI water	Clean	104

3.3 Heat pipe charging

The heat pipe was charged using the filling method based on a micro-syringe and T-junction adapter developed by Y. Cao, M. Gao, and E. Pinilla [16]. Prior to charging the heat pipe, it must be verified that the heat pipe structure is hermetic.

3.3.1 Leak detection

Several methods are available which can detect leaks of different magnitudes. Very large leaks can be found by pressurizing the heat pipe with compressed gas and coating the surface with a soap solution, which bubble at the site of the leak. Smaller leaks are notice when the pipe cannot be pumped down sufficient with a vacuum-roughing pump. Still smaller leaks will cause the pressure within the high-vacuum pump to not reach its ultimate capacity. Therefore, a series of procedures is needed to determine the magnitude of the leak, and then the location of the hole in the container. The magnitude of the leak will be quantified by the pressure seen in the leaking pipe if attached to a vacuum system, instead of the standard volume of air per second (std cm^3/s). This is done since most experiments have access to vacuum equipment, but do not have a leak rate measurement system. With this method, the pressure inside containers with gross leaks ranges from atmospheric to 1 torr, low vacuum leaks range from 1 torr to 10^{-3} torr, and high-vacuum leaks from 10^{-3} to 10^{-9} torr. High vacuum leaks can be detected with a spectrometer leak detector.

3.3.2 Filling the Heat Pipe with Working Fluid

After passing the leakage testing the laminated heat pipe was charged by using syringe method. In this method, a unique micro-syringe, designed primarily for precision measurement and displacement of liquid or gaseous samples into chromatographic analyzers was used. The syringe consists of a turn valve with a Teflon seal, a leak-tight Teflon plunger tip, and a removable needle. This type of syringe is recommended for use in either a high vacuum or with pressures up to 250 psi, with gases or liquids. The turn valve can be used to isolate the working fluid stored in the barrel from the vacuum during evacuating of the heat pipe. The plunger makes flush contact with the bottom of the syringe barrel when fully depressed, virtually eliminating any dead volume.

The filling setup is schematically shown in Figure 3. 4.

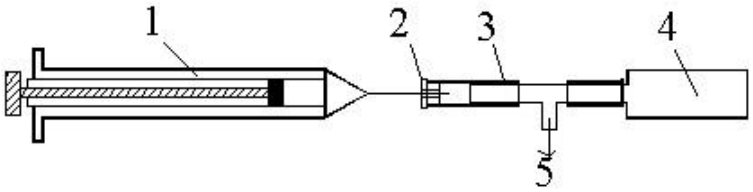

1-Microsyringe
2-Teflon seal
3-Polyurethane tubing
4-Heat pipe
5-To vacuum system

Figure 3. 4 Micro-syringe filling setups

The heat pipe is connected to the syringe using the polyurethane/Teflon adapter through which the needle is inserted, it is completed through a T-junction. The filling procedure

for the system incorporating the micro-syringe and the T-junction can be outlined as follows:

(1) Fill the syringe with the working liquid.

(2) Lock in the liquid. Replace the needle with a dry one and lock in the working liquid in the barrel by screwing the nosepiece with at least two turns left to tighten. At this time, there is no liquid in the needle, and the liquid is isolated from the ambient.

(3) Evacuate the heat pipe. Connect the syringe with the heat pipe through the T-junction and connect the T-junction to the vacuum system, until the desired vacuum is reached. The vacuum inside the heat pipe is difficult to measure and is certainly lower than the system vacuum because of the small diameter of the filling pipe. Adequate time should be allowed for the heat pipe to reach the desired vacuum. Usually, 3×10^{-5} torr of vacuum can be obtained.

(4) Fill the heat pipe. Screw the needle nosepiece all the way and depress the plunger down to the dead point to displace the working liquid into the heat pipe via the filling tube.). The laminated heat pipe was charged of 0.1 ml of distilled water.

(5) Finally, pinch and seal the heat pipe filling tube.

3.4 Heat Pipe Performance

Steady state testing and evaluation procedures for heat pipes and thermosyphons are typically designed to measure the maximum heat transport capacity, the end-to-end temperature drop, the thermal resistance, and / or the effect of variations in the local

gravitational acceleration on the overall thermal performance. For low or moderate temperature heat pipes of the type typically encountered in the thermal control of electronics, all of these measurements can be accomplished using a single, relatively simple test facility and straightforward test procedures. Figure 3.5 illustrates a steady state test facility of the type that would normally be used for low or moderate temperature heat pipes. As shown, the test facility consists of four principal subsystems: the test pipe, a heat source, a heat sink, and a temperature measurement system.

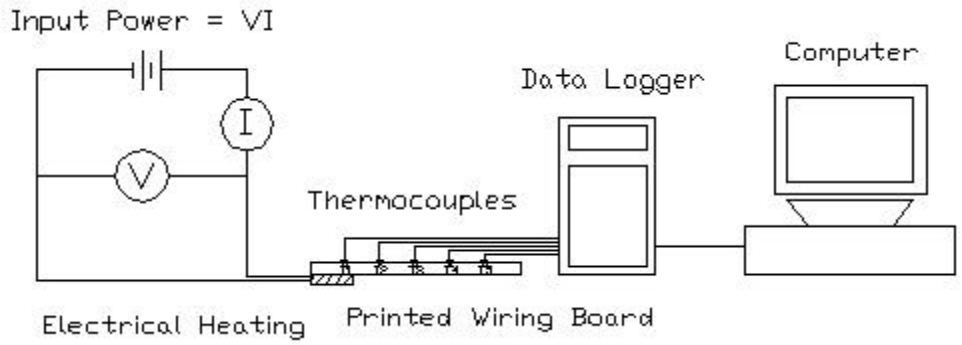

Figure 3.5 Heat pipe thermal testing setting

3.4.1 Test Facility

Because of the simplicity and accuracy with which the thermal power applied to the test pipe can be measured, electrical resistance heating is the most common type of heating system used. Other methods, including induction heating, heated constant temperature baths, and radiation, have also been used successfully [1]. Regardless of the method, what is needed is a means by which the temperature and power input into a specific region of the heat pipe can be carefully monitored and controlled. For the case of electrical resistance heating, the electrical energy input to the heat pipe or joule heating can be measured either by measuring the input voltage and current or by measuring the

voltage and using the known electrical resistance of the heating element. The electrical power input to the system can be controlled by means of a simple variable power transformer.

In addition to a means for adding power to the evaporator section of the heat pipe, a system is also required by which the heat can be rejected. Again, there are several alternatives available, including radiation, latent heat rejection to a spray cooling system, rejection to a liquid-cooled heat exchanger, and free convection to the surrounding atmosphere [1]. The latter of these was used in this study because represents the most practical alternative.

To determine the transport characteristics, it is also necessary to evaluate the axial temperature distributions along the length of the heat pipe. These measurements were made on five different points along the longitudinal axis on the external case of embedded heat pipe (see Figure 3.6). Thermocouples in conjunction with a computerized data acquisition system were used to monitor the power input, heat rejected, and temperature distribution throughout the tests. While the temperature gradient along the length of the heat pipe may be quiet small, is important to note that in most heat pipe test procedures, the absolute temperature measurements are not as critical as the relative temperatures differences. For this reason, the use of thermocouples with a relatively large uncertainly (±0.5 °F) when compared with the temperature gradients being measured, can yield results that are quite acceptable. However, care should be taken to ensure that at any given temperature all of the thermocouples would yield the same value. This was accomplished by verifying the thermocouples and data acquisition system at the

freezing point and atmospheric boiling point of water to ensure that, for a given condition, they yield similar results prior the installation on or in the test pipe. Previous tests have shown that temperature differences can be measured to within an accuracy of ±0.05 °F using this technique [1].

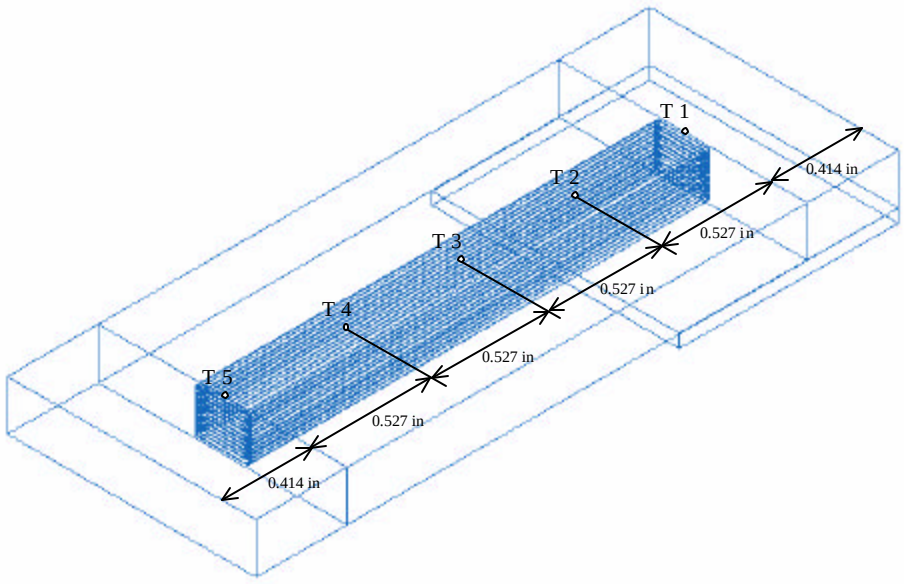

Figure 3.6 Temperature points distributions along the length of the heat pipe.

3.4.2 Test Procedure

Test procedures consisted in incrementing the input power to the evaporator in predetermined increments and determined the maximum power input that the embedded heat pipe in the PWB could accept without failing. The increments in power input were: 2.5 W, 5.6 W, and 10 W. The same tests were conducted to the PWB with uncharged heat pipe. Figure 3.7 to Figure 3.9 compare the temperature distribution along heat pipe length for charged and uncharged heat pipes for 2.5 W, 5.6 W, and 10 W respectively.

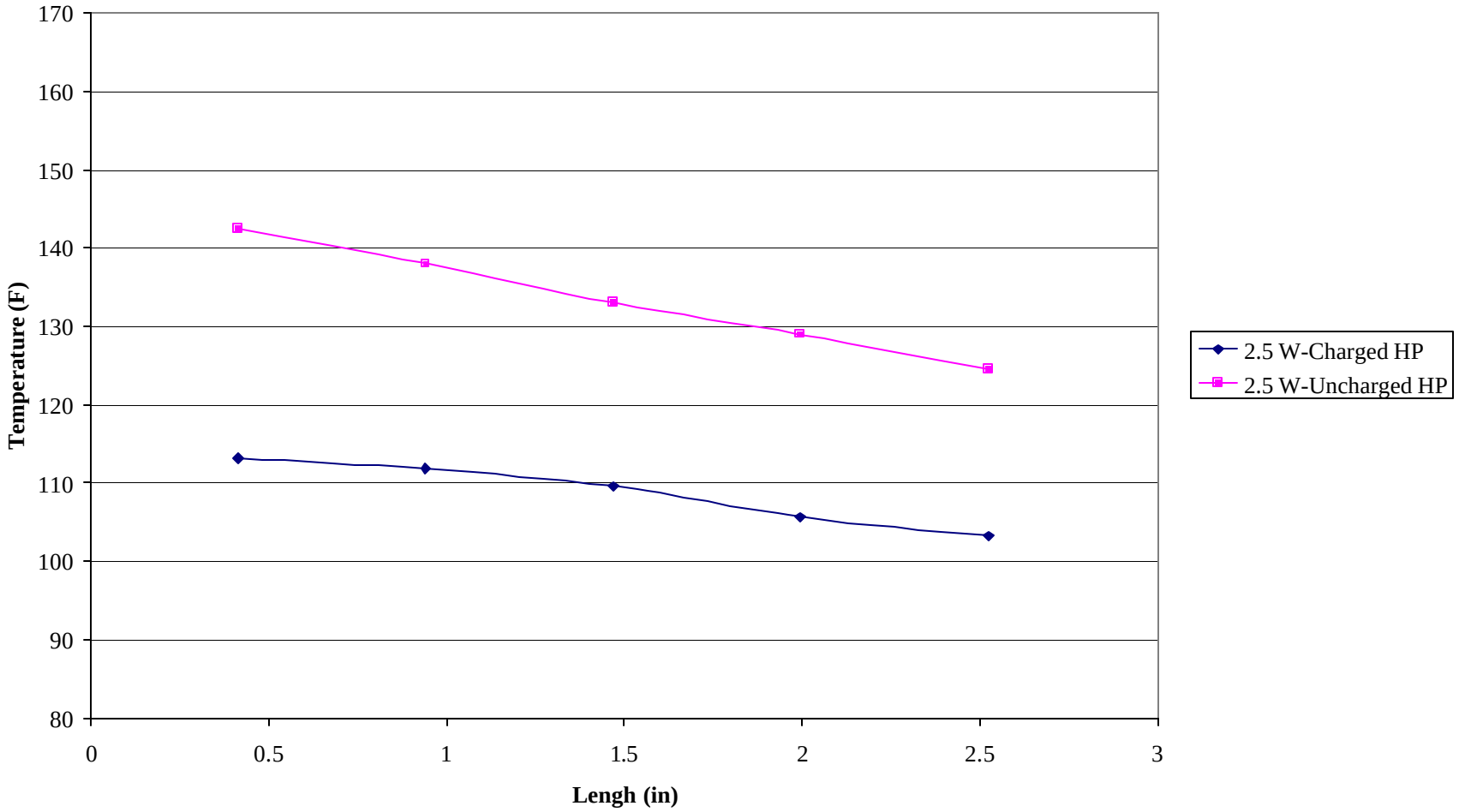

Figure 3.7 Experimental temperature distribution along heat pipe length with 2.5 W of input power.

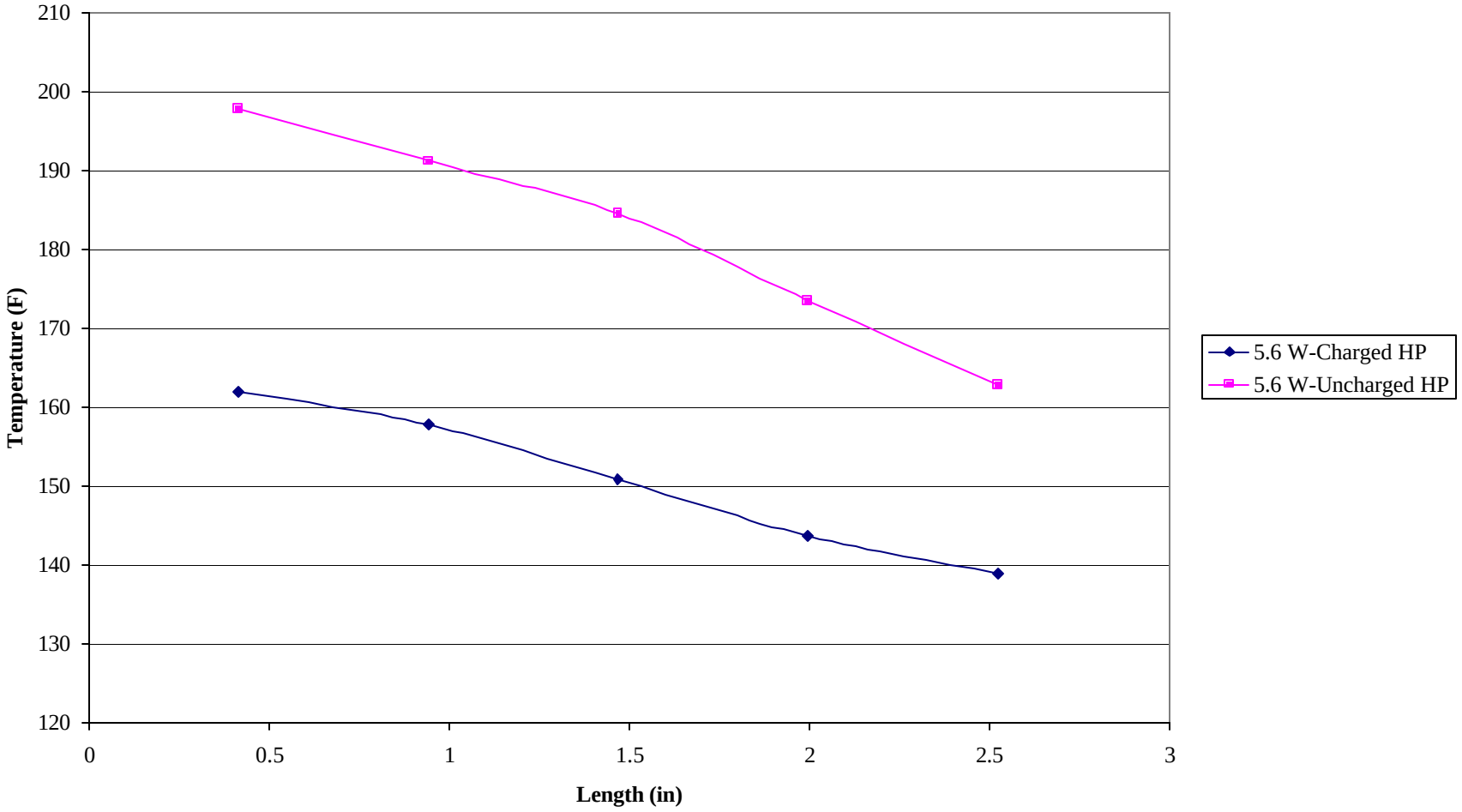

Figure 3.8 Experimental temperature distribution along heat pipe length with 5.6 W of input power.

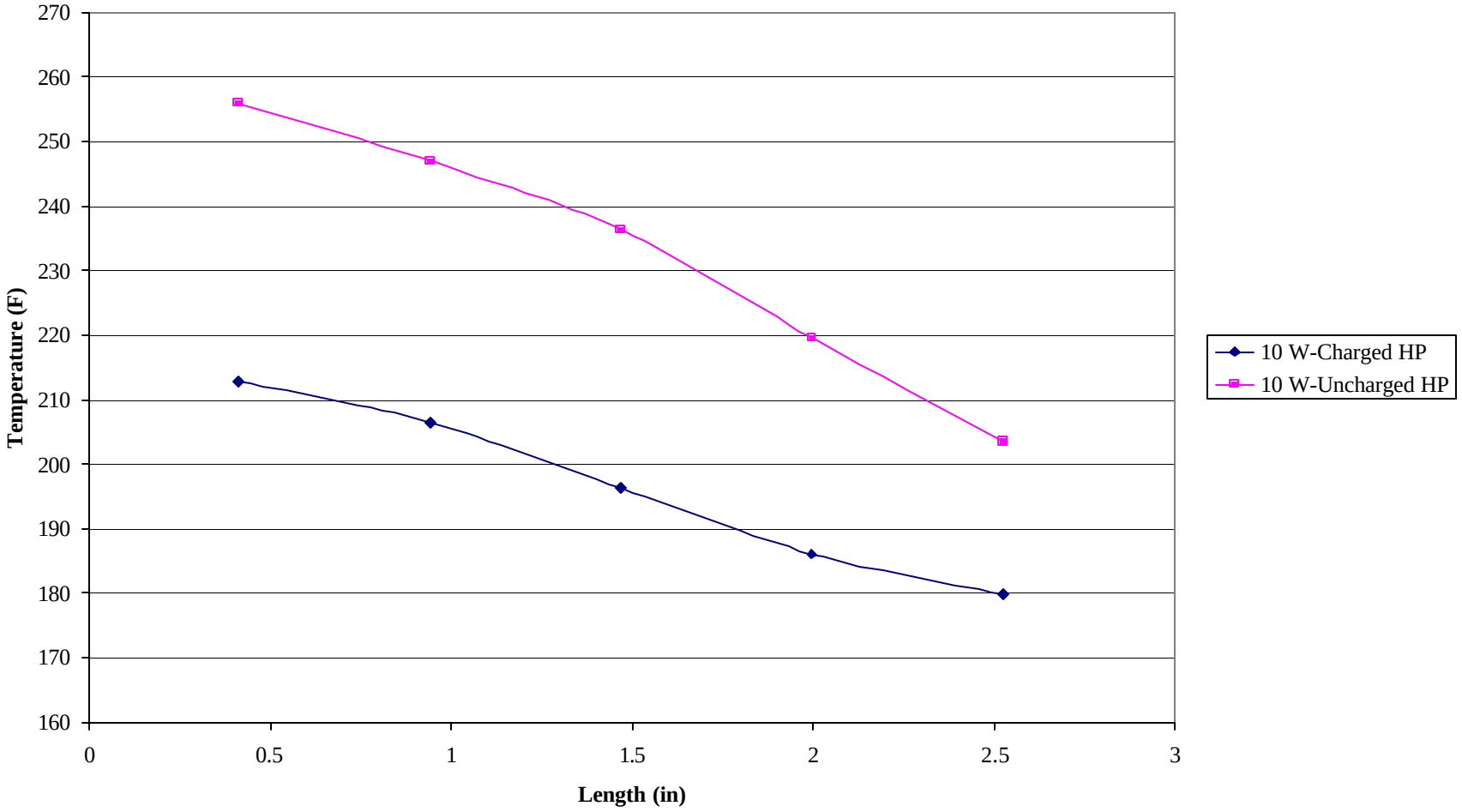

Figure 3.9 Experimental temperature distribution along heat pipe length with 10 W of input power.

Section 4

Finite Element Modeling

In parallel with the test, a finite element analysis was also made in the present study to determine the stresses induced in the substrate by thermal gradients. The intent was to reproduce the thermal gradients found in the experimental thermal performance fitting the heat pipe conductivity in the finite element model.

The physical structure of the embedded heat pipe was modeled for both heat pipe operation and system level exposure to environmental stresses, such as temperature, using a FEA software (ABAQUS/CAE 6.1 from HKS, Inc). The material properties of the laminated material, and the plated metallization were determined and used to model the mechanical performance (i.e. thermally induced stresses and strains) over the environmental stress exposure. For this purpose the following two FEA analyses were conducted:

1. A 3D heat transfer analysis to determine the temperature distribution through the whole PWB model.
2. A 2D sequentially coupled thermal-stress analysis of the cross section at a selected point of the embedded heat pipe.

Because ABAQUS has no built-in system a consistent system of units has to be selected for all input data before starting to define the models [17]. The system selected was the US Unit (inch) system.

Length: in

Force: lbf

Mass: lbf- s^2/in

Time: s

Stress: lbf/in^2

Energy: in-lbf

Power: in-lbf/s

Density: lbf s^2/in^4

4.1 3D Heat Transfer Analysis of the PWB Model

An uncoupled 3D heat transfer analysis is used to model the PWB solid body with general, constant thermal conductivity irrespective of temperatures, internal energy generated in the heater, and quite general convection and radiation boundary conditions.

Two different analyses were performed in this model. The first one simulating a charged heat pipe and the second one simulating an uncharged heat pipe. The only difference between these two analyses is the thermal conductivity of the vapor space part as shown in Table 4.1

4.1.1 Assumptions

The numerical analysis was conduced under the following assumptions:

(1) Heat transfer coefficient from test printed circuit board to air has a constant value irrespective of location and/or shape.

(2) The ambient air temperature is constant.

(3) A printed circuit board model has a shape and dimensions shown in Figure 2. 5 and Figure 2.6.

(4) Every member has a constant thermal conductivity irrespective of temperatures.

(5) Contact resistance is constant between the heating element and the printed circuit board.

(6) The axial temperature testing points along the length of the heat pipe were located at the same positions as the experimental testing points (see Figure 3.6).

4.1.2 Model Definition

The defining parameters of the model include shape and geometry information as well as material property data. All of these components are modeled using eight-node convection diffusion brick linear element. The typical material properties were used, except for the conductivity of PWB material. Since the typical conductivity of the FR404 epoxy is not the same as the PWB part after lamination due the copper layer in the top and bottom surfaces of each laminate layer. The conductivity of the PWB material was fit to meet the experimental temperature distribution.

Table 4.1 lists the material properties of the different parts of the heat pipe assembly including the two different sets of materials properties for the Vapor Space part, one for the charged heat pipe analysis and other one for the uncharged heat pipe analysis. These parts can be seen in Figure 4.1.

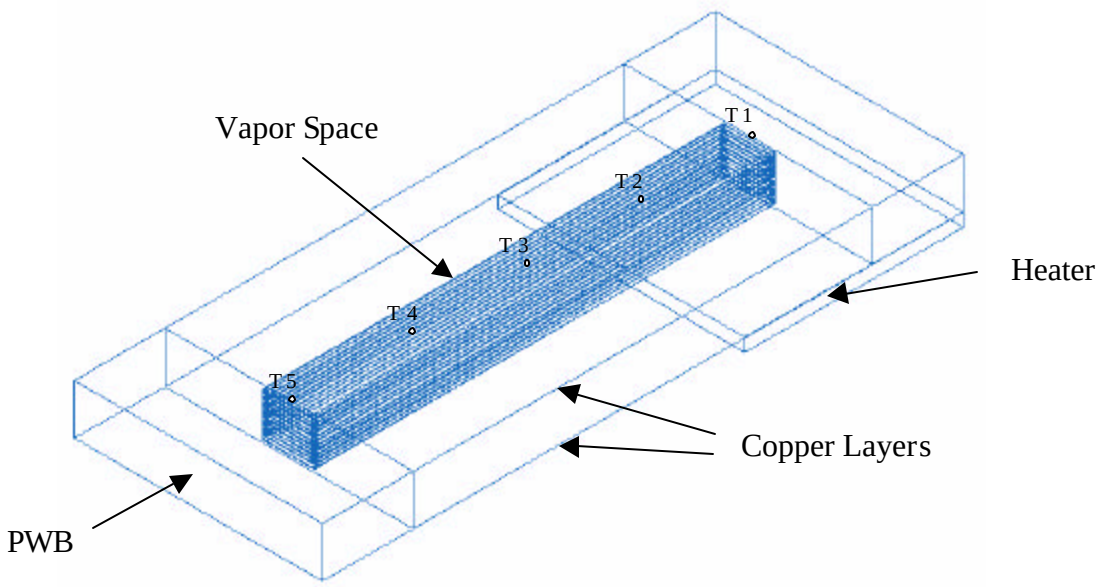

Figure 4.1 Printing Wiring Board model.

Table 4.1 3D Thermal Model material properties.

	Conductivity [W/m°K]			Density [g/cm^3]	Specific Heat [J/kg°K]
Copper Layer	398			8.96	385
PWB	X 7.61	Y 0.48	Z 7.61	1.90	1150
Vapor Space (Charged Heat Pipe Analysis)	X 80	Y 400	Z 80	8.96	385
Vapor Space (Uncharged Heat Pipe Analysis)	X 0	Y 0	Z 0	8.96	385
Heater	398			8.96	385

4.1.3 Element Selection

The element selected for the all mesh model components is the linear hexahedron element, 8-node convection diffusion brick, ABAQUS type DCC3D8. This element holds temperature as active degree of freedom [17].

4.1.3.1 Surface Contact Interaction

The Surface Contact Interaction in this model defines the thermal interactions between regions of the model and between a region of the model and its surroundings.

The *Tie Surface Interaction* was used to fuse together all part-instance faces in contact even though the meshes created on the surfaces may be dissimilar. Creating a tie surface interaction is analogous to including the *CONTACT PAIR, TIED option in a solver input file.

The *Thermal Film Condition* was used to define the cooling due to convection of all surfaces of the model expose to the surrounding. A film condition interaction is analogous to including the *SFILM option in a solver input file.

Radiation to Ambient Interaction used in this model describes heat transfer between the nonconcave surface of the model and a nonreflecting environment due to radiation. A radiation interaction is analogous to including the *SRADIATE option in a solver input file.

4.1.4 Mesh Discretization

ABAQUS /CAE can use a variety of meshing techniques to mesh models of different topologies: structured meshing, swept meshing, free meshing. The different meshing

techniques provide varying levels of automation and user control. Figure 4.2 displays the meshed model.

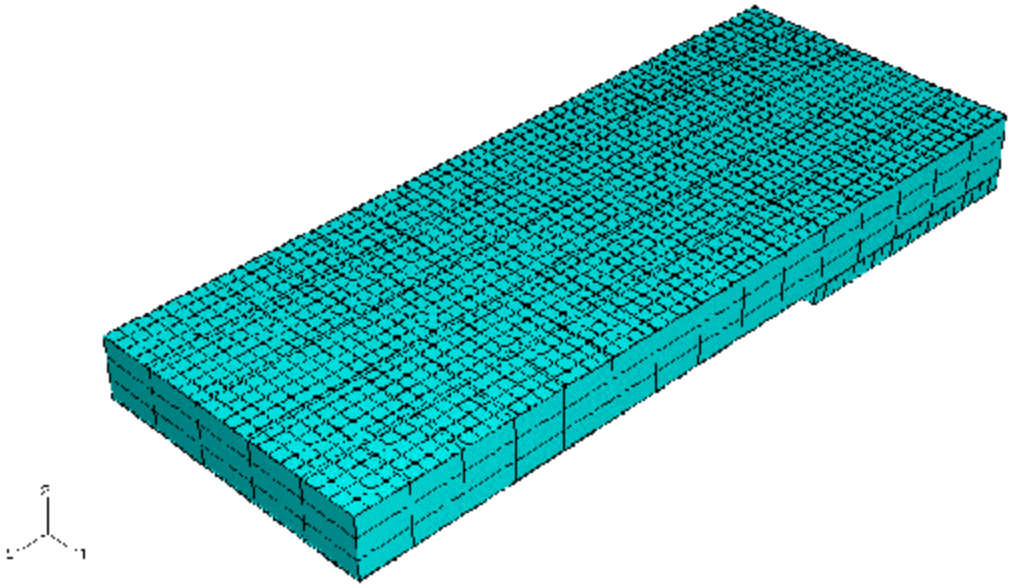

Figure 4.2 Meshed Model.

Structure meshing was used since it gives most control over the mesh because it applies pre-established mesh patterns to particular model topologies. The PWB-1 part-instance was too complex to be meshed using pre-established mesh patterns directly. Consequently, it had to be partitioned into simple regions with topologies for which structured meshing patterns exits. The total number of elements is 3435 and nodes 7276. Table 4.2 shows the mesh break down by part-instances.

Table 4.2 Part-instance mesh break down.

PART-INSTANCE	ELEMENT TYPE	NODES	ELEMENTS
Copper Layer-1	Linear Hexahedron DCC3D8	2806	1320
Copper Layer-2	Linear Hexahedron DCC3D8	2880	1357
PWB-1	Linear Hexahedron DCC3D8	384	214
Vapor Space-1	Linear Hexahedron DCC3D8	198	84
Heater-1	Linear Hexahedron DCC3D8	1008	460
	TOTAL	7276	3435

4.1.5 Loading Conditions

The loading condition attempt to simulate the heat generated in the heater. Three heat inputs levels will be analyzed: 2.5 W (22.121 in lbf/s), 5.6 W (49.551 in lbf/s), and 10 W (88.485 in lbf/s).

The *DFLUX option was used to specify the body fluxes (flux per unit volume) in the heater. Since the heater volume is 0.06816 in^3 the corresponding flux per unit volume for the three different heat inputs are: 36.678 W/in^3 (324.547 in lbf/s in^3), 82.160 W/in^3 (726.985 in lbf/s in^3), and 146.714 W/in^3 (1298.188 in lbf/s in^3).

4.1.6 Type of Analysis

Uncoupled heat transfer analysis is a pure heat transfer analysis using heat transfer elements and the *HEAT TRANFER procedure. This is linear, transient, heat transfer analysis used to model solid body heat conduction with general, constant thermal

conductivity irrespective of temperatures, internal energy generated in the heater, and quite general convection and radiation boundary conditions.

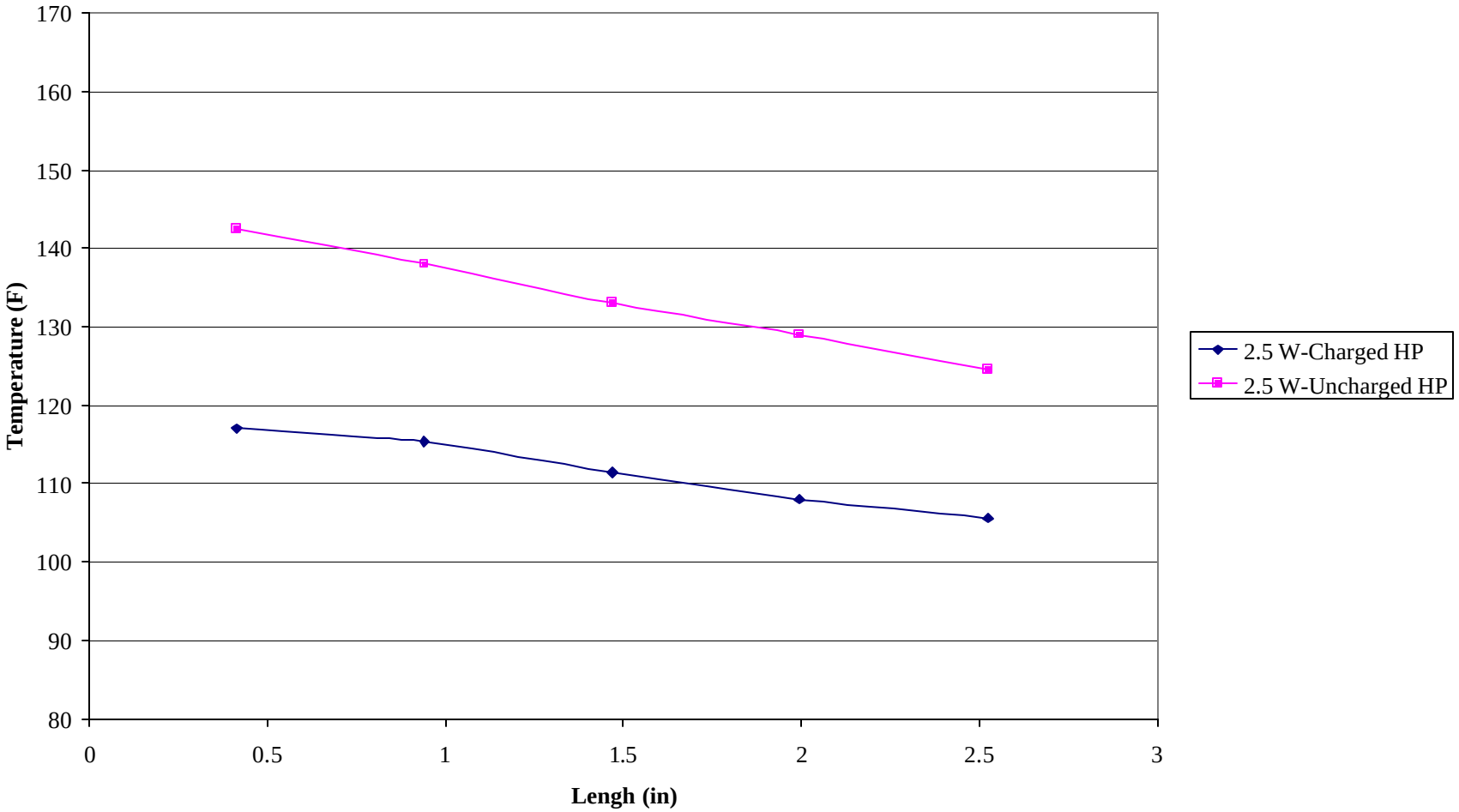

Figure 4.3 FEM temperature distribution along heat pipe length with 2.5 W of input power.

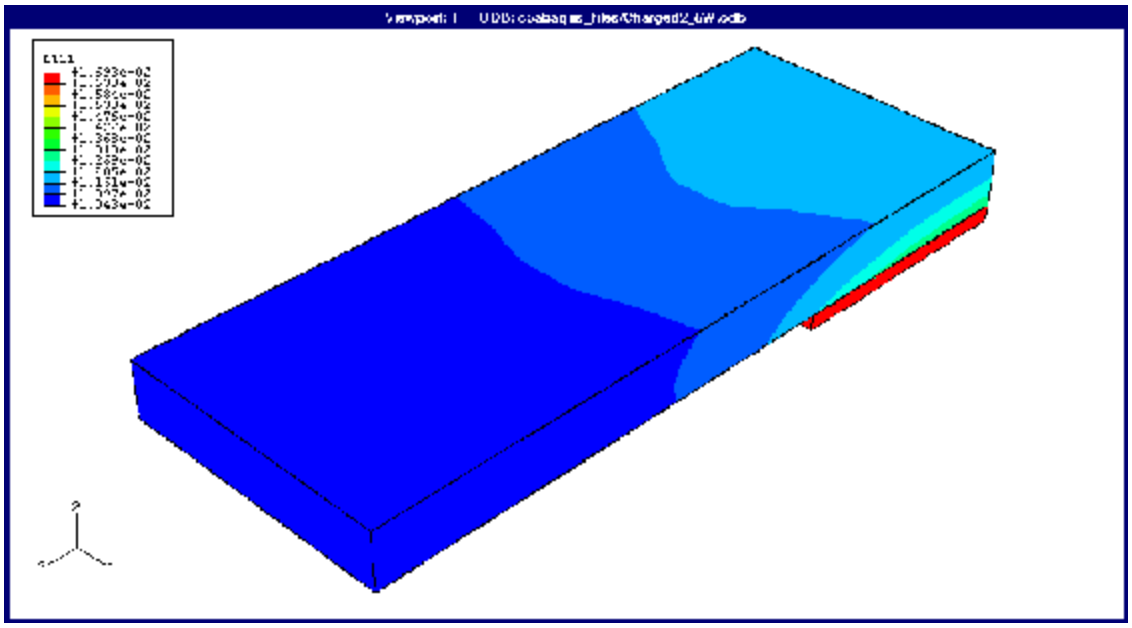

(a)

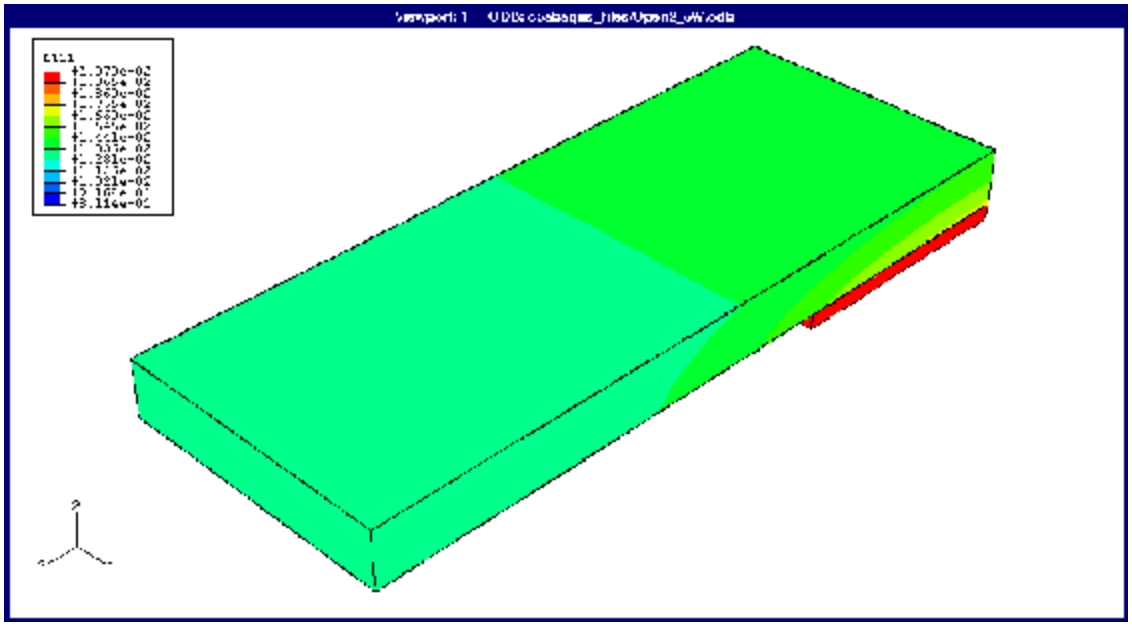

(b)

Figure 4.4 Temperature distribution top view for 2.5 W of input power: (a) charged heat pipe, (b) uncharged heat pipe.

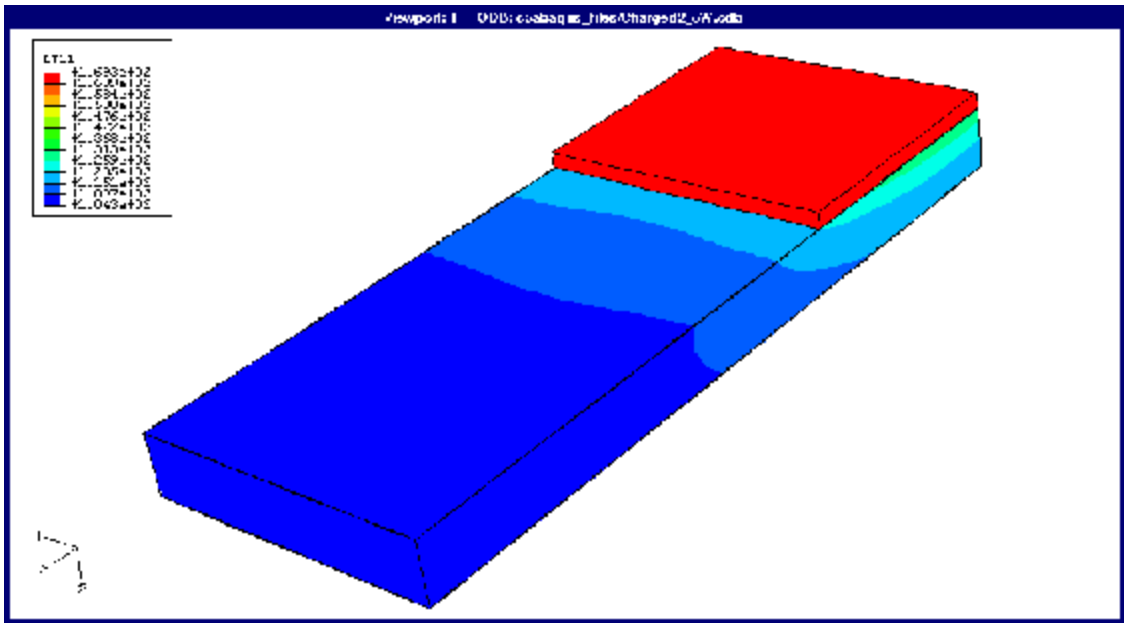

(a)

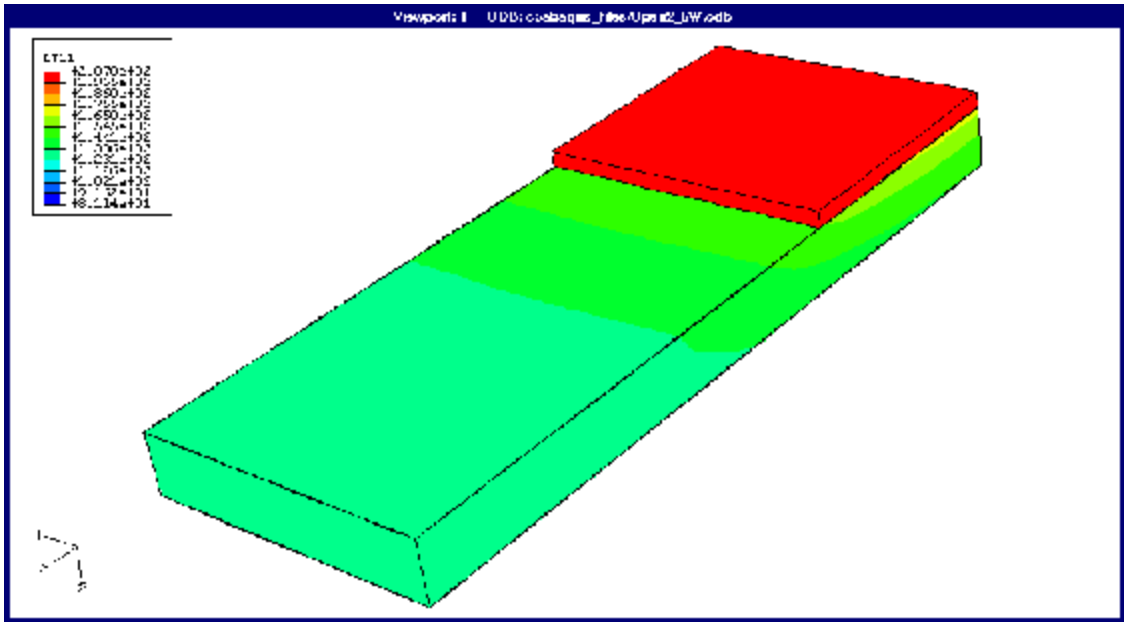

(b)

Figure 4.5 Temperature distribution bottom view for 2.5 W of input power: (a) charged heat pipe, (b) uncharged heat pipe.

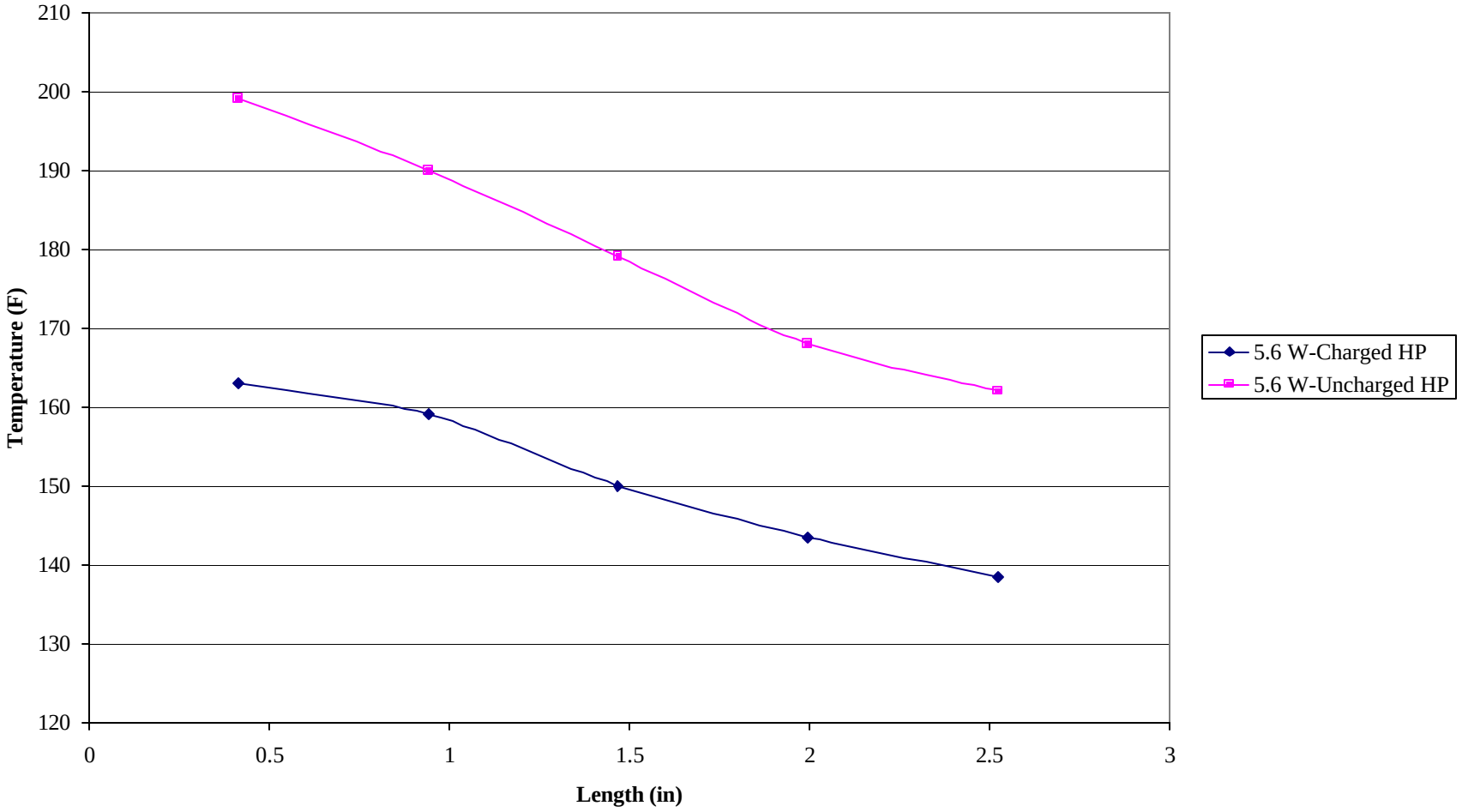

Figure 4.6 FEM temperature distribution along heat pipe length with 5.6 W of input power.

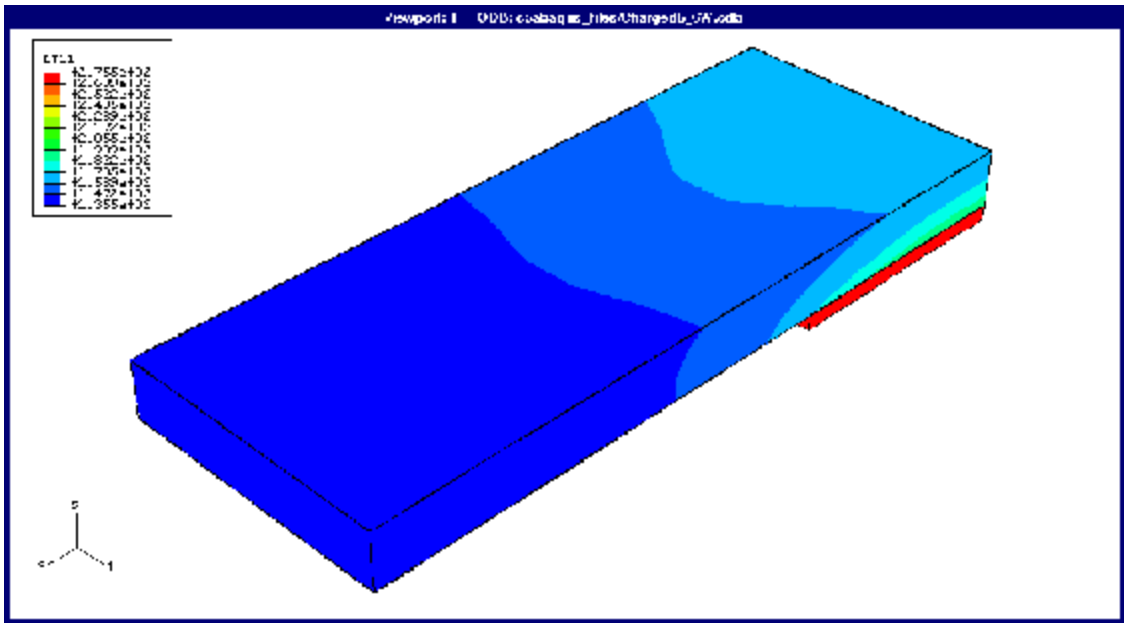

(a)

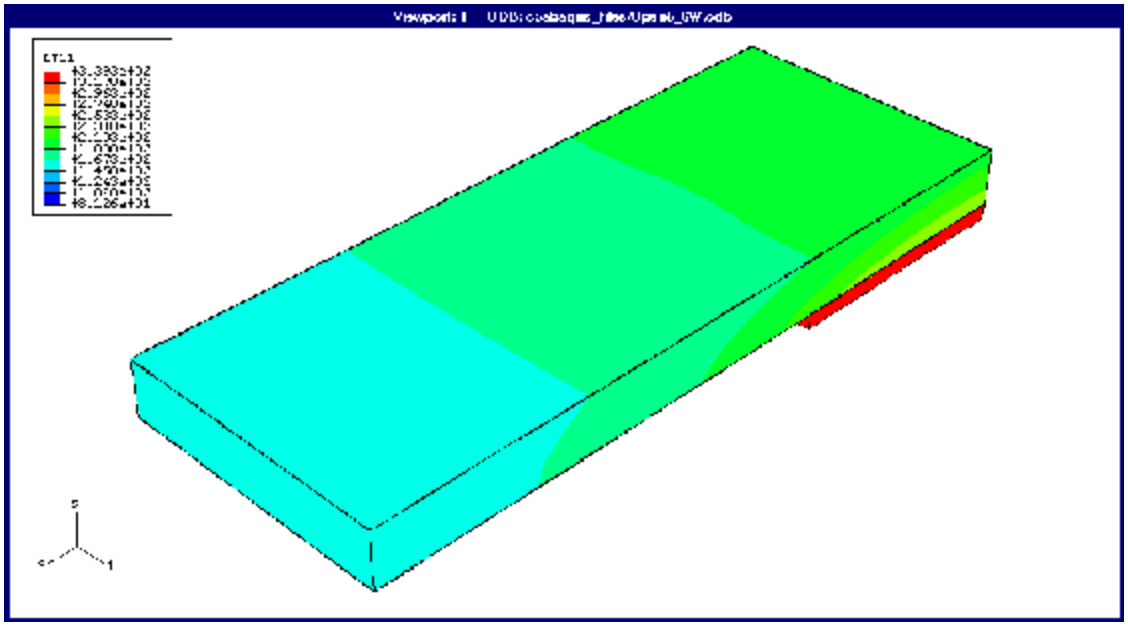

(b)

Figure 4.7 Temperature distribution top view for 5.6 W of input power: (a) charged heat pipe, (b) uncharged heat pipe.

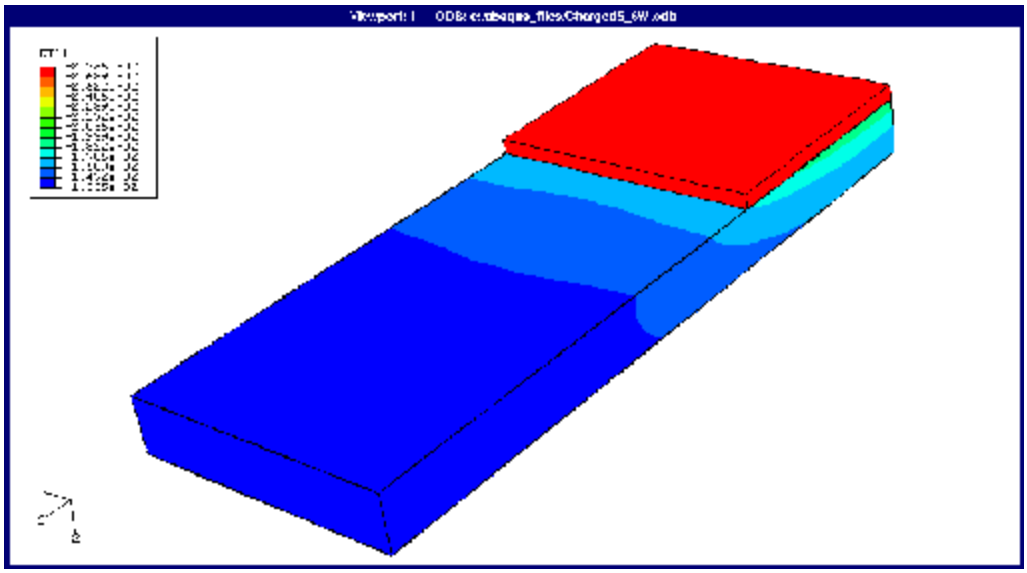

(a)

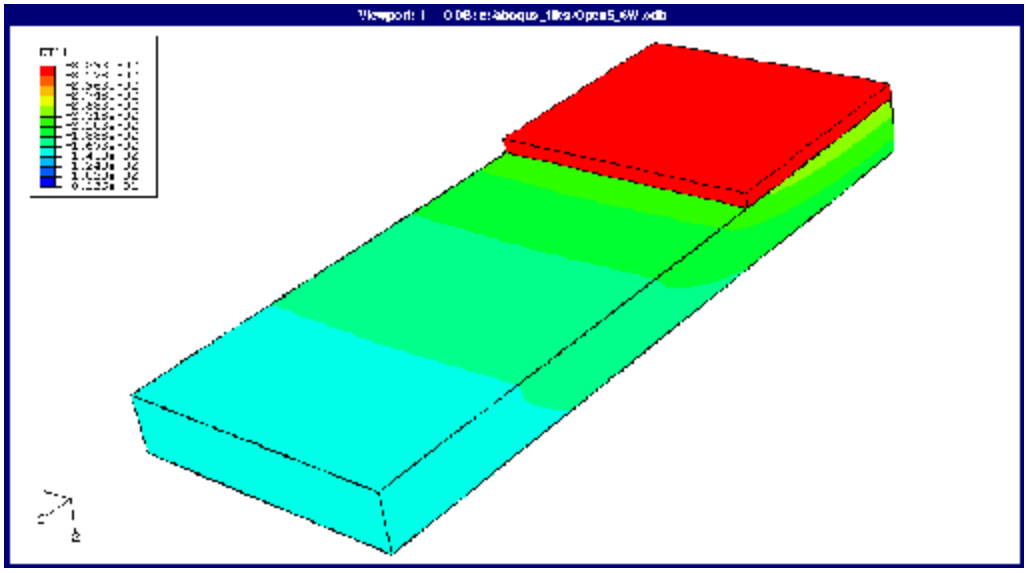

(b)

Figure 4.8 Temperature distribution bottom view for 5.6 W of input power: (a) charged heat pipe, (b) uncharged heat pipe.

.

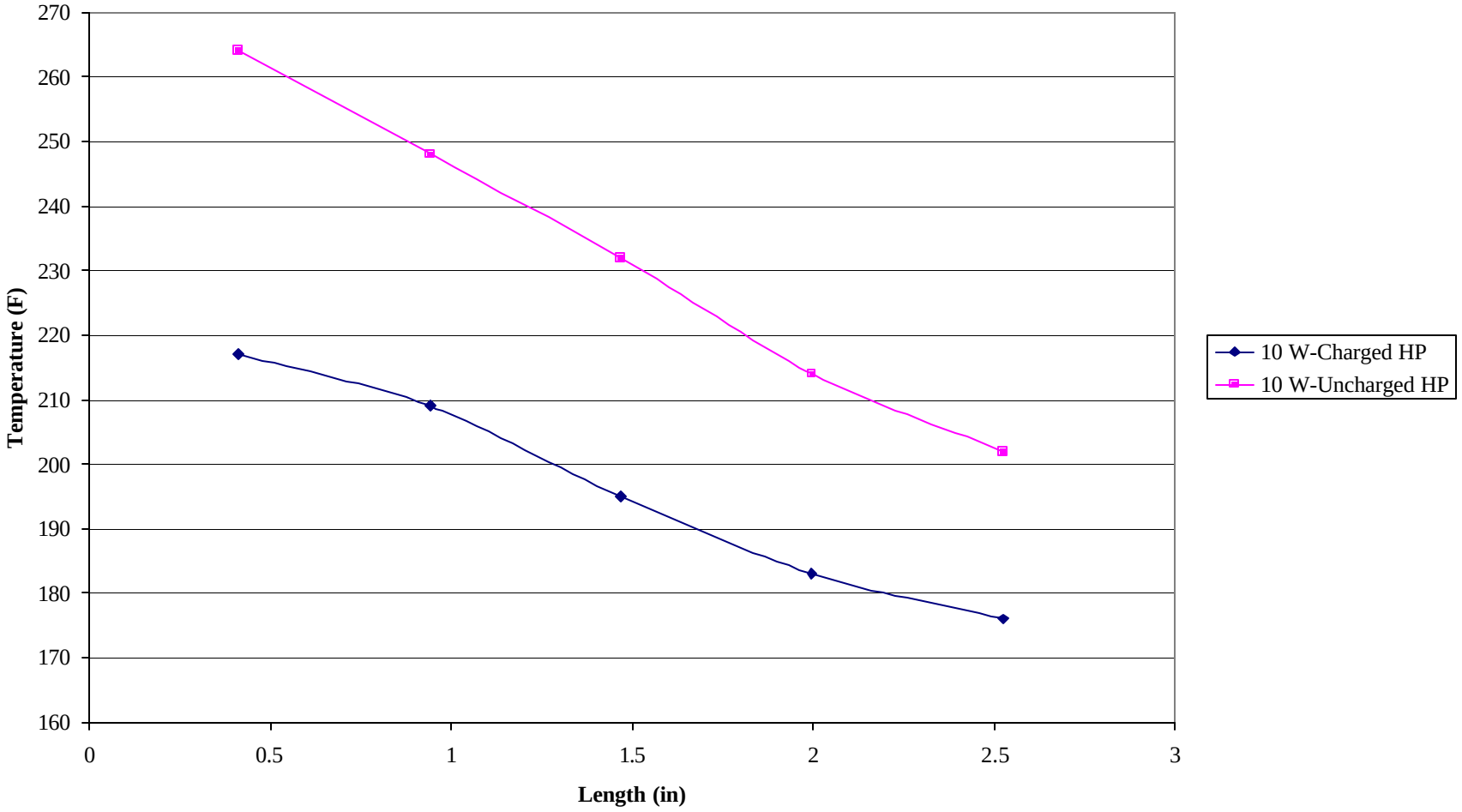

Figure 4.9 FEM temperature distribution along heat pipe length with 10 W of input power.

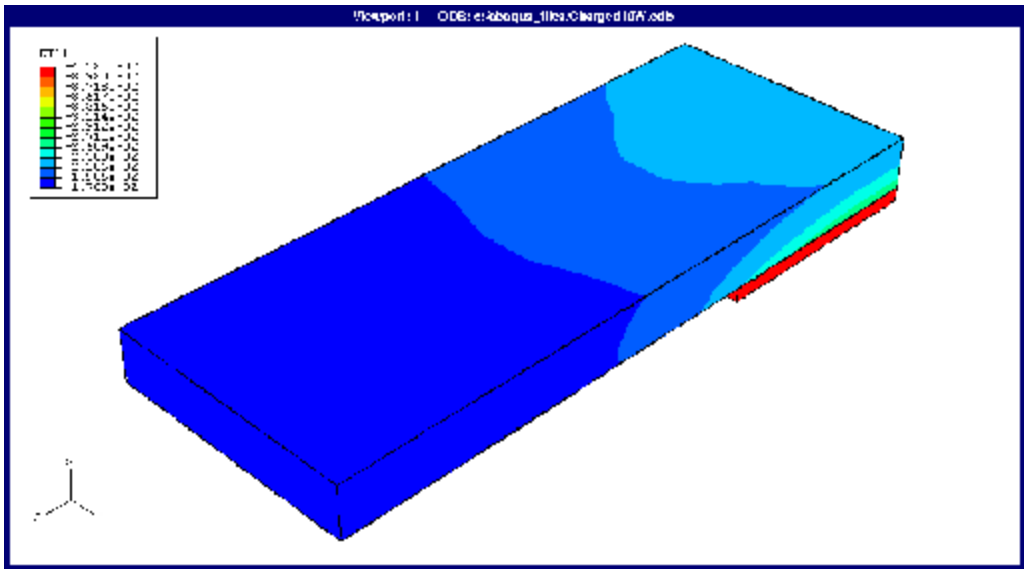

(a)

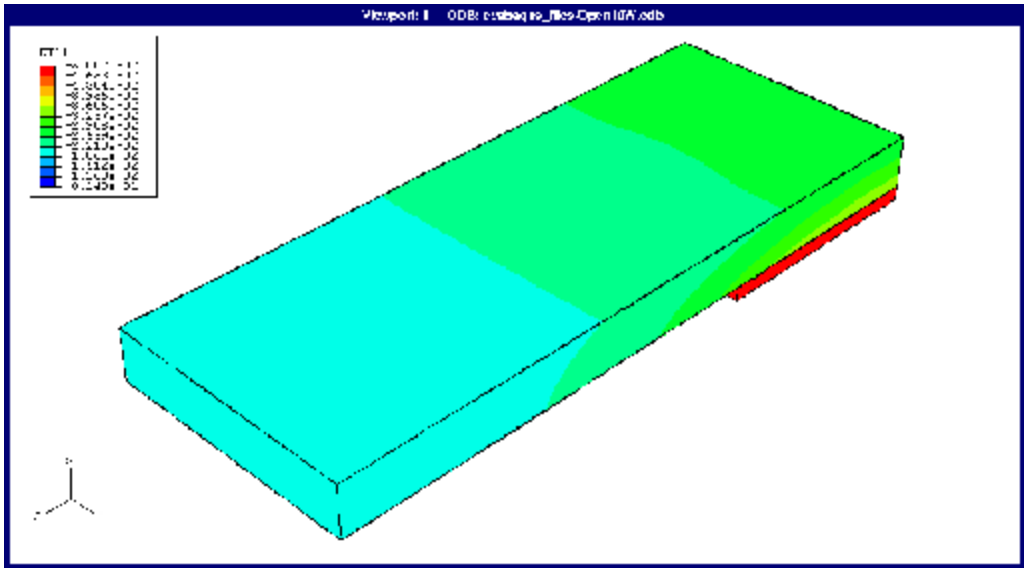

(b)

Figure 4. 10 Temperature distribution top view for 10 W of input power: (a) charged heat pipe, (b) uncharged heat pipe.

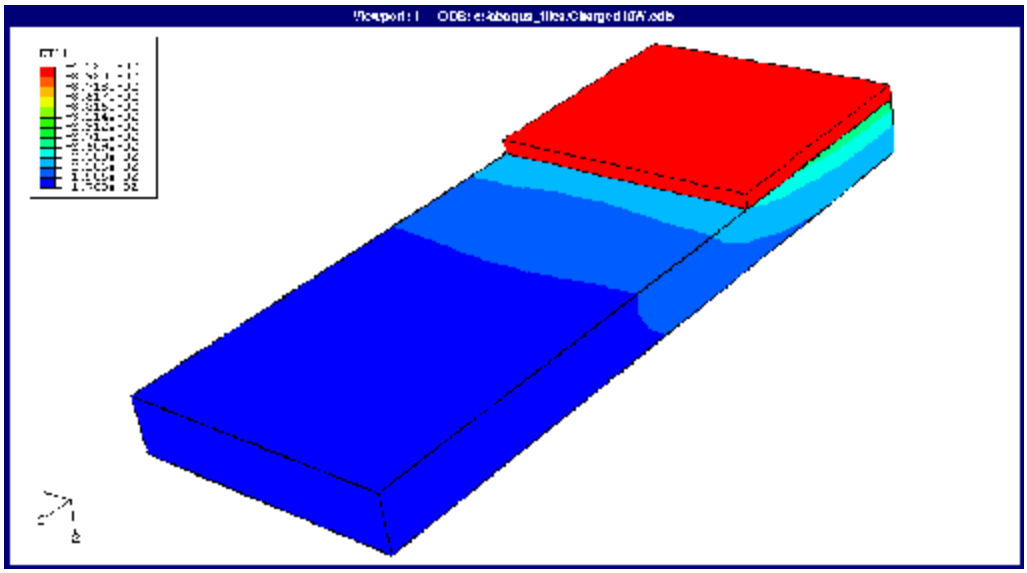

(a)

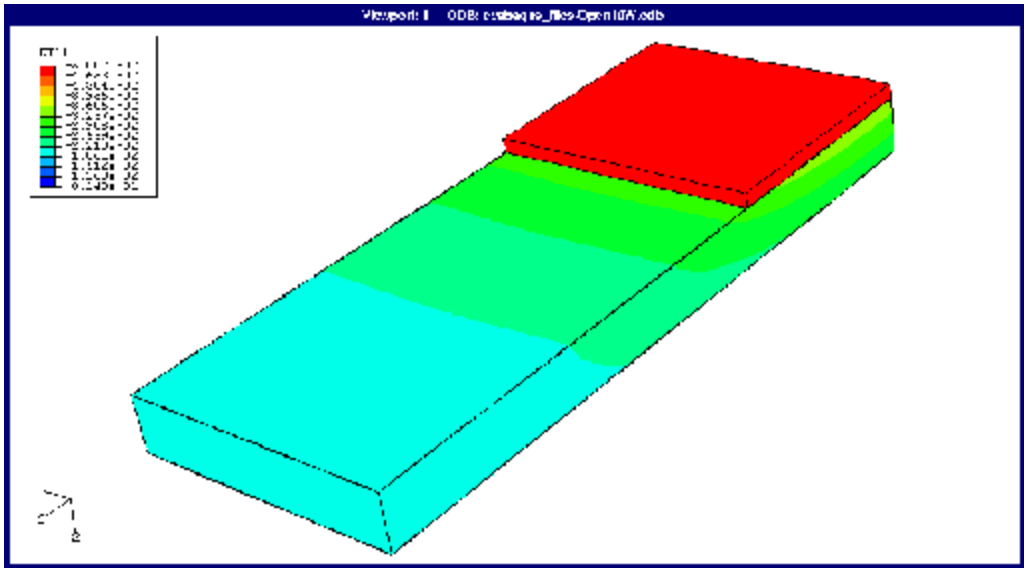

(b)

Figure 4. 11 Temperature distribution bottom view for 10 W of input power: (a) charged heat pipe, (b) uncharged heat pipe.

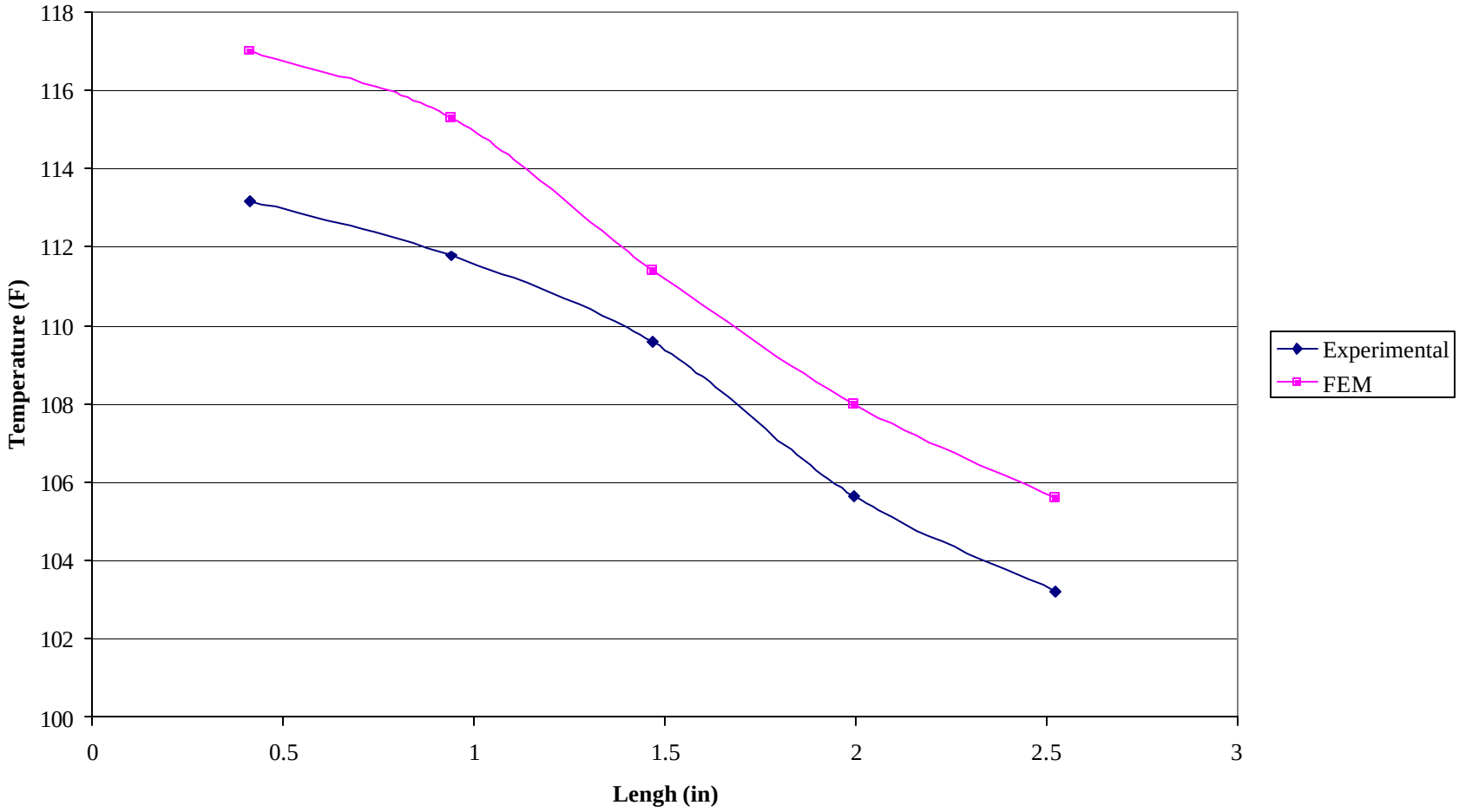

Figure 4. 12 Experimental and FEM temperature distributions along charged heat pipe with 2.5 W of input power.

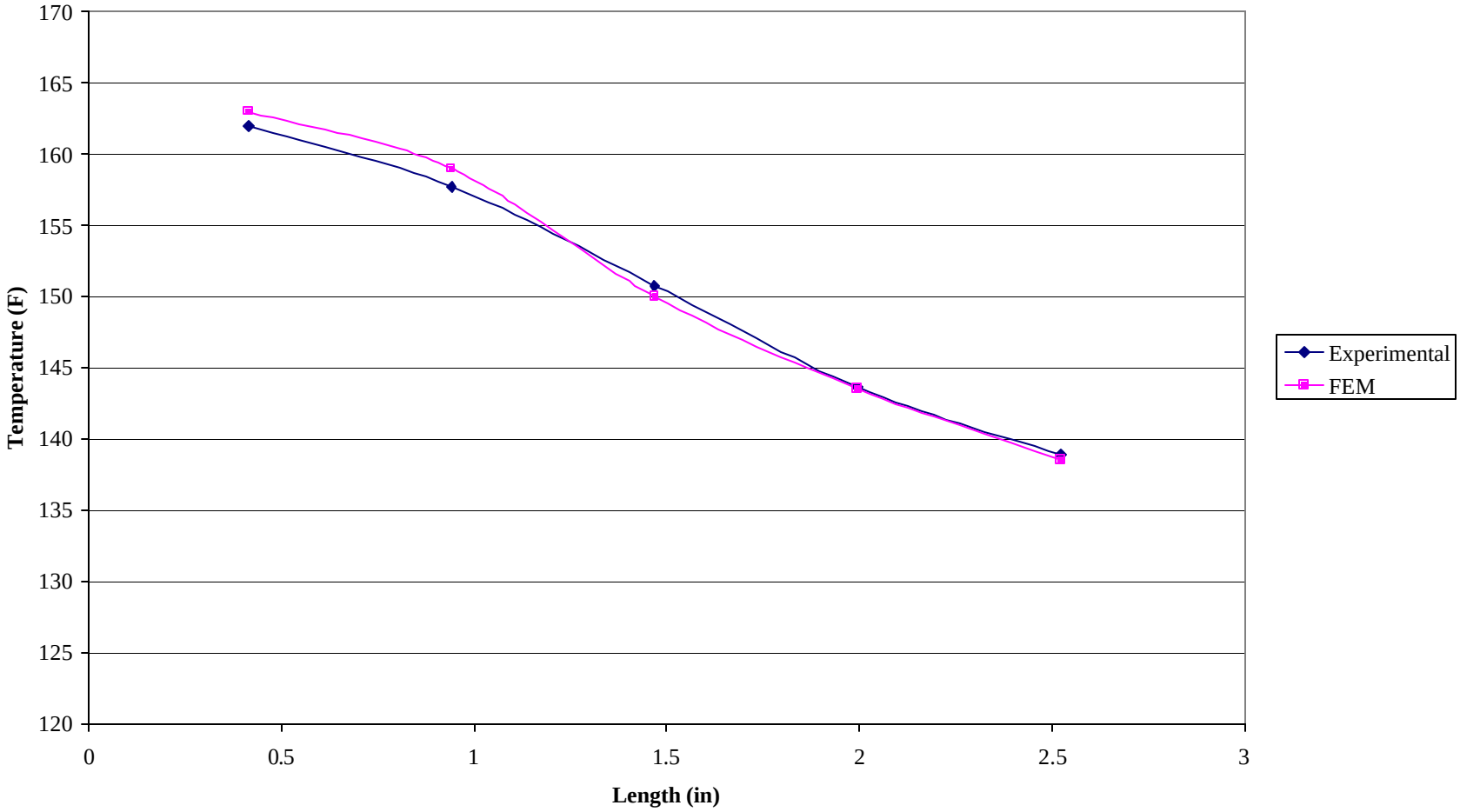

Figure 4.13 Experimental and FEM temperature distributions along charged heat pipe with 5.6 W of input power.

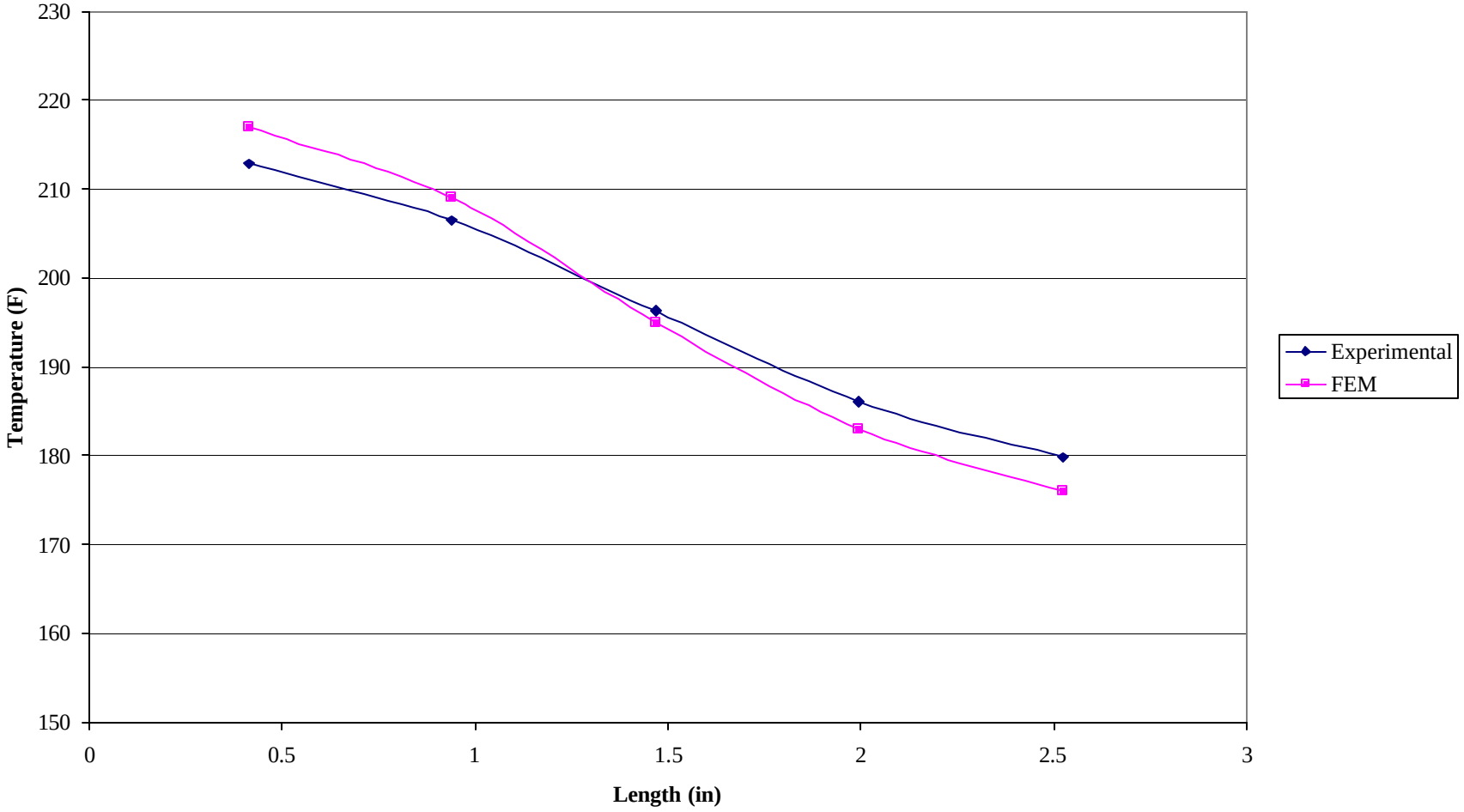

Figure 4.14 Experimental and FEM temperature distributions along charged heat pipe with 10 W of input power.

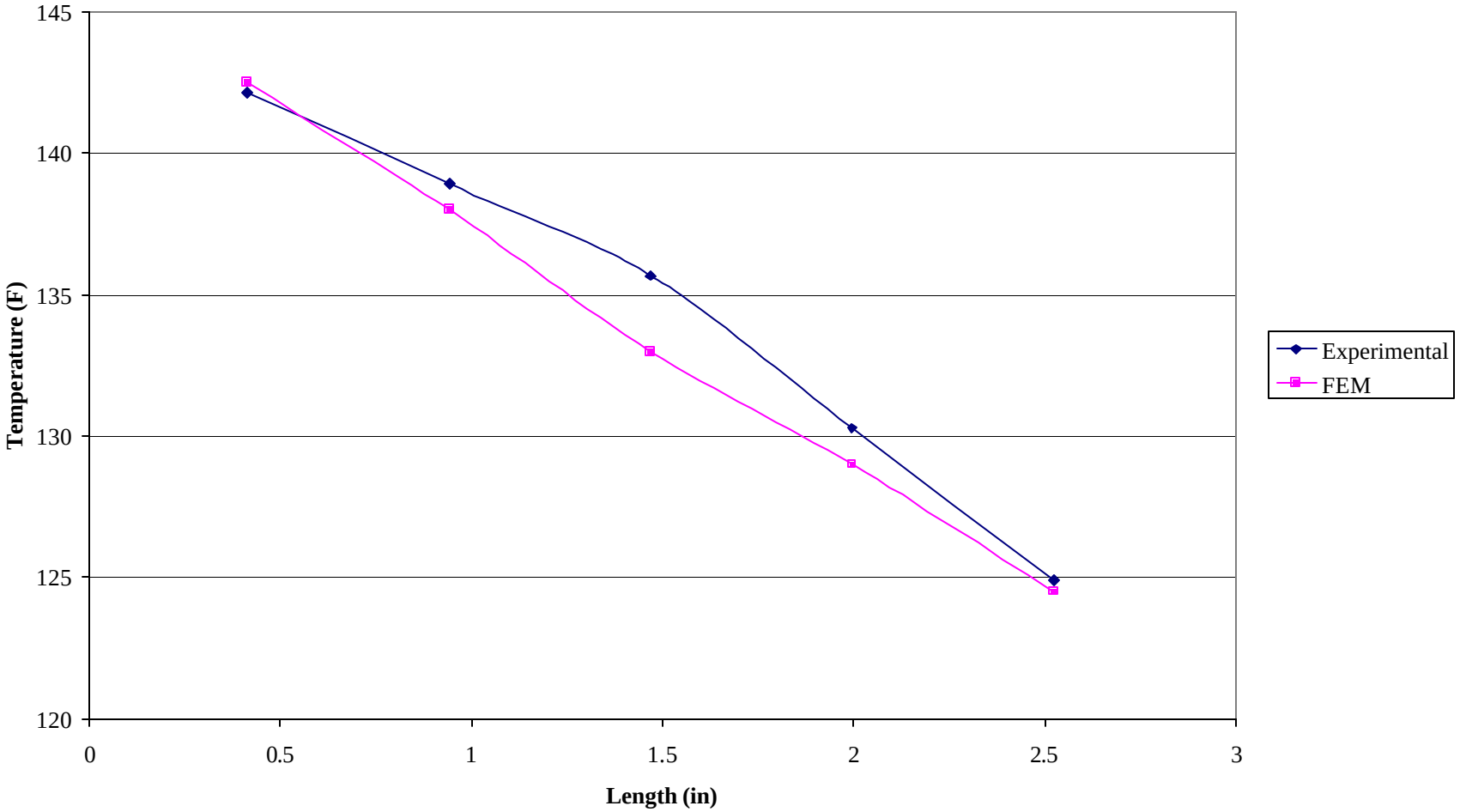

Figure 4.15 Experimental and FEM temperature distributions along uncharged heat pipe with 2.5 W of input power.

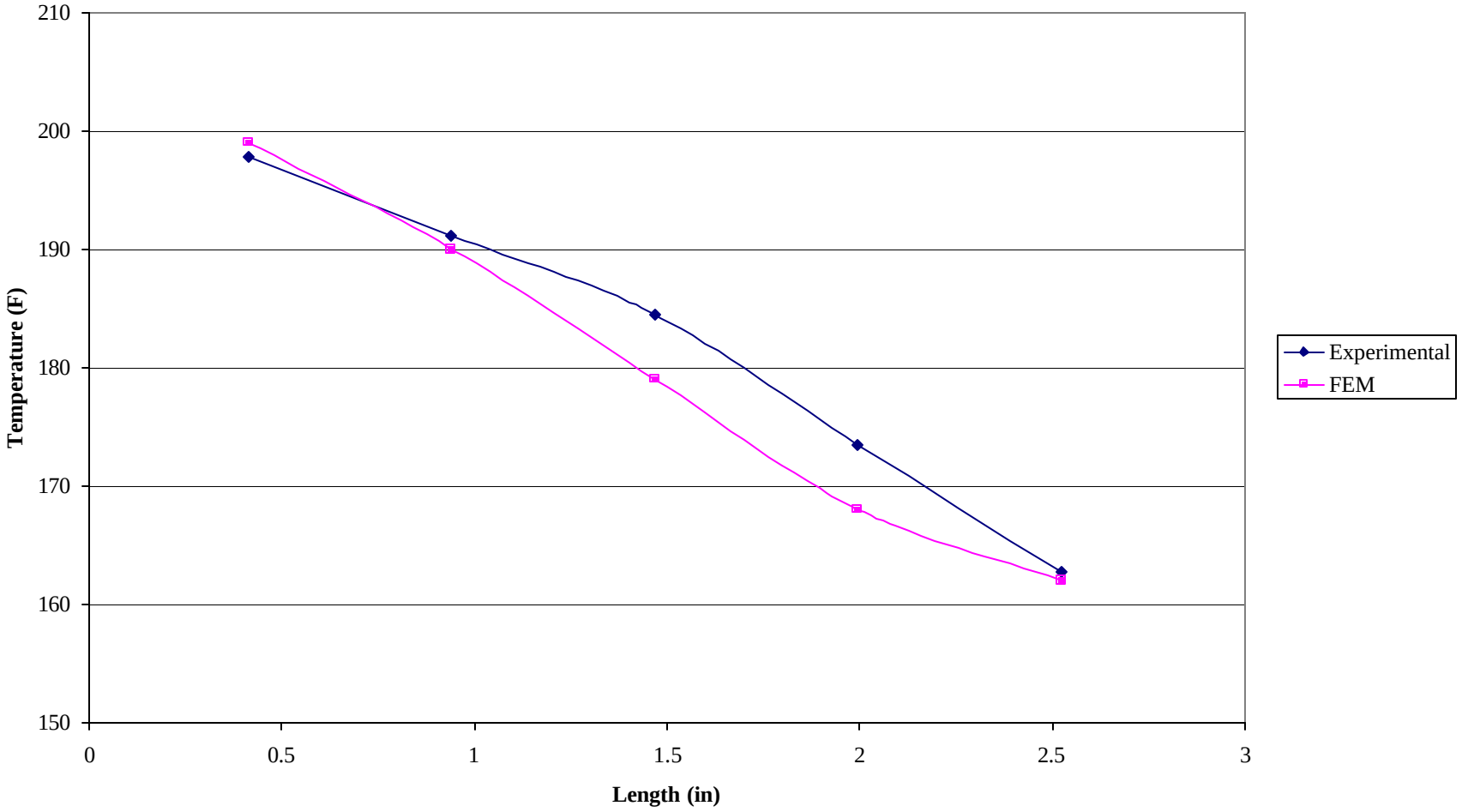

Figure 4.16 Experimental and FEM temperature distributions along uncharged heat pipe with 5.6 W of input power.

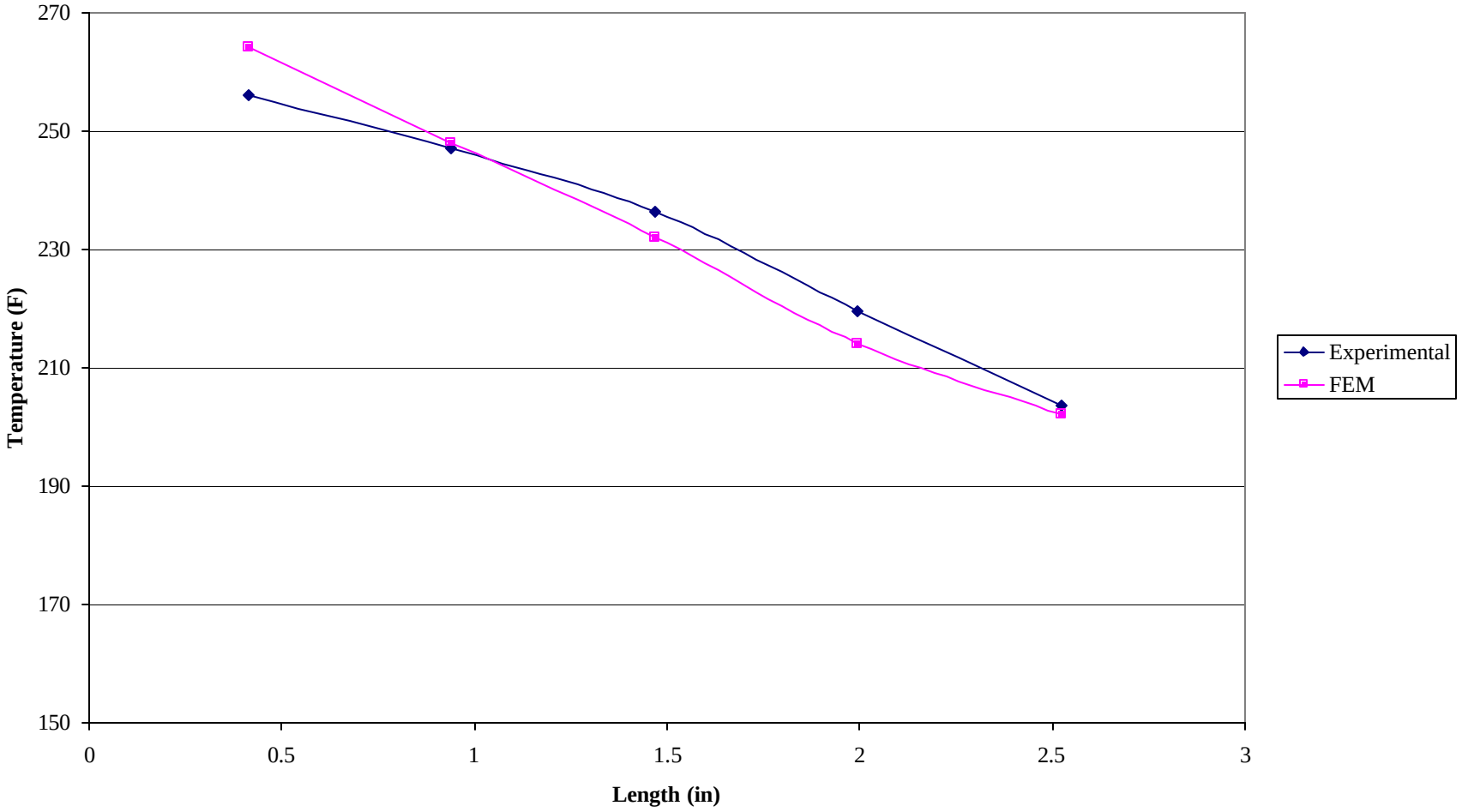

Figure 4.17 Experimental and FEM temperature distributions along uncharged heat pipe with 10 W of input power

4.2 2D Sequentially Coupled Thermal-Stress Analysis of the PWB Cross Section

A sequentially coupled heat transfer analysis is used when the stress/deformation field in a structure depends on the temperature field in that structure, but the temperature field can be found without knowledge of the stress/deformation response. A sequentially coupled heat transfer analysis is performed by first conducting a pure heat transfer analysis and then a stress/deformation analysis.

Nodal temperature are stored as a function of time in the heat transfer results (.fil) file by using the *NODE FILE option and specifying output variable NT.

To define the temperature field at different times in the stress analysis *TEMPERATURE option is used within the stress analysis step definition to read temperatures at the nodes stored in the heat transfer results file. This interface assumes that node numbers are the same for corresponding nodes in the stress analysis mesh and in the heat transfer analysis mesh.

The Vapor Space-1 and Heater-1 part-instances were omitted for stress/displacement analysis to avoid their interaction with the rest of the structural elements of the model. Nodes from Vapor Space-1 and Heater-1 part-instances were removed for the stress problem using the *MODEL CHANGE option. When the results file is read during the stress analysis, temperature at nodes that are not in the mesh are ignored.

4.2.1 Assumptions

The numerical analysis was conduced under the following assumptions:

(1) The stress/deformation field depends on the temperature field, but the temperature field can be found without knowledge of the stress/deformation response.

(2) Inertia effects are neglected.

(3) Ignores time-dependent material effects (creep, swelling, viscoelasticity).

(4) Heat transfer coefficient from test printed circuit board to air has a constant value irrespective of location and/or shape.

(5) The ambient air temperature is constant.

(6) A printed circuit board cross section model has a shape dimensions as shown in Figure 2.6.

(7) Every member has a constant thermal conductivity irrespective of temperatures.

(8) Contact resistance is constant between the heating element and the printed circuit board.

4.2.2 Model Definition

In the heat transfer analysis all components are modeled using a four-node convection diffusion quadrilateral linear element, while in the stress/deformation analysis all the components are modeled using a four-node bilinear plane strain quadrilateral linear element. Table 4.3 lists the material properties of the different parts of the heat pipe assembly. These parts can be seen in Figure 4. 18.

Table 4.3 2D Thermal-Stress Model material properties.

	Conductivity [W/m°K]			Density [g/cm^3]	Specific Heat [J/kg°K]	Modulus of Elasticity GPa	Poisson's Ratio	Coefficient of Thermal Expansion 10^{-6} (°C)$^{-1}$		
Copper Layer	398			8.96	385	110	0.35	16.5		
FR-4	X 7.61	Y 0.48	Z 7.61	1.90	1150	17.4	0.19	X 14	Y 175	Z 13
Vapor Space	X 80	Y 400	Z 80	8.96	385	110	0.35	16.5		
Heater	398			8.96	385	110	0.35	16.5		
Copper Plating	398			8.96	385	39.36	0.35	16.5		

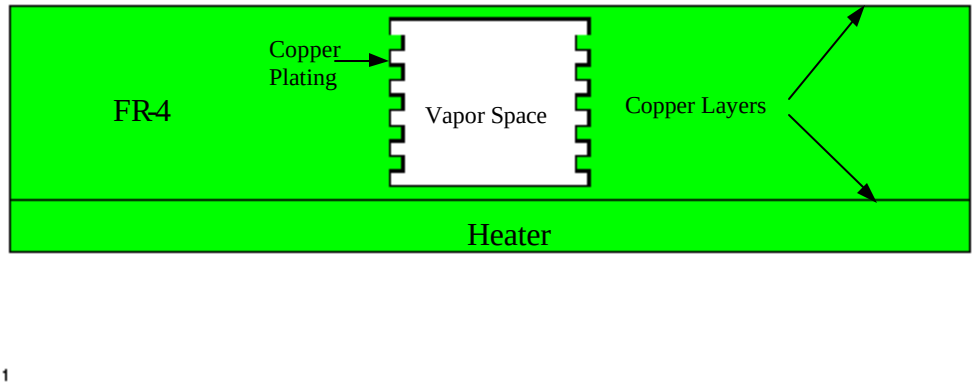

Figure 4. 18 PWB Cross Section Model.

4.2.3 Element Selection

The element selected in the heat transfer analysis for the all mesh model components is the 4-node convection diffusion quadrilateral linear element ABAQUS type DCC2D4. This element holds temperature as active degree of freedom [17].

The element selected for the all mesh model components in the stress/displacement analysis is the 4-node bilinear plane strain quadrilateral linear element ABAQUS type CPE4R. This element holds 1, 2 (u_x, u_y) as active degree of freedom [17].

4.2.3.1 Surface Contact Interaction

The *Tie Surface Interaction* was used to fuse together all part-instances surfaces in contact even though the meshes created on the surfaces may be dissimilar. Creating a tie surface interaction is analogous to including the *CONTACT PAIR, TIED option in a solver input file.

In the heat transfer analysis the *Thermal Film Condition* is used to define the cooling due to convection of all surfaces of the model expose to the surrounding. A film condition interaction is analogous to including the *SFILM option in a solver input file.

Radiation to Ambient Interaction is used in the heat transfer analysis to model heat transfer between the nonconcave surface of the model and a nonreflecting environment due to radiation. A radiation interaction is analogous to including the *SRADIATE option in a solver input file.

4.2.4 Mesh Discretization

Structure meshing was used since it gives most control over the mesh because it applies pre-established mesh patterns to particular model topologies. The FR-4-1 part-instance was too complex to be meshed using pre-established mesh patterns directly. Consequently, it had to be partitioned into simple regions with topologies for which

structured meshing pattern exits. The total number of elements is 1550 and nodes 2443. Table 4.4 shows the mesh break down by part-instances.

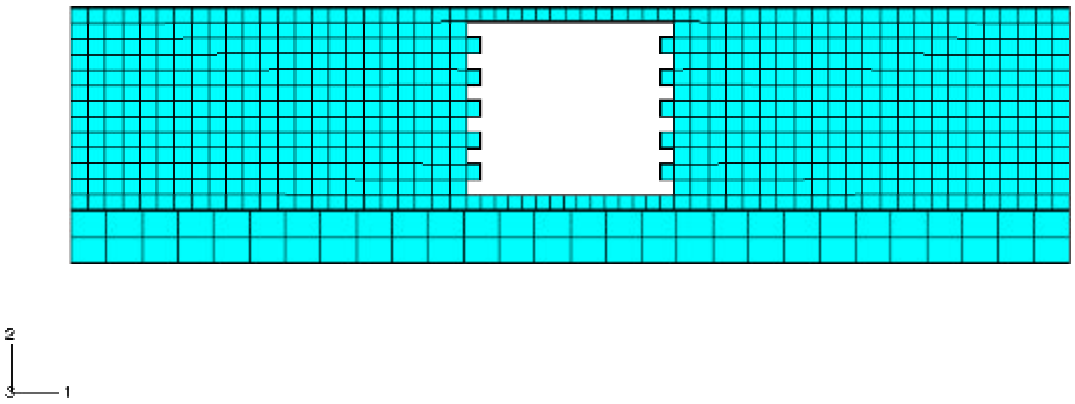

Figure 4.19 Meshed Model

Table 4.4 Part-instance mesh break down

PART-INSTANCE	HEAT TRANSFER ELEMENT TYPE	STRESS/DISPLACEMENT ELEMENT TYPE	NODES	ELEMENTS
Copper Layer-1	Linear quadrilateral DCC2D4	Linear quadrilateral CPE4R	452	225
Copper Layer-2	Linear quadrilateral DCC2D4	Linear quadrilateral CPE4R	452	225
FR-4-1	Linear quadrilateral DCC2D4	Linear quadrilateral CPE4R	746	637
Vapor Space-1	Linear quadrilateral DCC2D4	Linear quadrilateral CPE4R	180	144
Heater-1	Linear quadrilateral DCC2D4	Linear quadrilateral CPE4R	87	56
Copper Plating	Linear quadrilateral DCC2D4	Linear quadrilateral CPE4R	526	263
		TOTAL	2443	1550

4.2.5 Loading Conditions

The loading condition attempt to simulate the heat generated in the heater. Three heat inputs levels will be analyzed: 2.5 W (22.121 in lb./s), 5.6 W (49.551 in lb./s), and 10 W (88.485 in lb./s). The *DSFLUX option was used to specify the distributed surface fluxes in the heater.

4.2.6 Initial Conditions

By default the initial temperature of all nodes is zero. The TYPE=TEMPERATURE parameter is used on the *INITIAL CONDITIONS option to specify nonzero initial temperatures.

4.2.7 Boundary Conditions

Only zero-valued boundary conditions can be prescribed as model data. The data lines can be specified using either “type” or “direct” format. The “Type” format is a way of conveniently specifying common types of boundary conditions in stress/displacement analyses.

For “type” format the first entry on the data line is the node set or node number to which the boundary conditions apply. The following entries specify the degrees of freedom to be restrained at that node or node set. Either a single degree of freedom or the first and last of a range of degree of freedom can be specified directly on the data lines of the *BOUNDARY option. The bottom corners of the FR-4 part instance are constrained in d.o.f u_2 (vertical displacement) (see Figure 4.20).

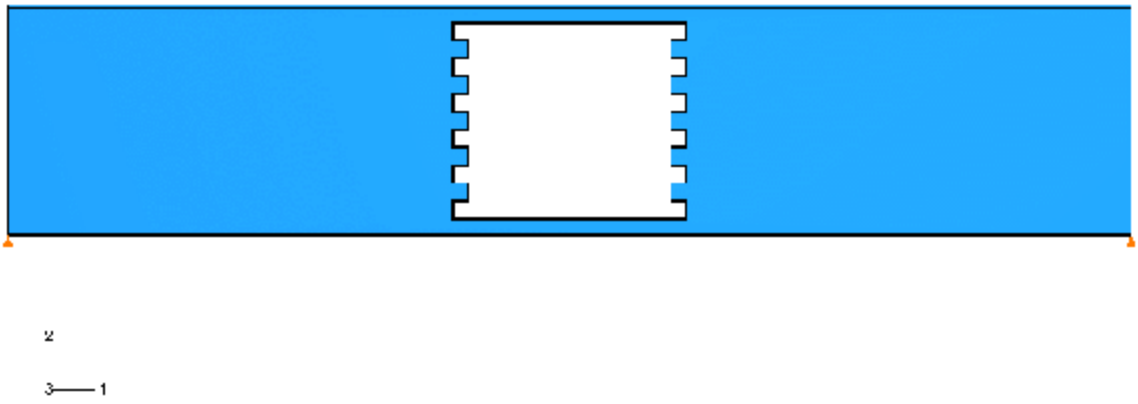

Figure 4.20 2D Stress Analysis Model Boundary Conditions.

4.2.8 Type of Analysis

The sequentially coupled heat transfer analysis is performed running first an uncoupled heat transfer analysis followed by a stress/deformation analysis run. Nodal temperature is stored at the heat transfer analysis in the heat transfer results (.fil) file and subsequently it is read at the stress/displacement analysis.

Uncoupled heat transfer analysis is a pure heat transfer analysis using heat transfer elements and the *HEAT TRANFER procedure. This is linear, steady state, heat transfer analysis used to model solid body heat conduction with general, constant thermal conductivity irrespective of temperatures, internal energy generated in the heater, and quite general convection and radiation boundary conditions.

Stress/deformation analysis is linear, steady state, static analysis and the *STATIC procedure is used to perform this analysis. The response is caused by temperatures varying with time based on the previous transient heat transfer run.

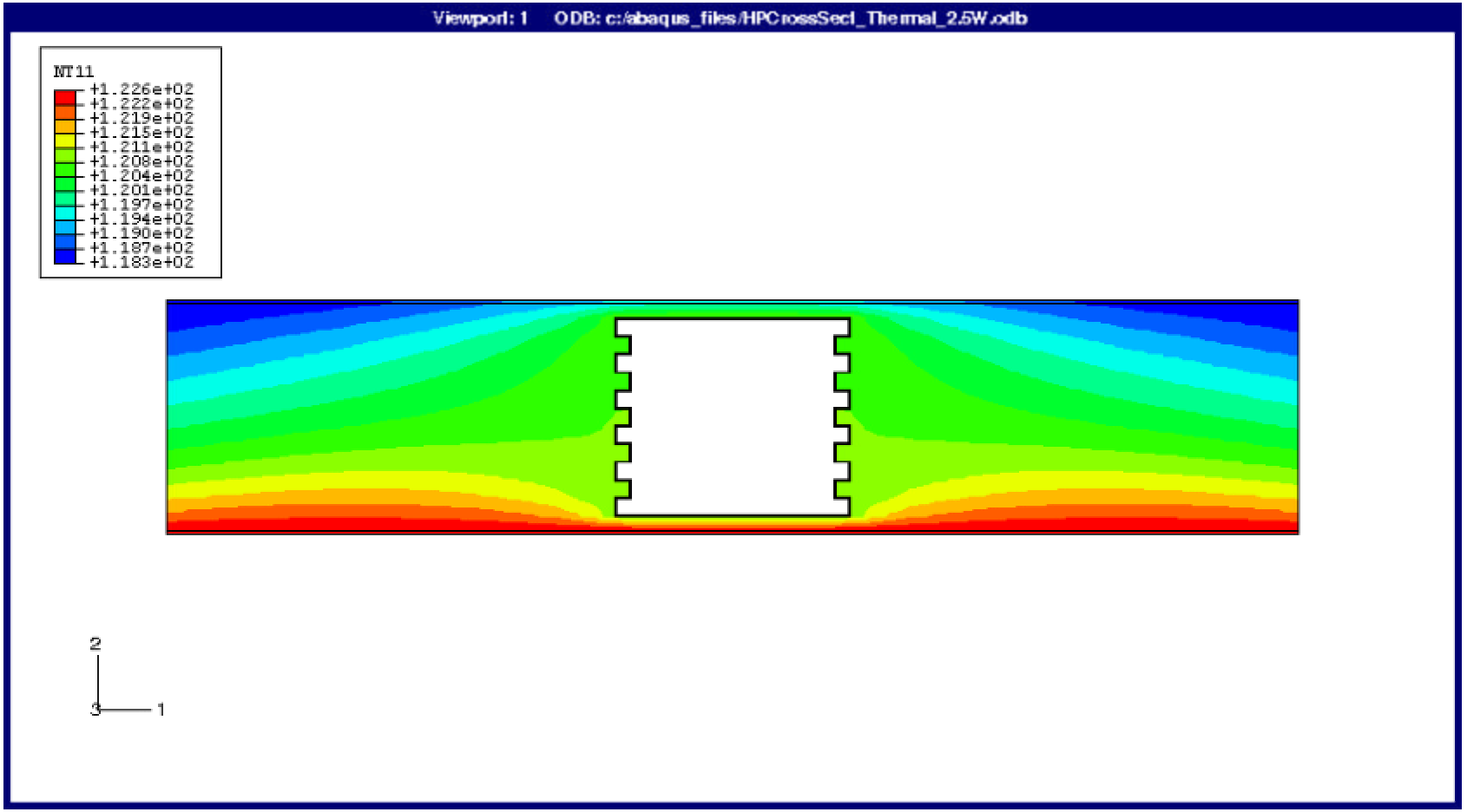

Figure 4.21 Temperature Distribution at point T1 with 2.5 W of input power.

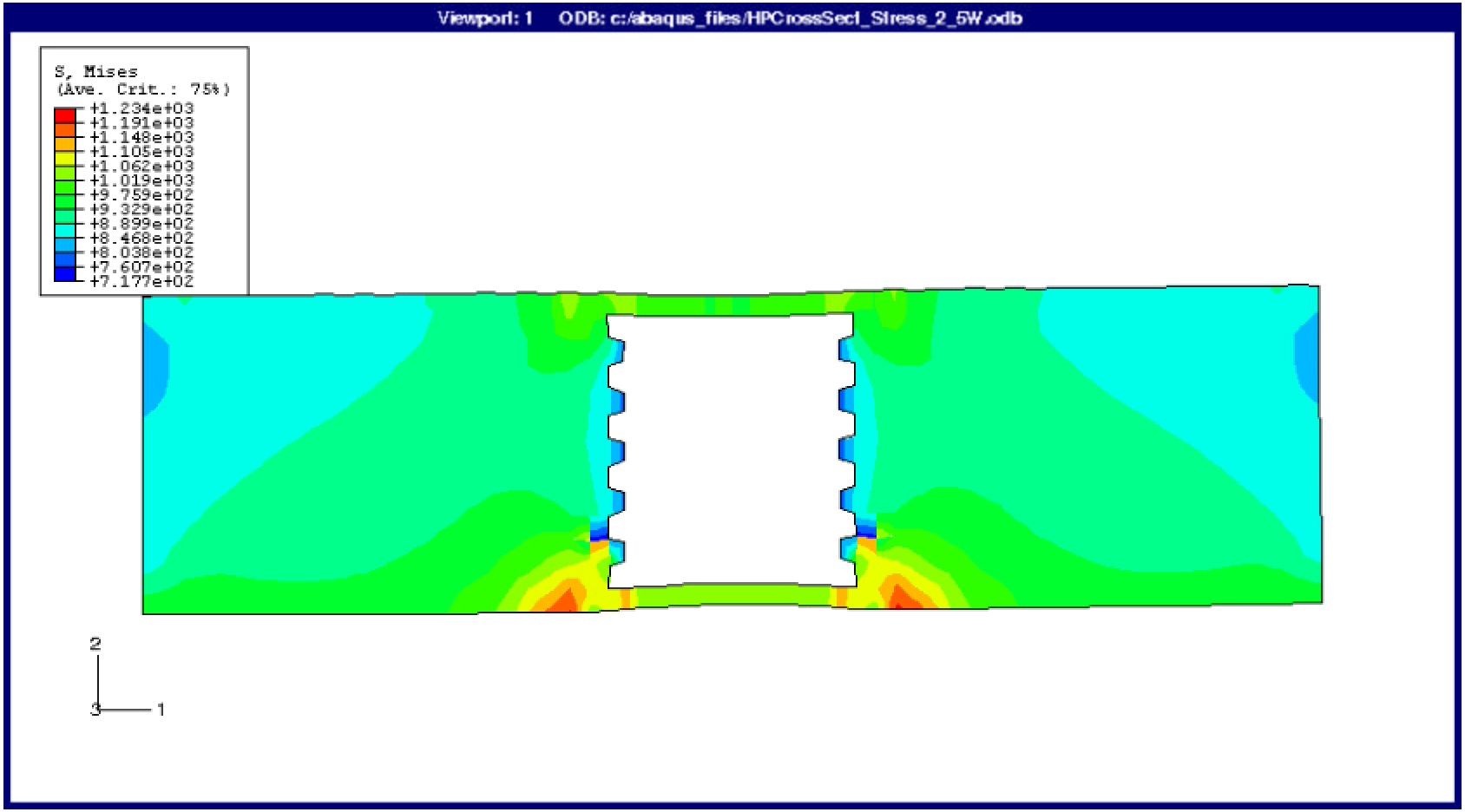

Figure 4.22 Mises stress at point T1 with 2.5 W of input power.

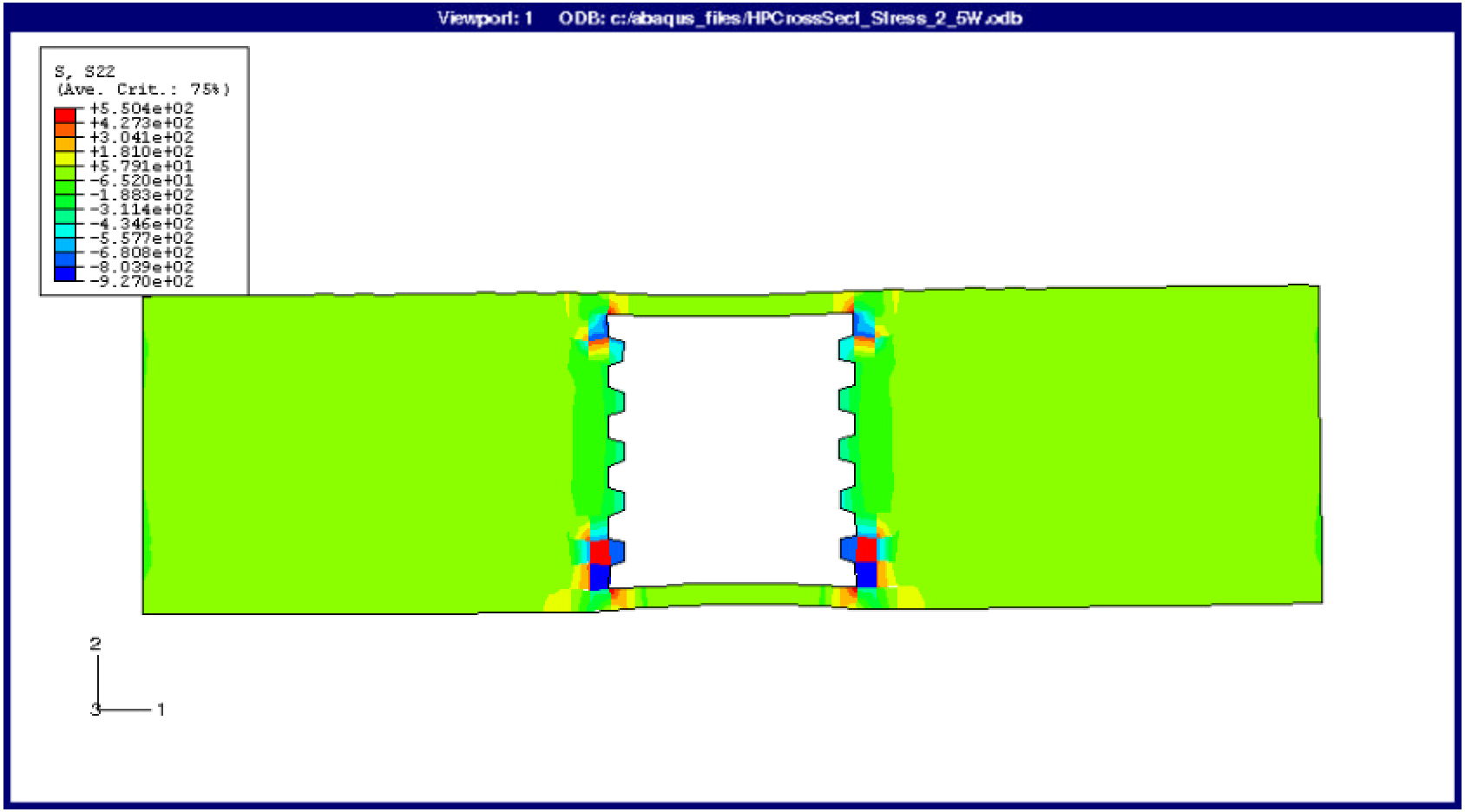

Figure 4.23 S22 stress at point T1 with 2.5 W of input power.

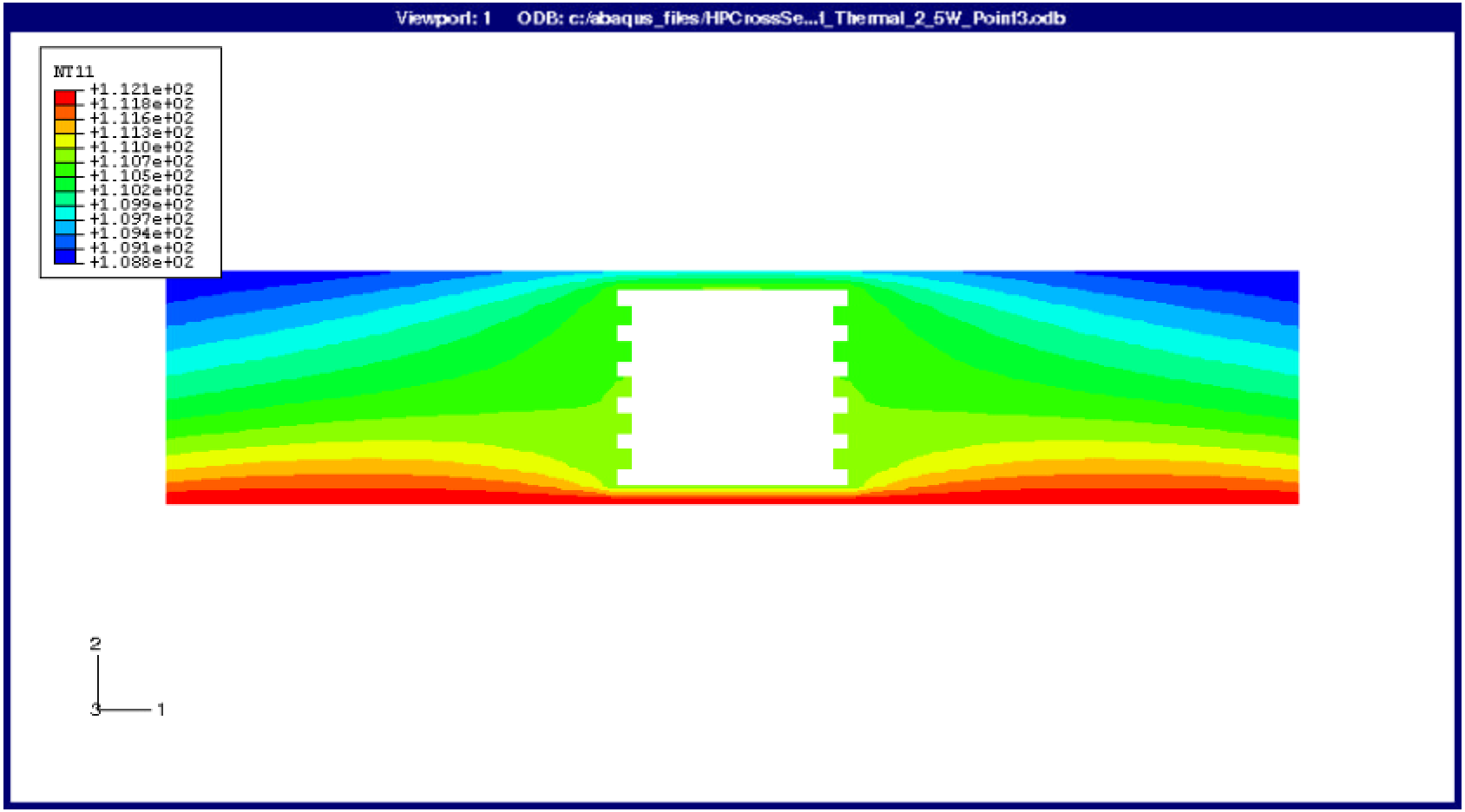

Figure 4.24 Temperature Distribution at point T3 with 2.5 W of input power.

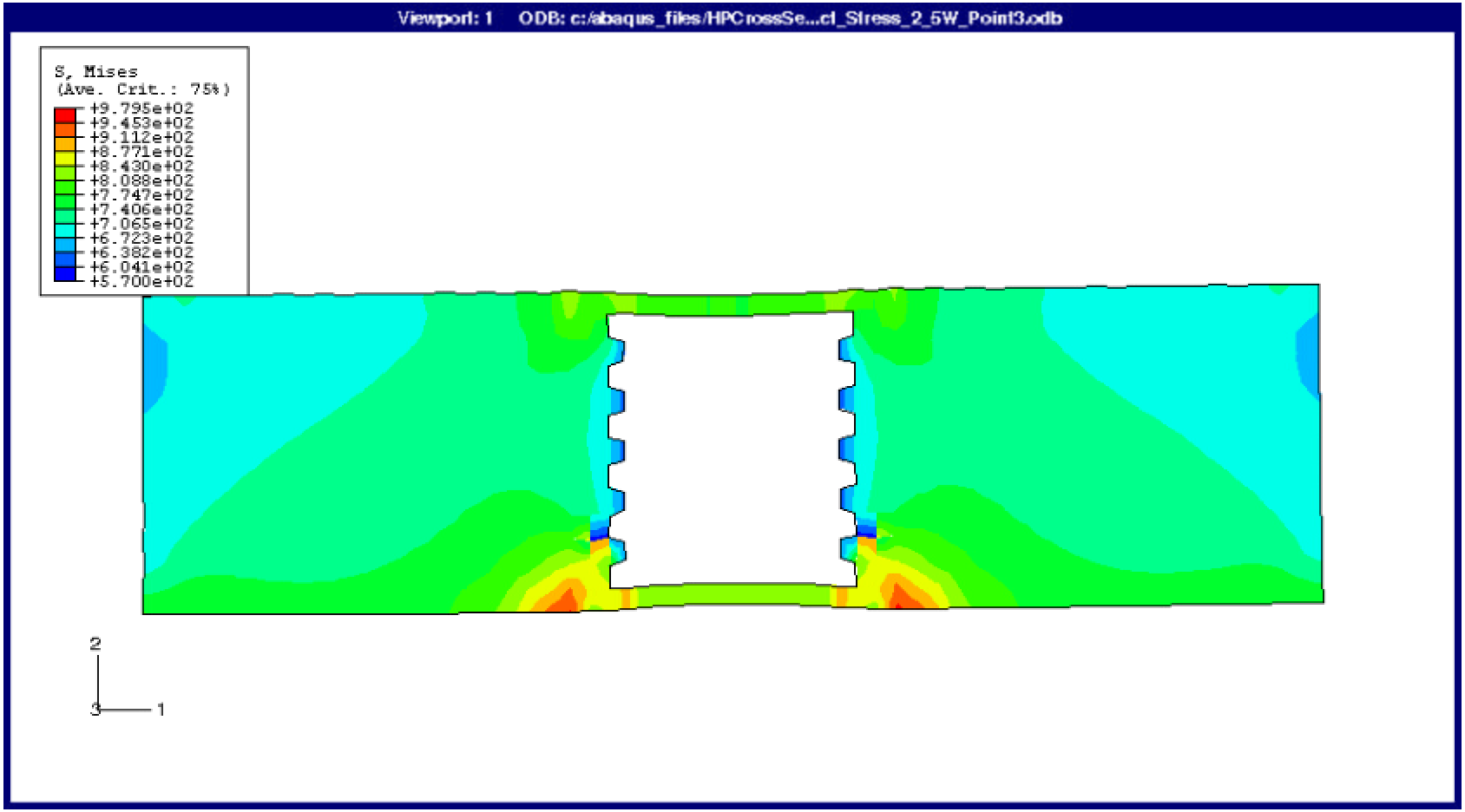

Figure 4.25 Mises stress at point T3 with 2.5 W of input power.

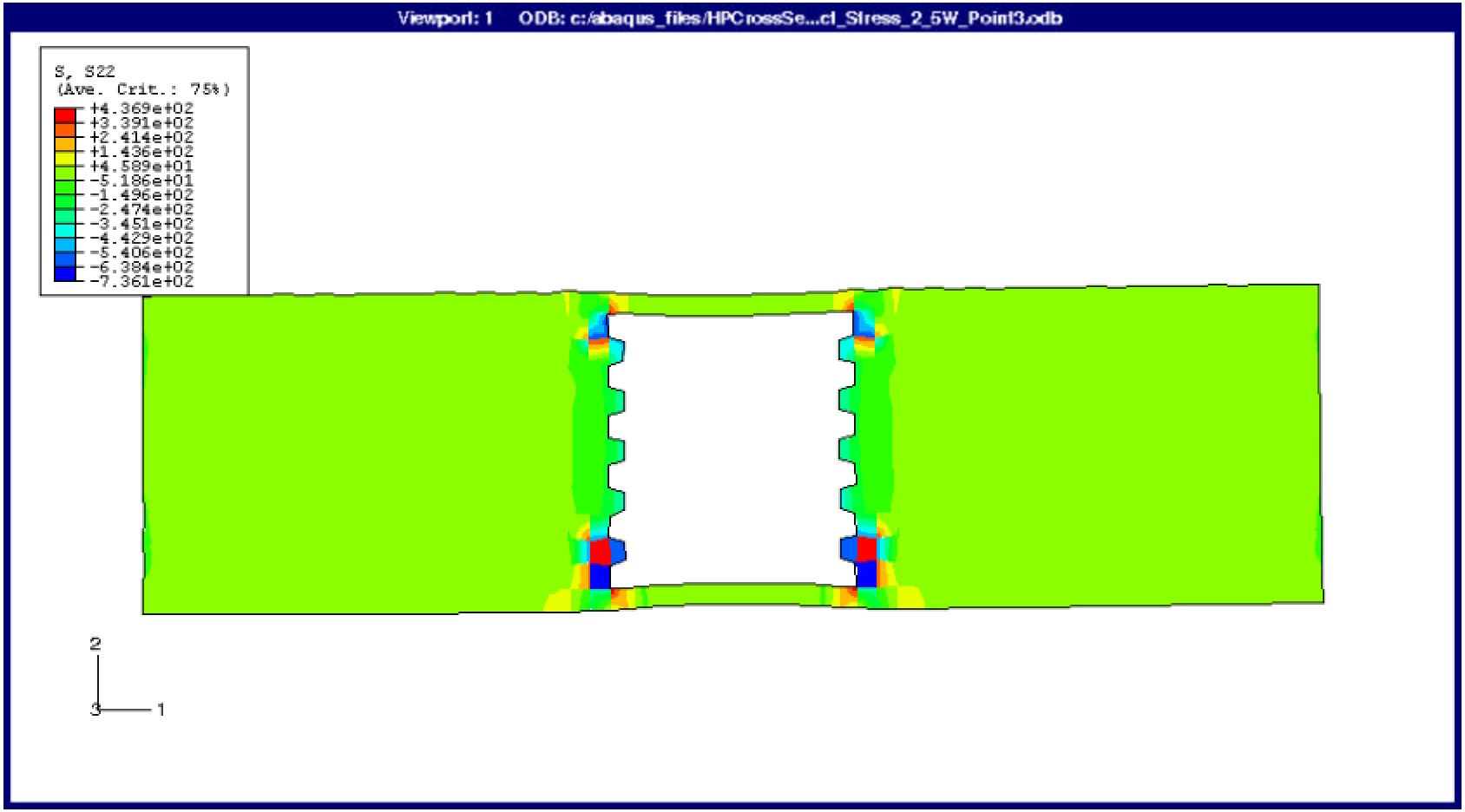

Figure 4.26 S22 stress at point T3 with 2.5 W of input power.

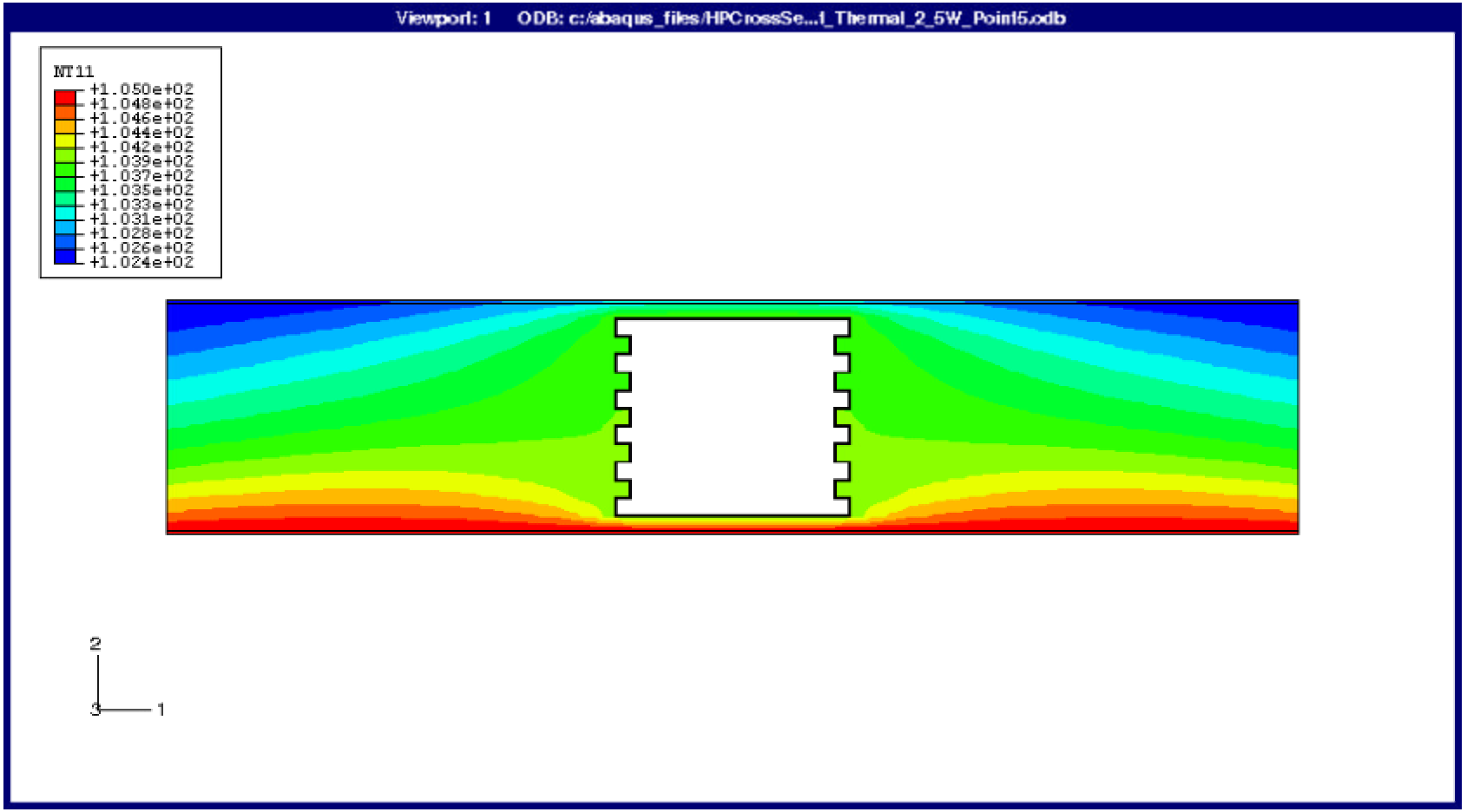

Figure 4. 27 Temperature Distribution at point T5 with 2.5 W of input power.

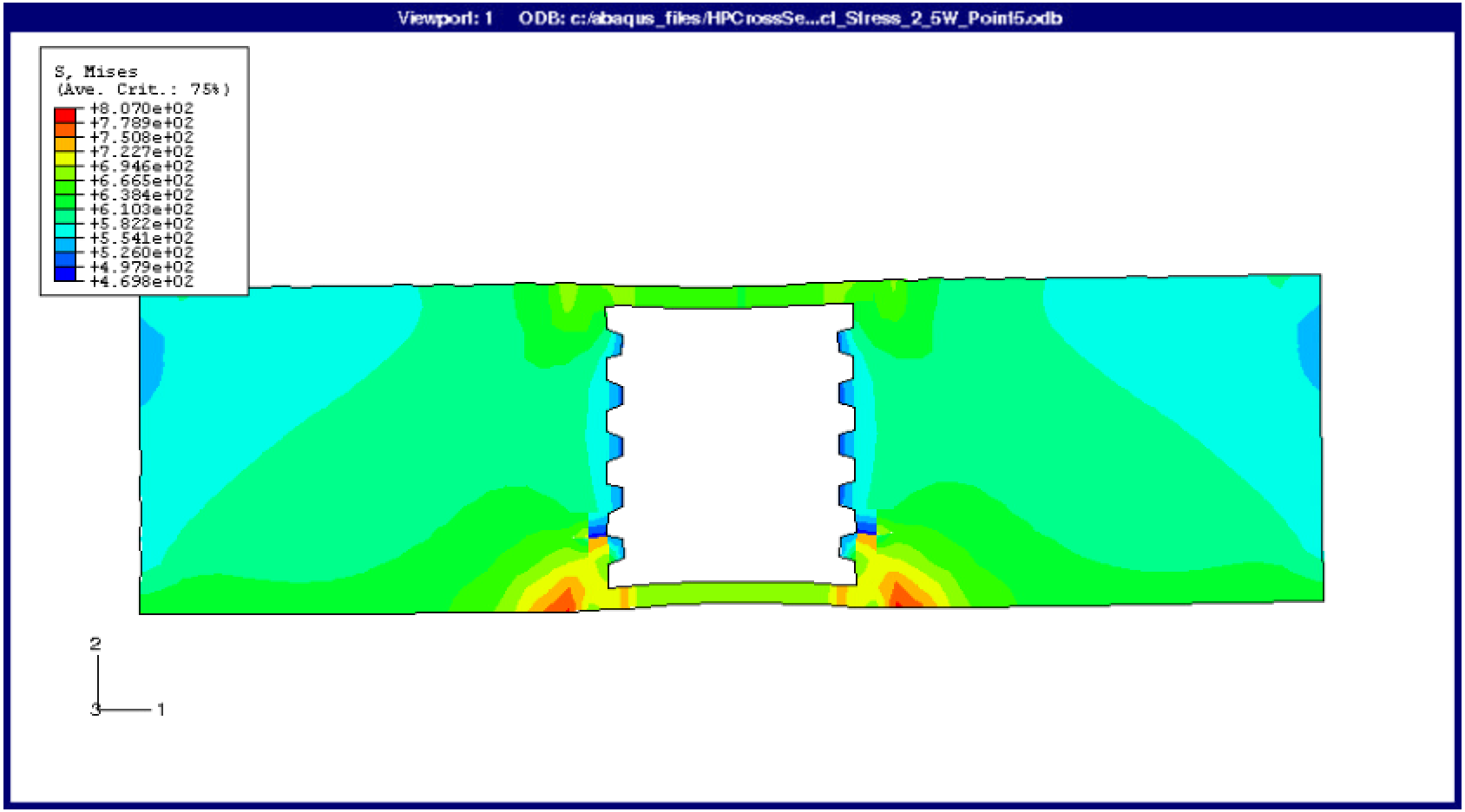

Figure 4. 28 Mises stress at point T5 with 2.5 W of input power.

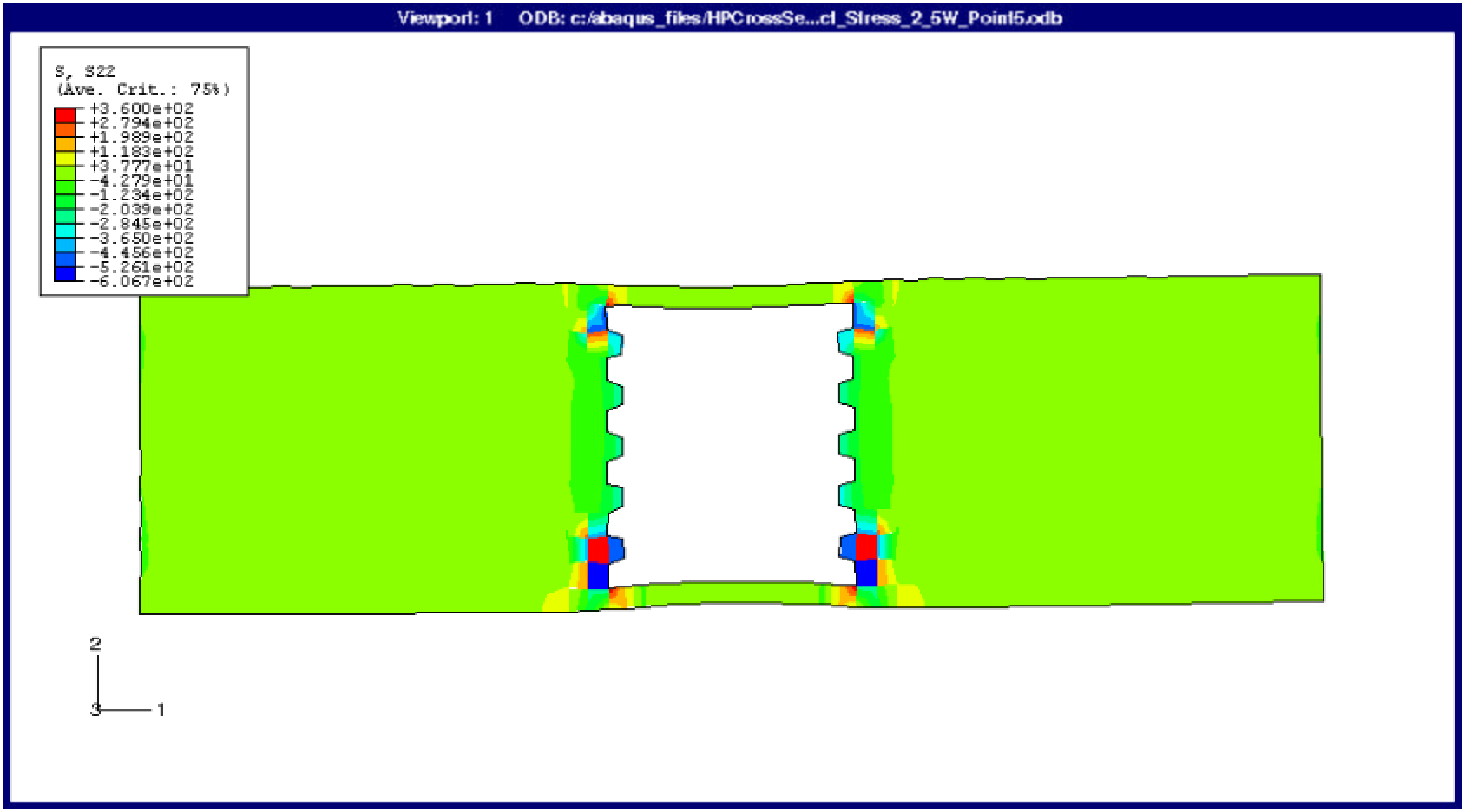

Figure 4.29 S22 stress at point T5 with 2.5 W of input power.

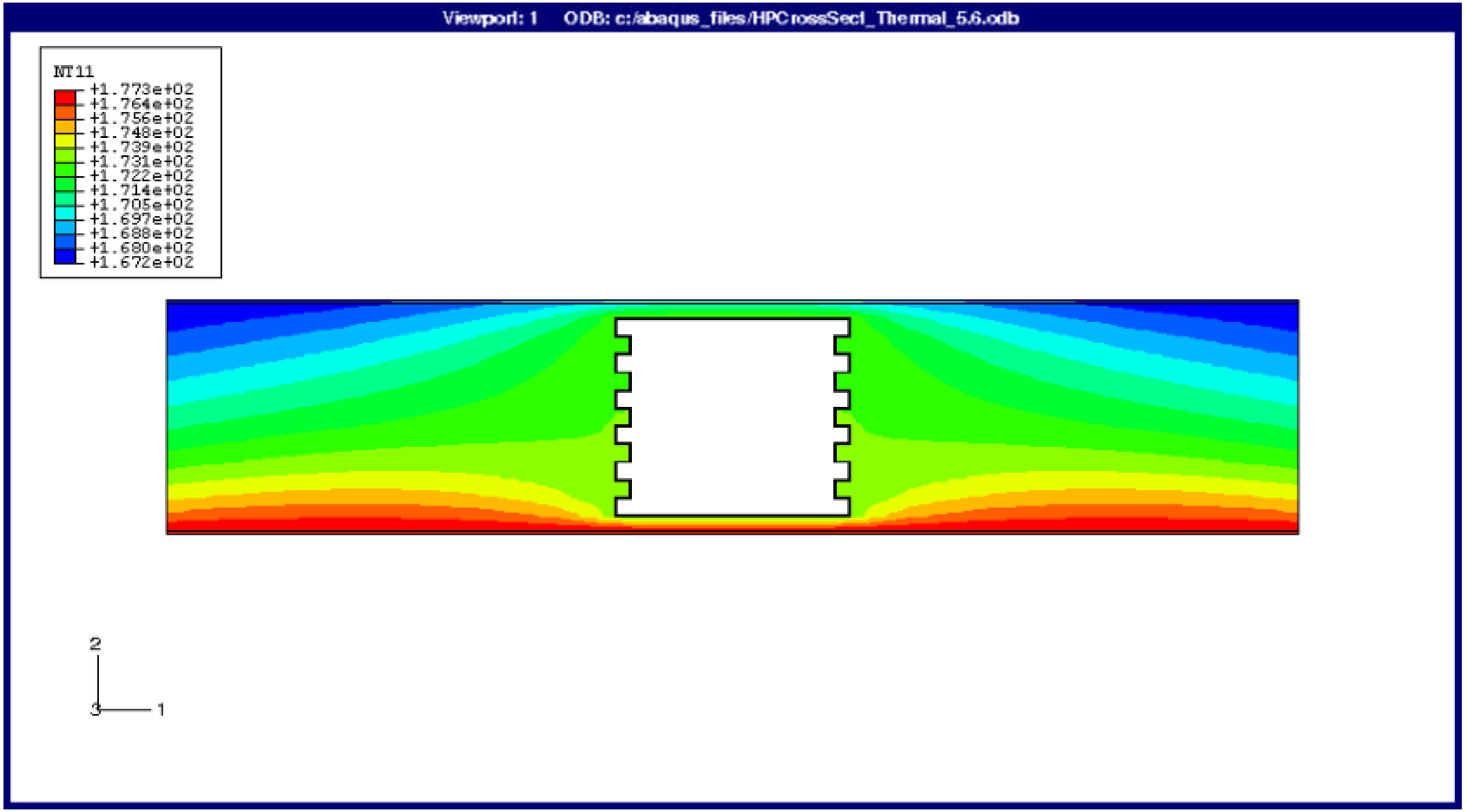

Figure 4.30 Temperature Distribution at point T1 with 5.6 W of input power.

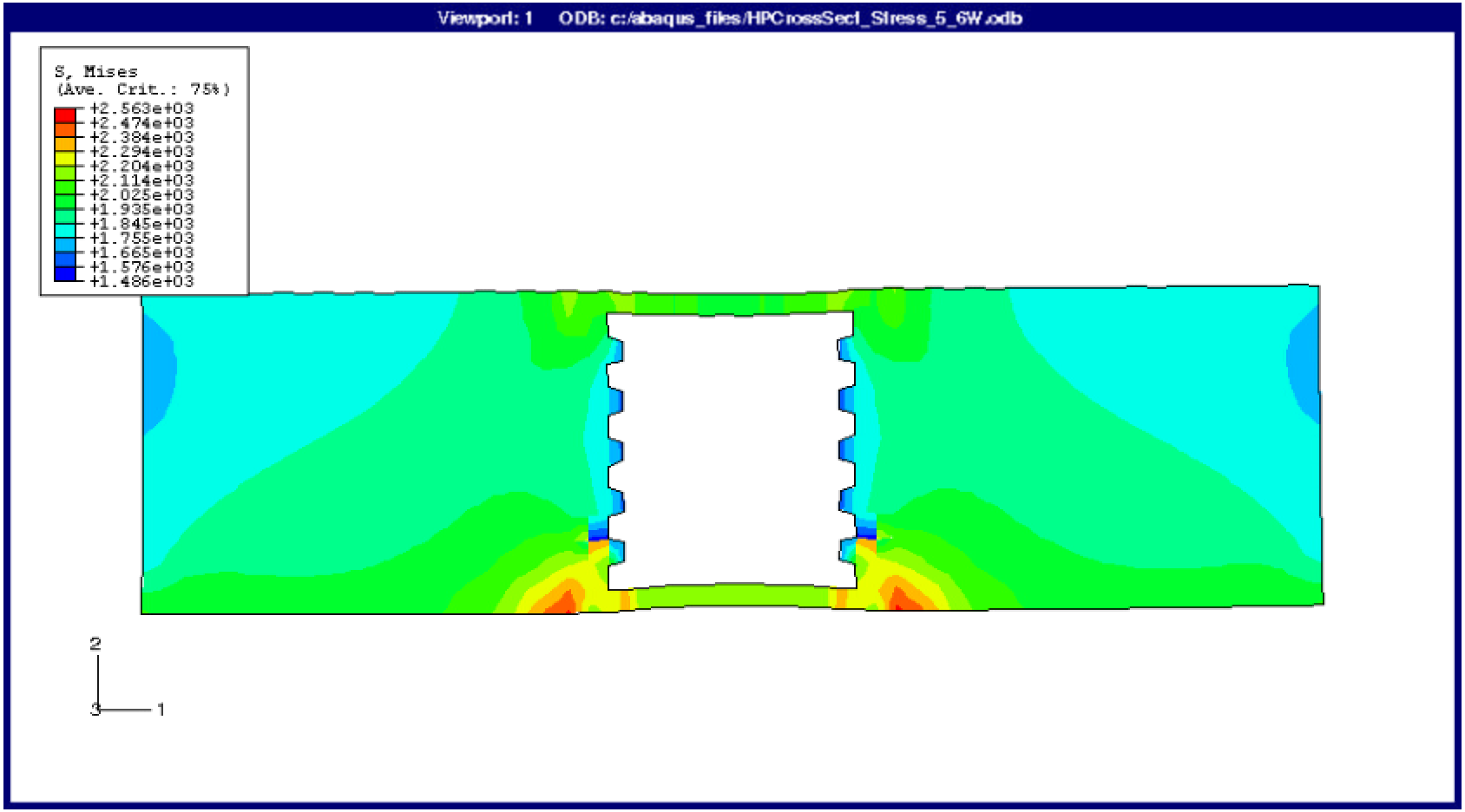

Figure 4.31 Mises stress at point T1 with 5.6 W of input power.

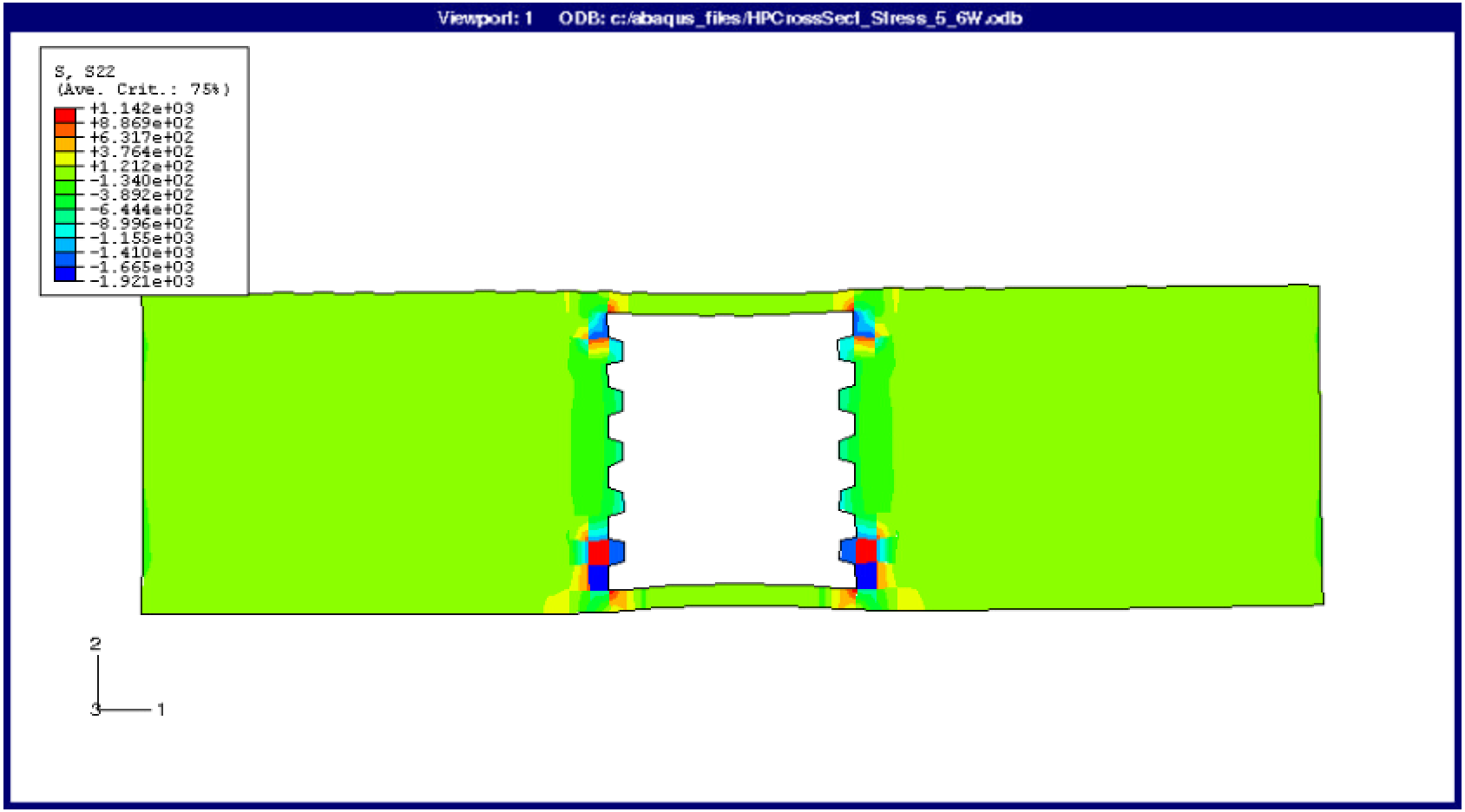

Figure 4.32 S22 stress at point T1 with 5.6 W of input power.

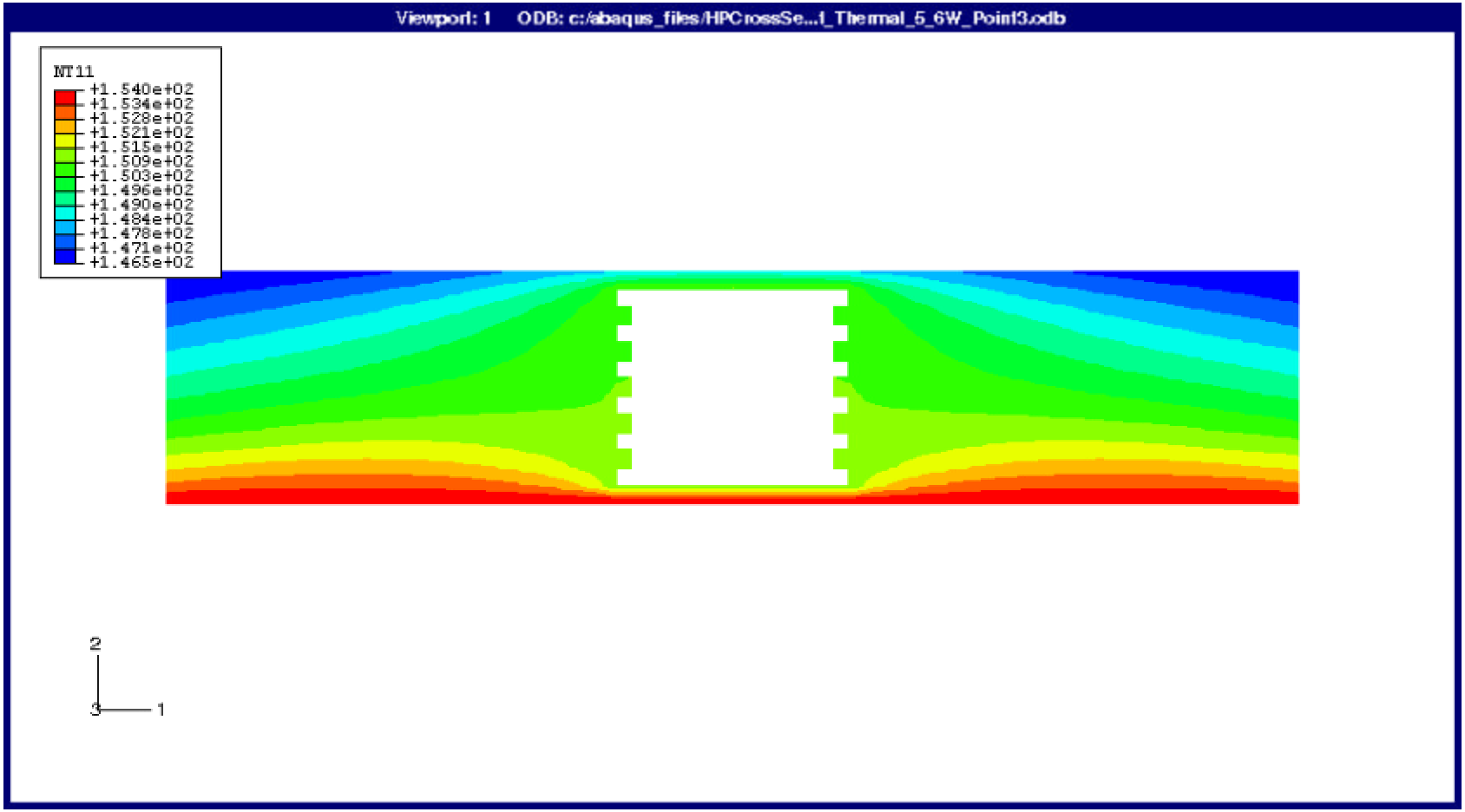

Figure 4.33 Temperature Distribution at point T3 with 5.6 W of input power.

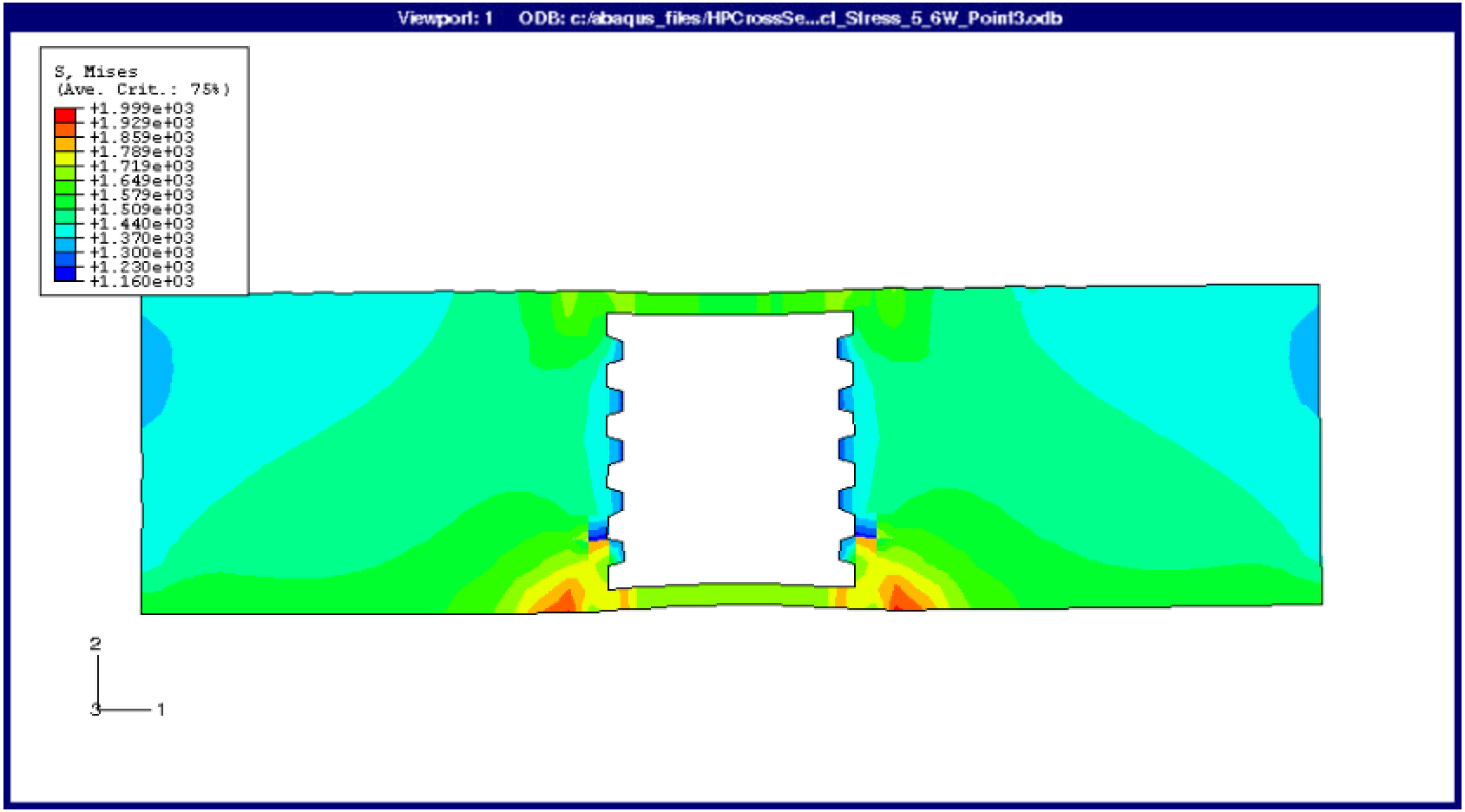

Figure 4.34 Mises stress at point T3 with 5.6 W of input power.

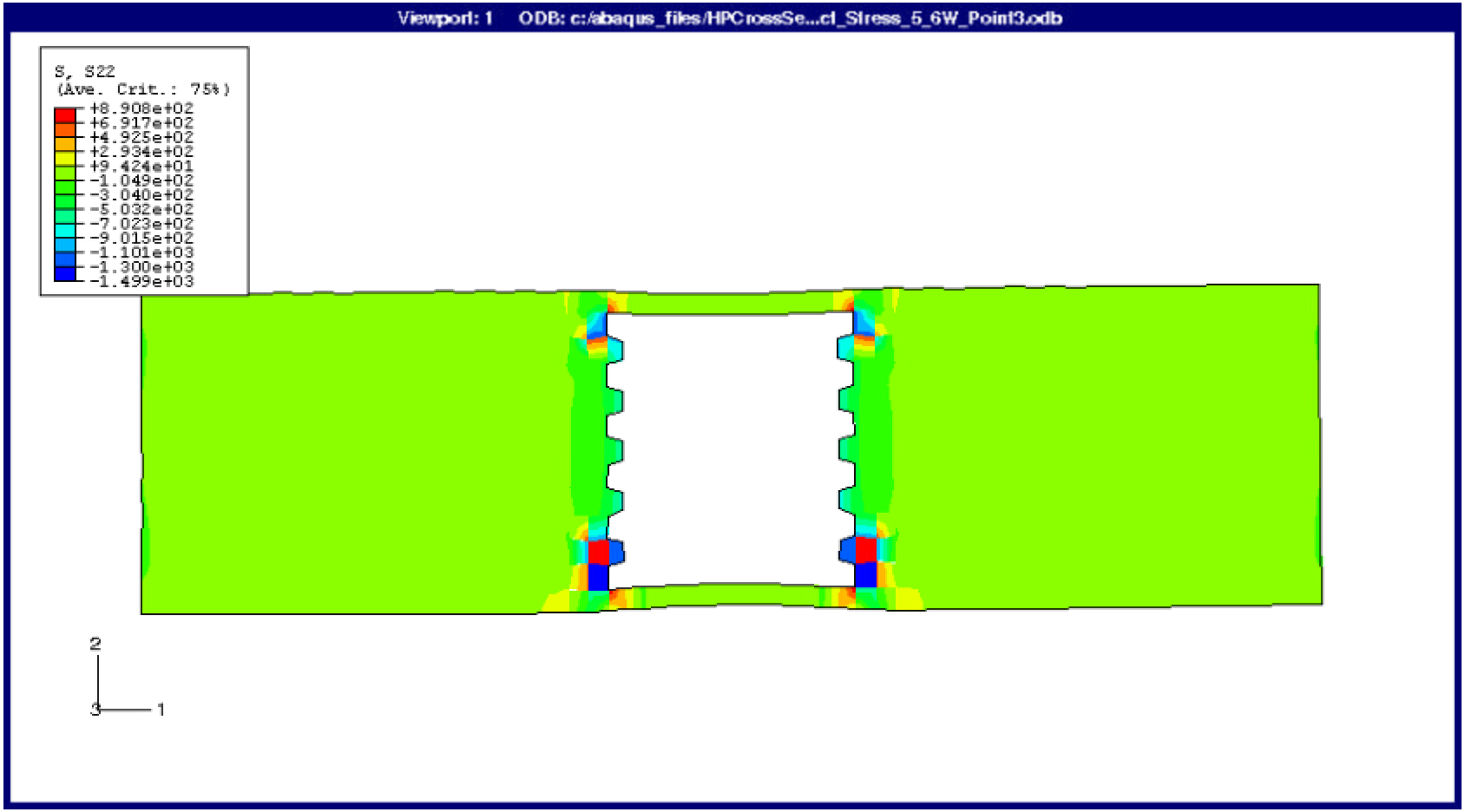

Figure 4.35 S22 stress at point T3 with 5.6 W of input power.

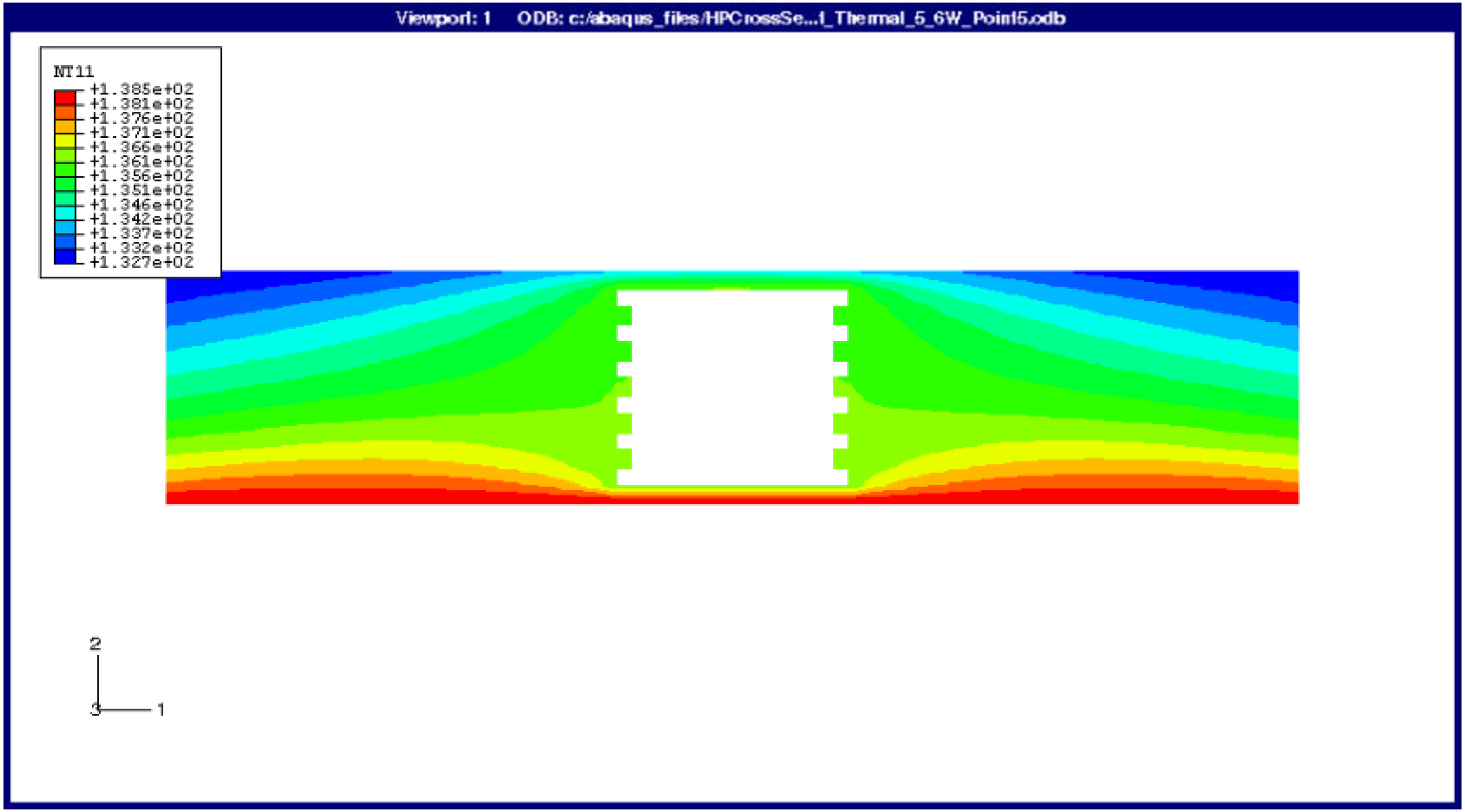

Figure 4. 36 Temperature Distribution at point T5 with 5.6 W of input power.

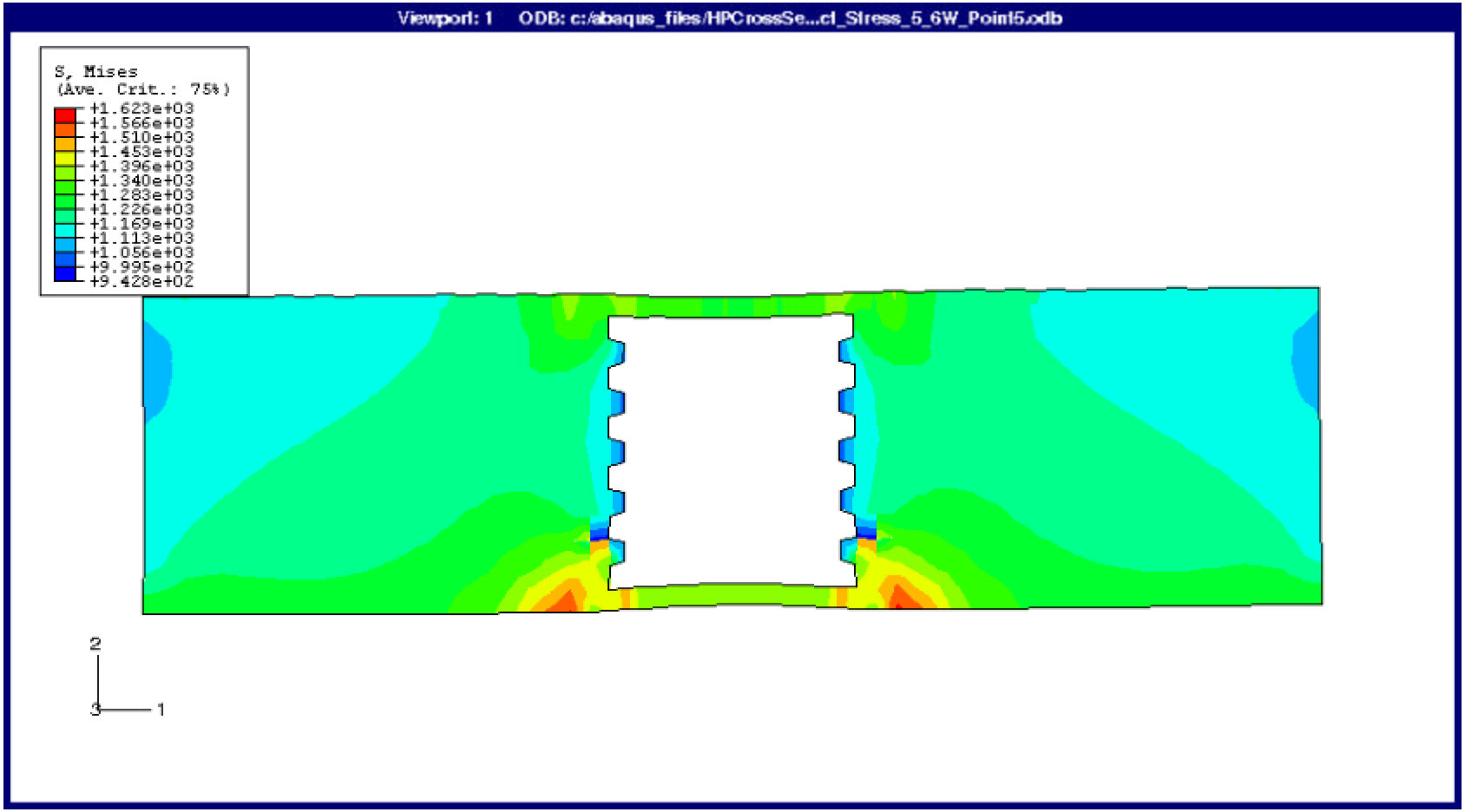

Figure 4.37 Mises stress at point T5 with 5.6 W of input power.

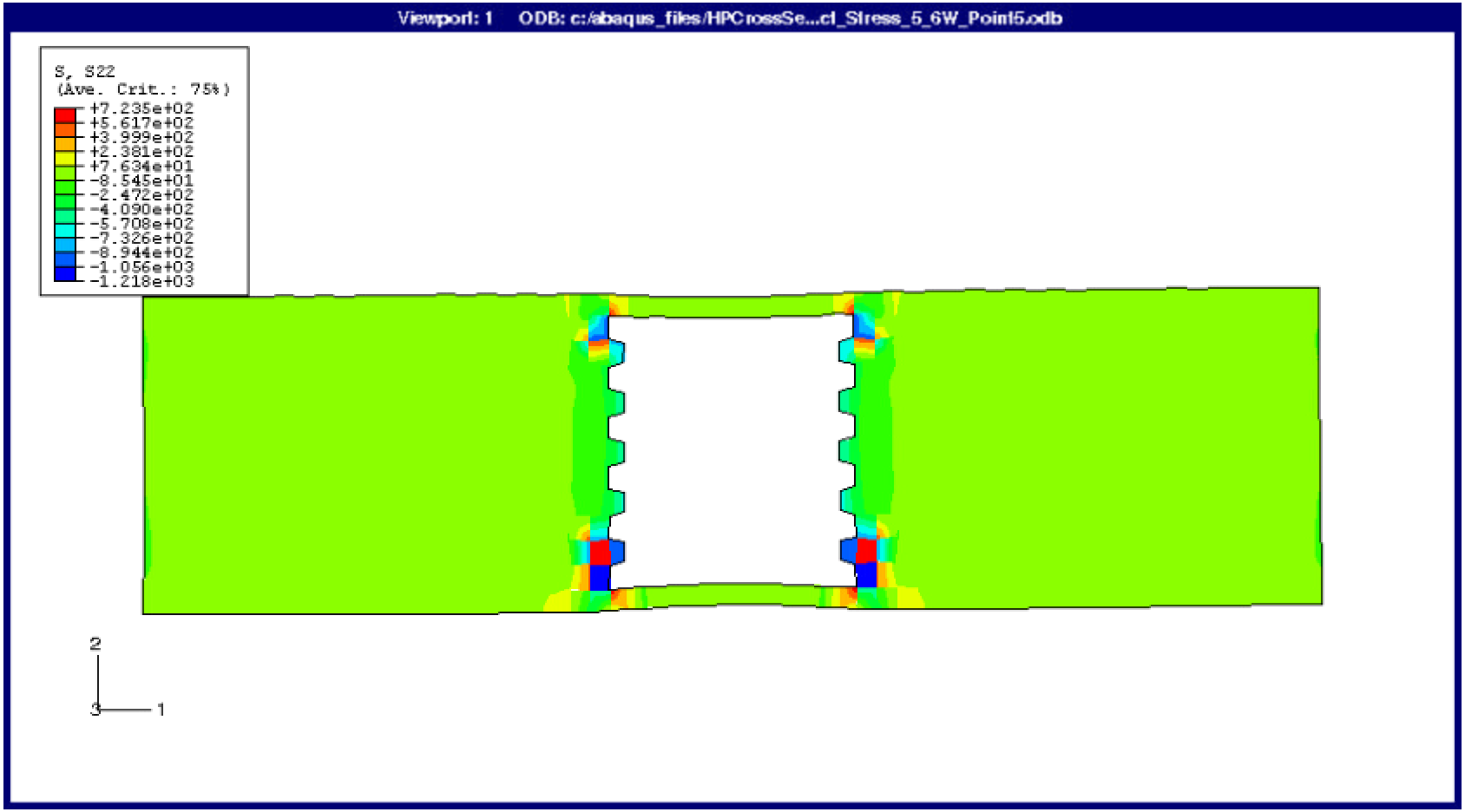

Figure 4. 38 S22 stress at point T5 with 5.6 W of input power.

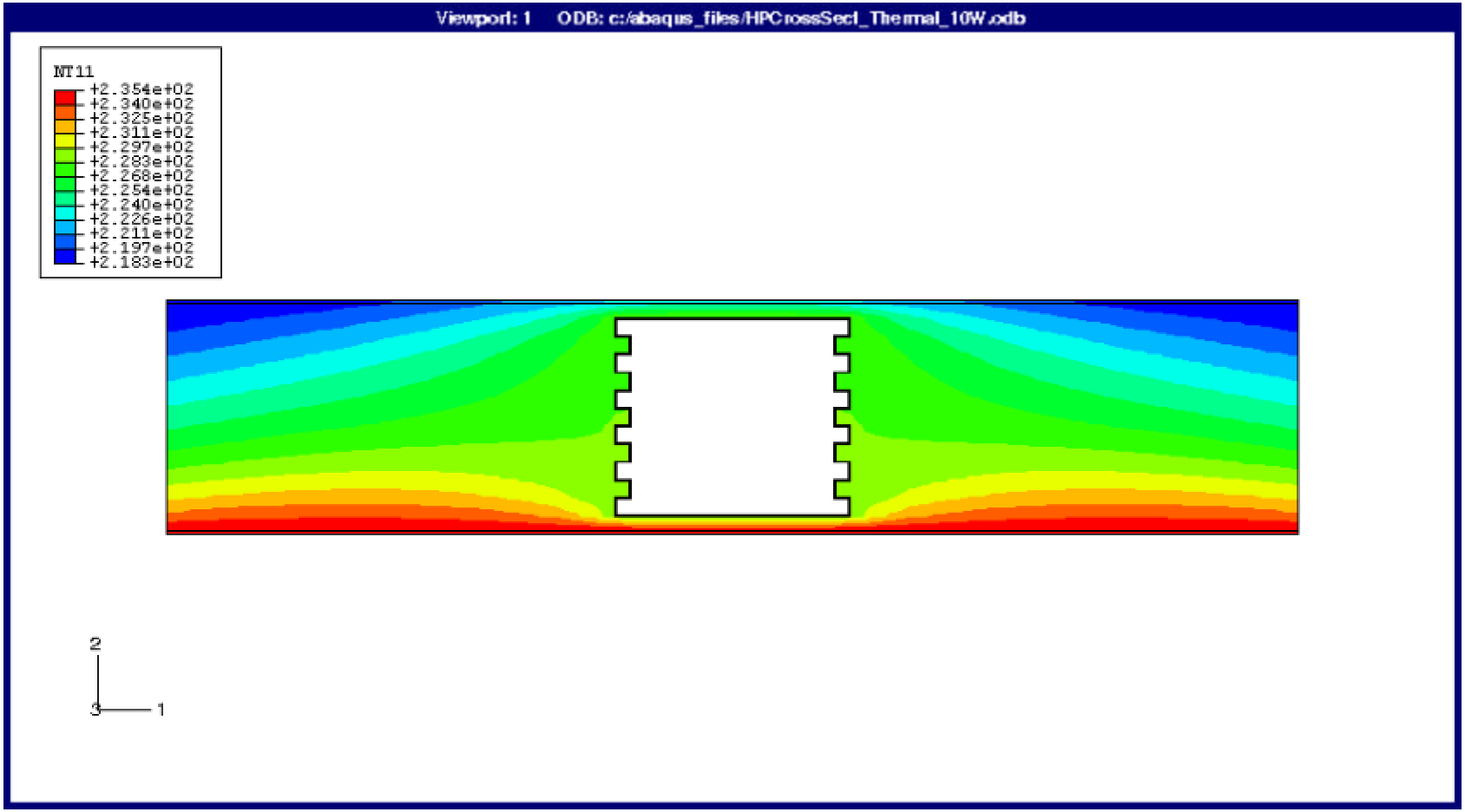

Figure 4.39 Temperature Distribution at point T1 with 10 W of input power.

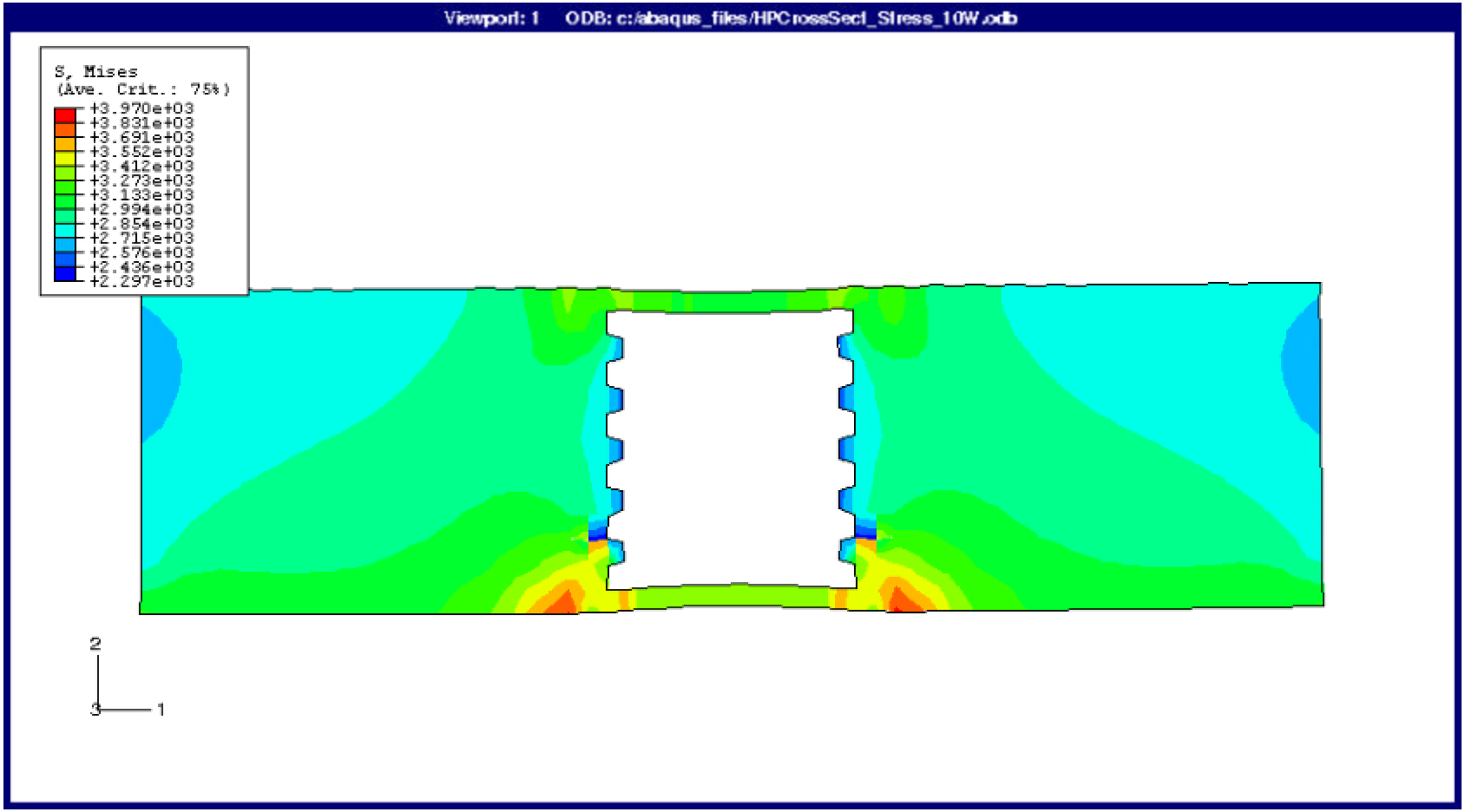

Figure 4.40 Mises stress at point T1 with 10 W of input power.

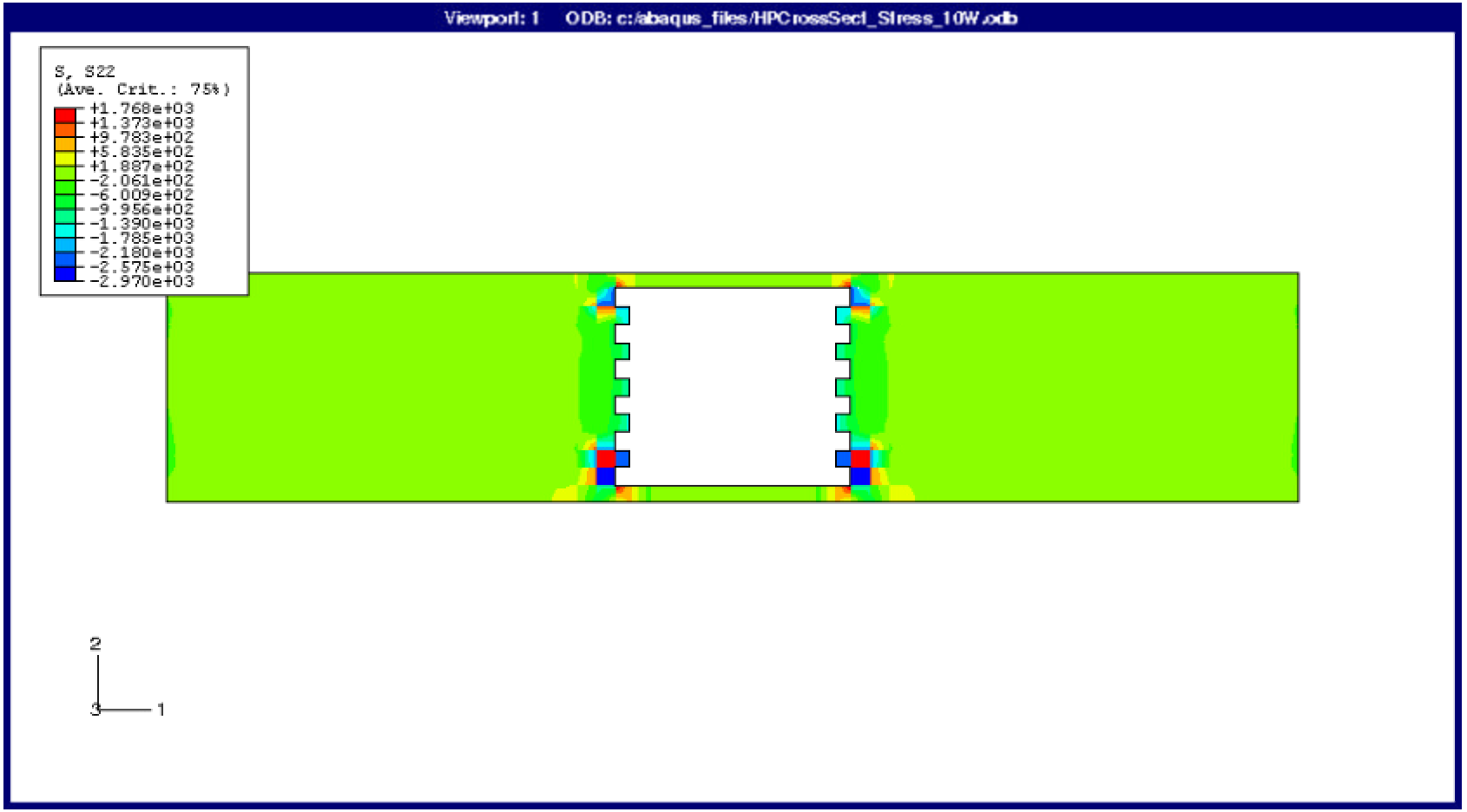

Figure 4.41 S22 stress at point T1 with 10 W of input power.

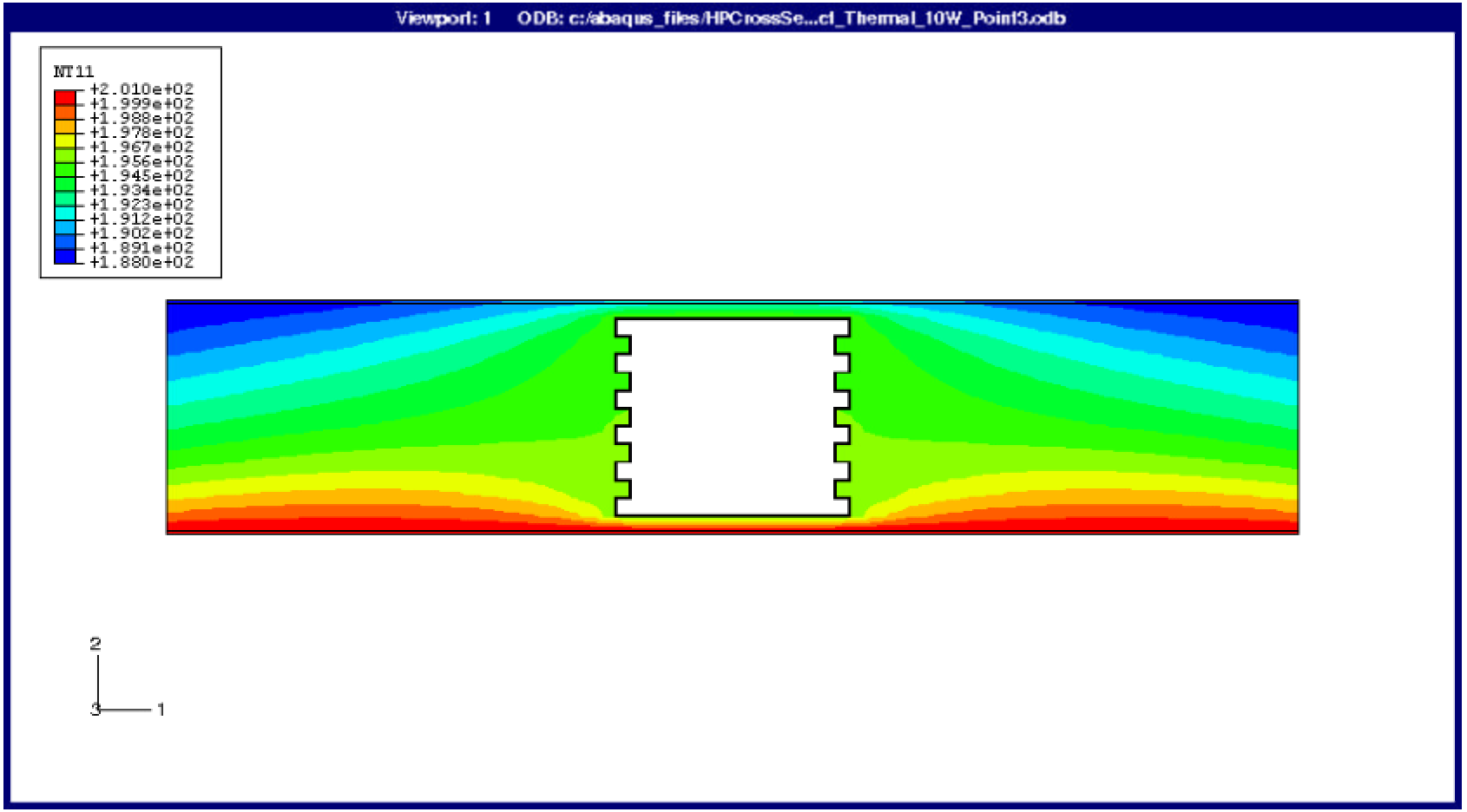

Figure 4.42 Temperature Distribution at point T3 with 10 W of input power

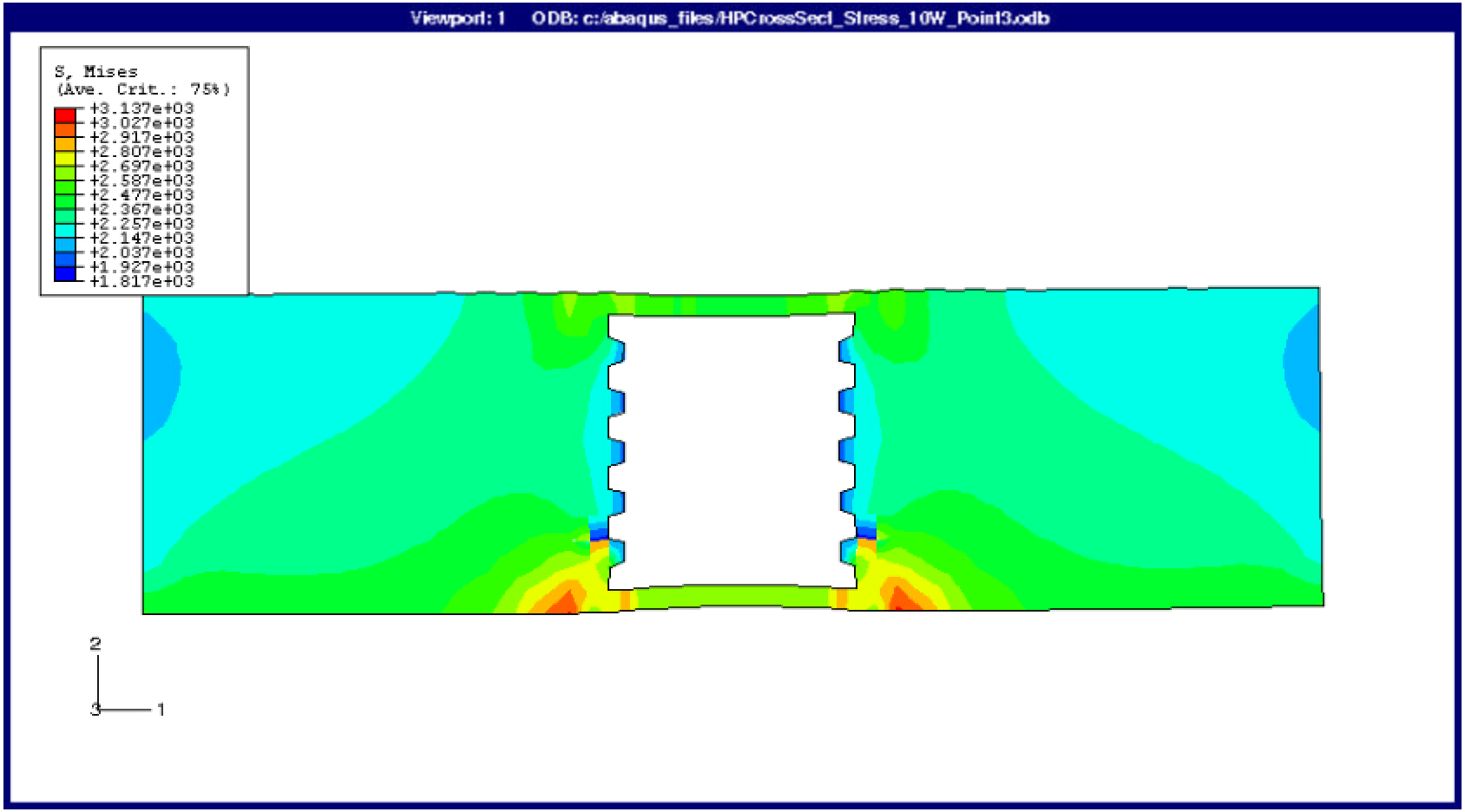

Figure 4.43 Mises stress at point T3 with 10 W of input power.

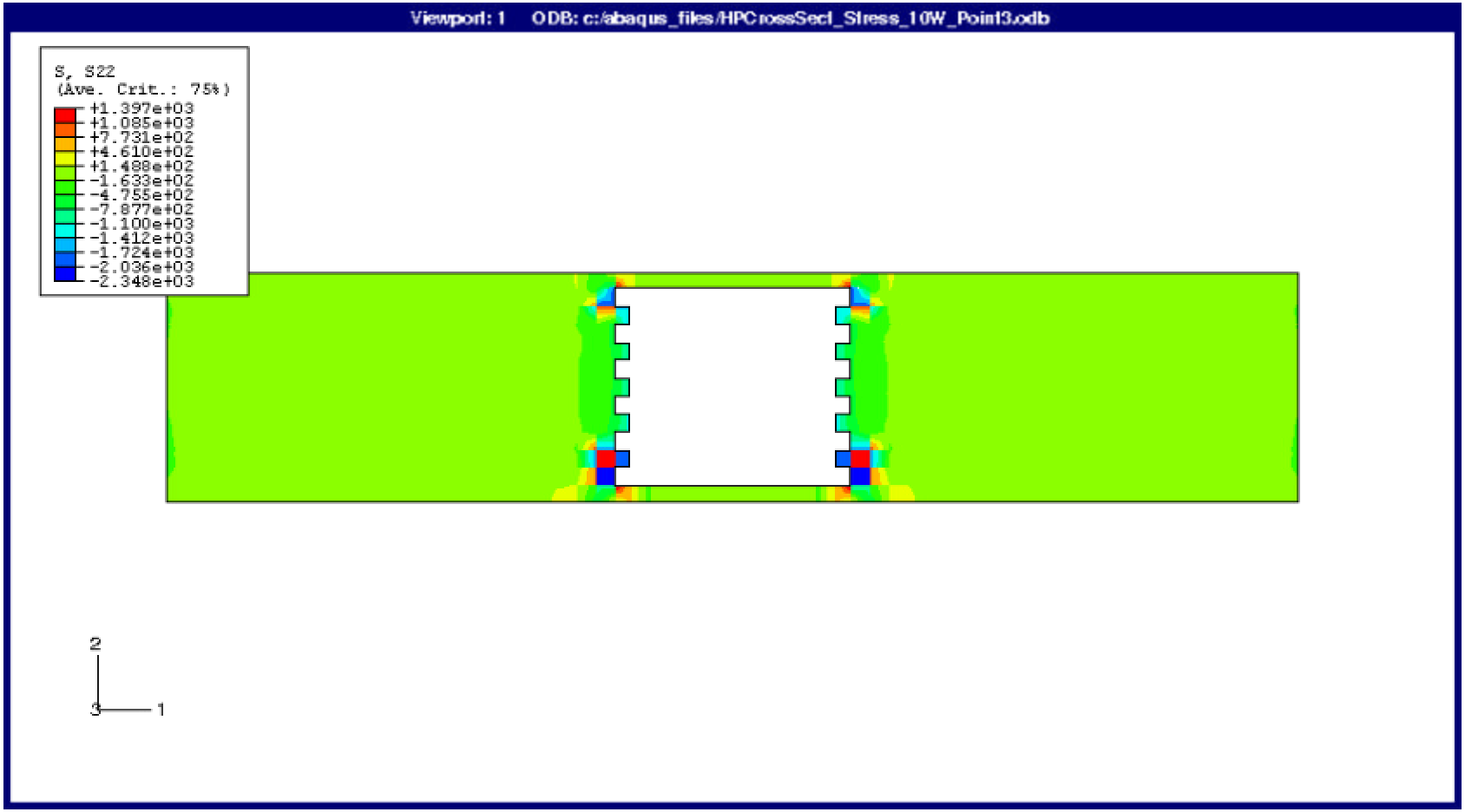

Figure 4.44 S22 stress at point T3 with 10 W of input power

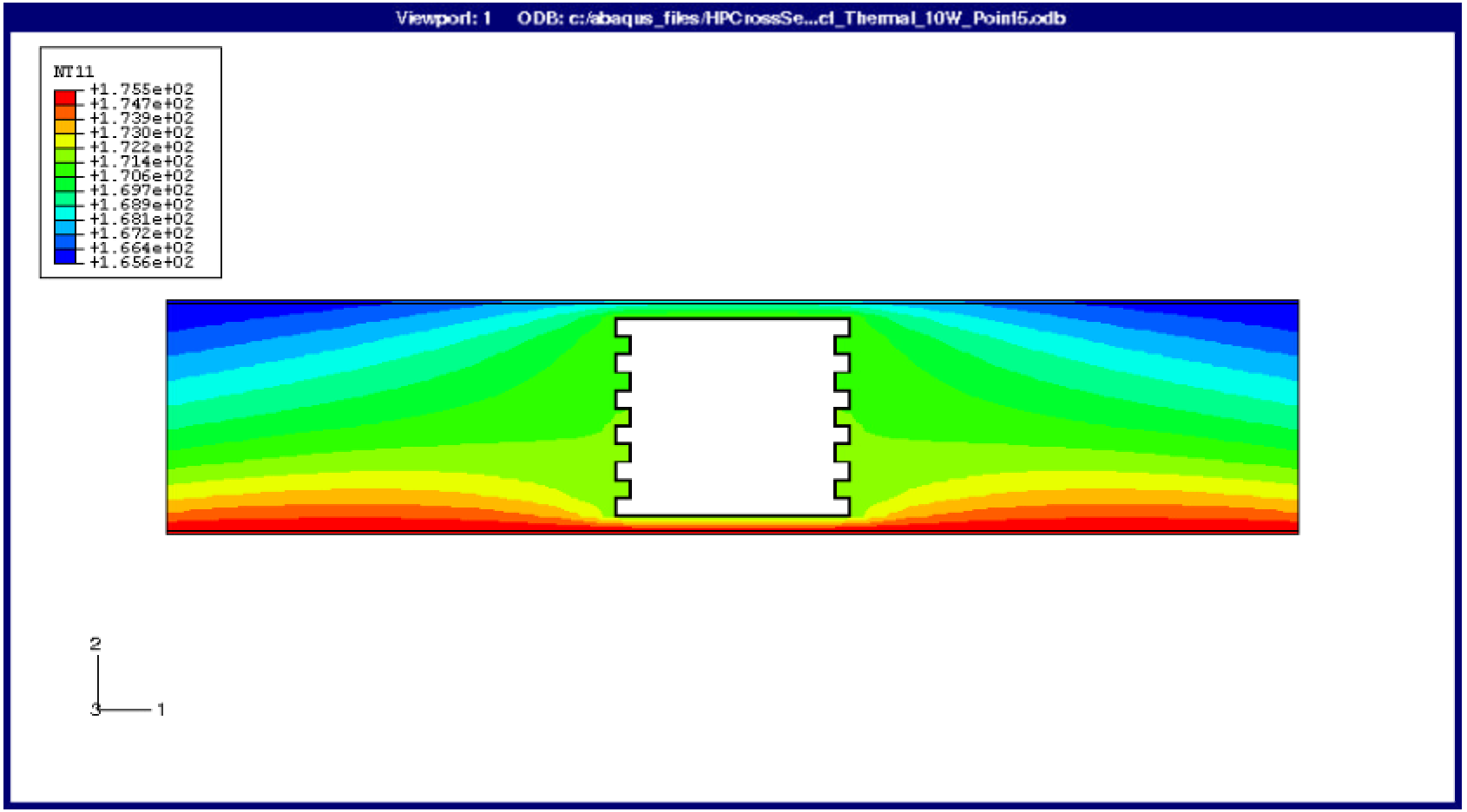

Figure 4.45 Temperature Distribution at point T5 with 10 W of input power.

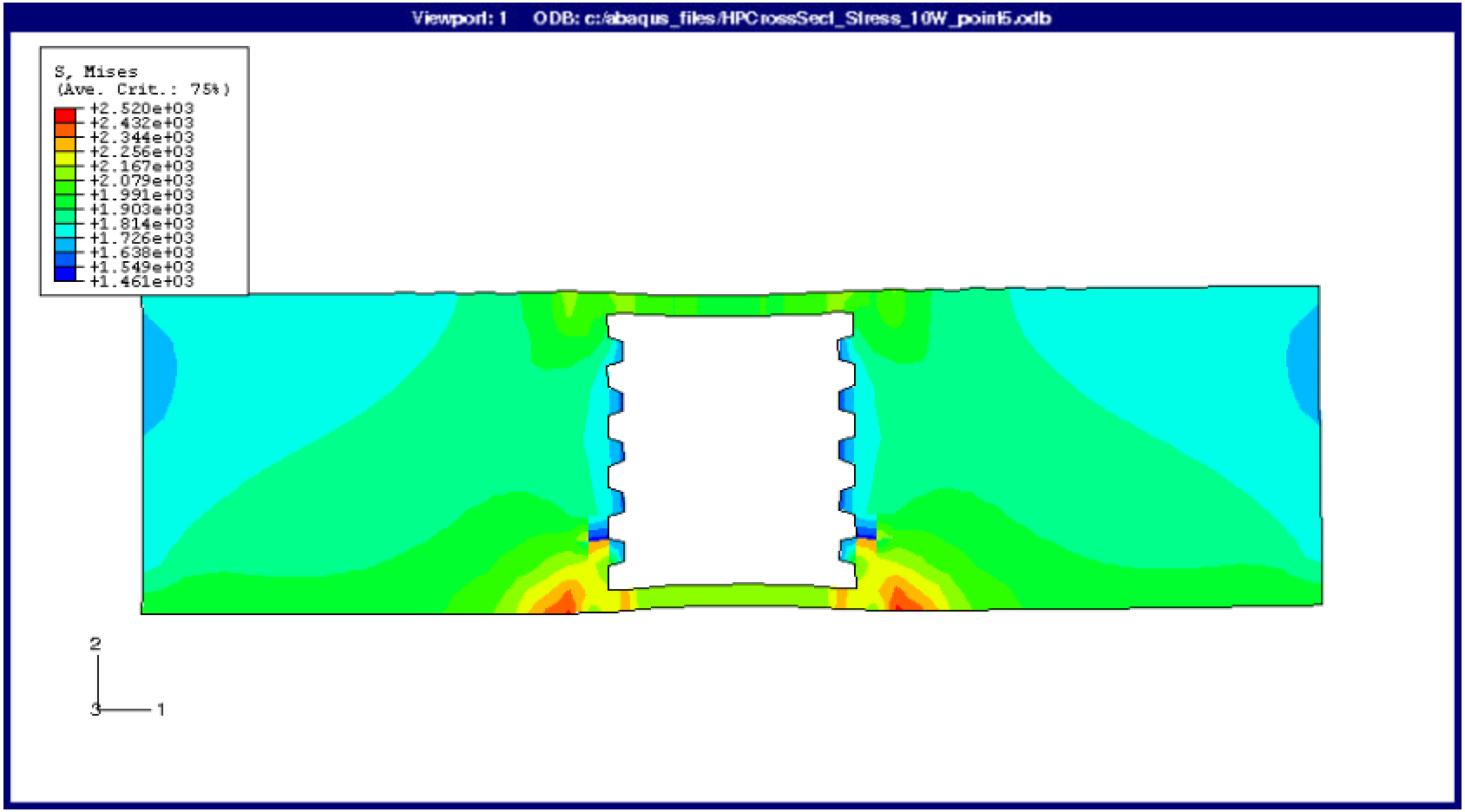

Figure 4.46 Mises stress Distribution at point T5 with 10 W of input power

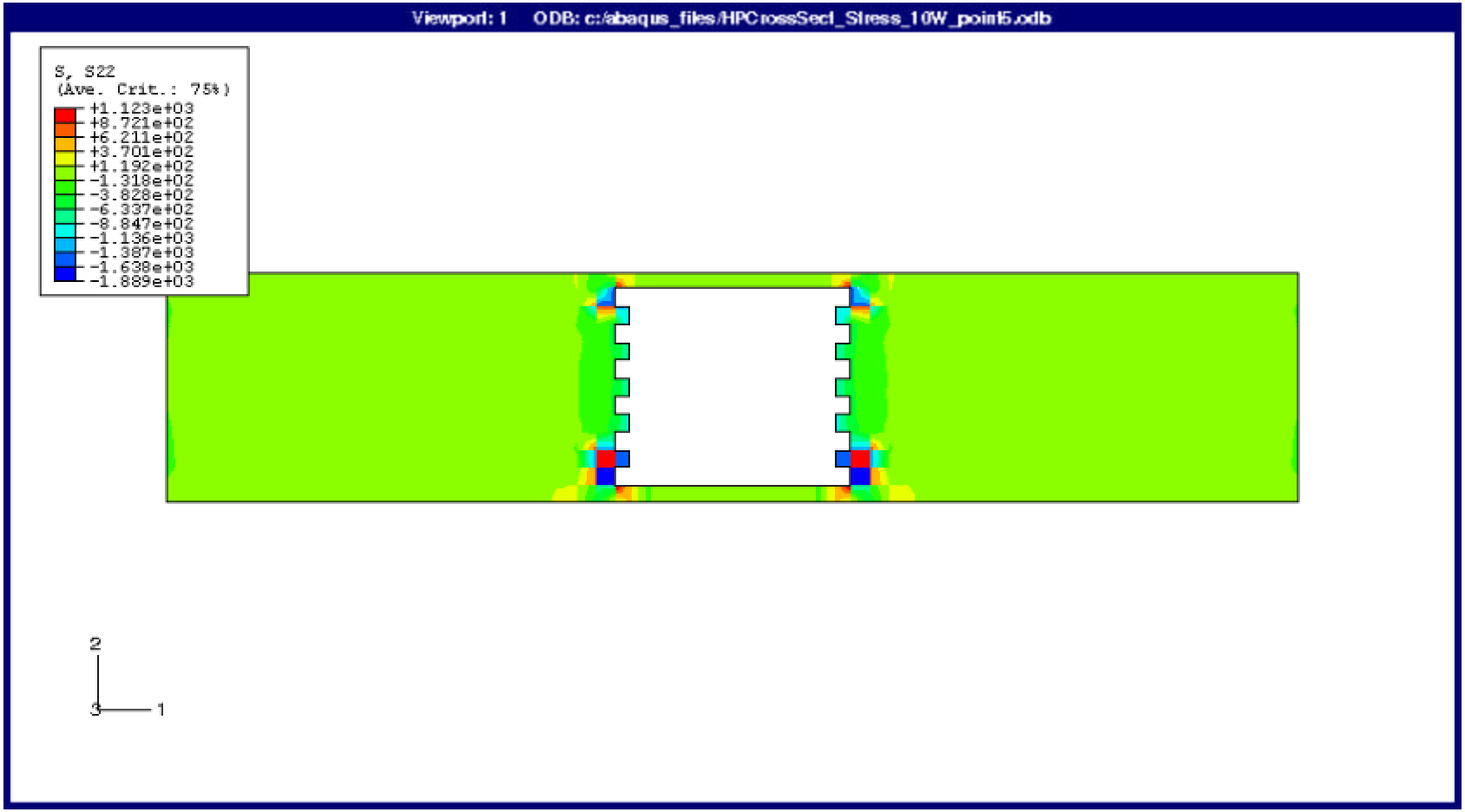

Figure 4.47 S22 stress Distribution at point T5 with 10 W of input power

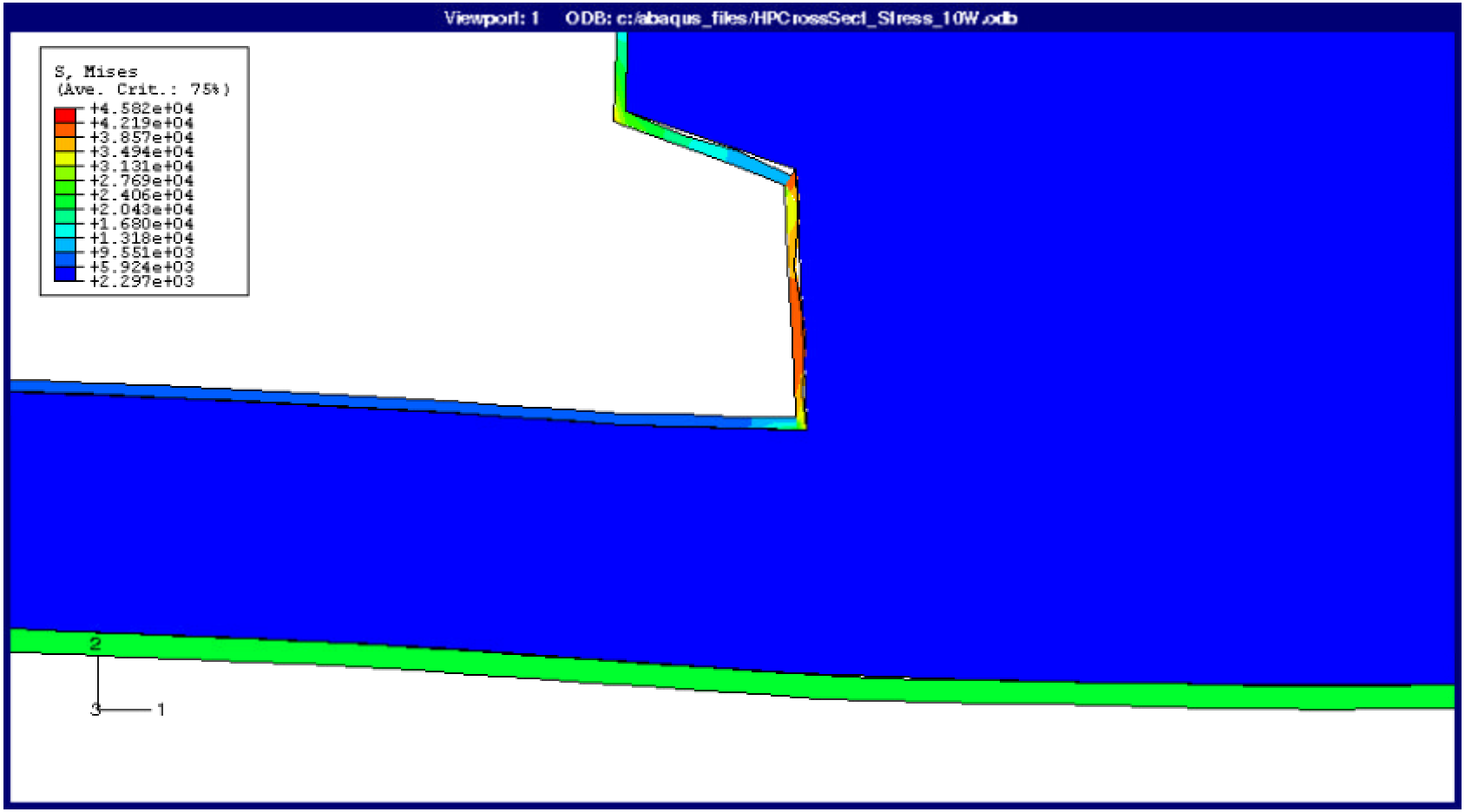

Figure 4.48 Maximum stress in the copper plating with 10 W of input power..

Table 4.5 Maximum temperature and stresses in the substrate (FR-4) cross-section with 2.5 W of input power.

Cross Section at Point	**Temperature (^{o}C)**	**Mises Stress (psi)**	**S11 (psi)**	**S22 (psi)**
T1	51	1234	319	550
T2	44	980	253	437
T3	41	807	208	360

Table 4.6 Maximum temperature and stresses in the substrate (FR-4) cross-section with 5.6 W of input power.

Cross Section at Point	**Temperature (^{o}C)**	**Mises Stress (psi)**	**S11 (psi)**	**S22 (psi)**
T1	81	2563	666	1142
T2	68	1999	518	891
T3	59	1623	420	724

Table 4. 7 Maximum temperature and stresses in the substrate (FR-4) cross-section with 10 W of input power.

Cross Section at Point	**Temperature (^{o}C)**	**Mises Stress (psi)**	**S11 (psi)**	**S22 (psi)**
T1	113	3970	1035	1768
T2	94	3137	817	1397
T3	79	2520	655	1123

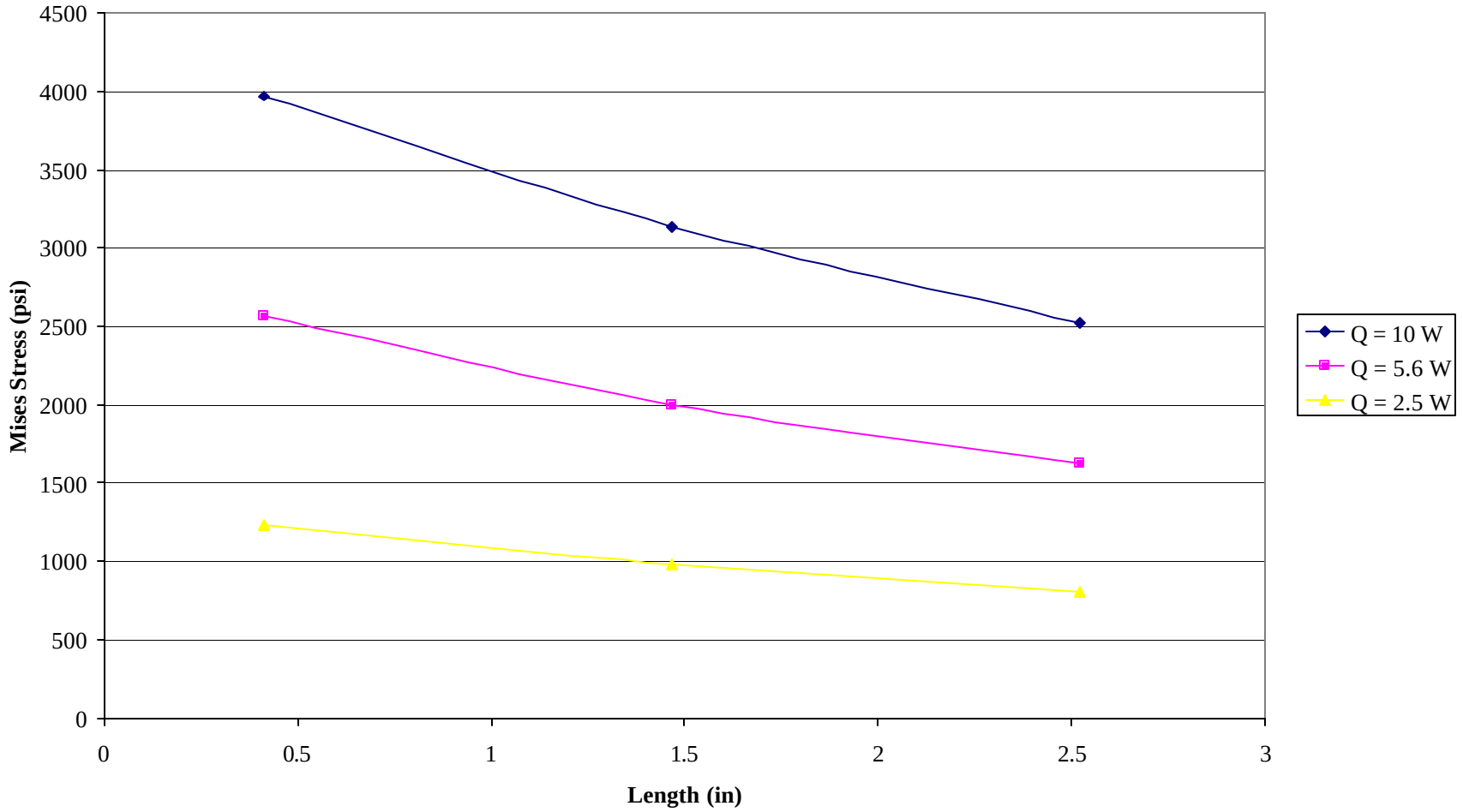

Figure 4.49 Substrate maximum Mises stresses along embedded heat pipe length.

Appendix A

PTH Chemistry

Wear protective clothing and face shield when handling chemicals. Always add acid to water, slowly; never the reverse. Fuming and heat will occur when mixing. Avoid breathing fumes

Step # 1 - Chemical Cleaner: CCH-3, 3.5G, PTH Cleaner

Pour 71ml. of water into a beaker; add 29 ml. of concentrate.

Step # 3 - Copper Cleaner: AP-24 G, Ammonium Persulphate

Pour 850 ml. of hot water into a beaker; add 205 gr. of AP crystals. Stir until dissolved. To this solution, add 18 ml., Sulfuric Acid, H_2SO_4, Reagent Grade 95-98 %.

Step # 5 - Acid Tread: H_2SO_4, Sulfuric Acid, Reagent Grade 95-98 %

Pour 857 ml of water into a beaker; slowly add 143 ml of Sulfuric Acid.

Step # 7 - Acid Treat: HCL, Hydrochloric Acid, Reagent Grade 36.5-38.0%

Pour 714 ml. of water into a beaker; add 286 ml. of hydrochloric acid.

Step # 8 - Activator: ACT-1G, Activator

Used as supplied. Approximately 100 ml. required.

Step # 10 - Accelerator: ACC-3.5G, Accelerator

Pour 714 ml. of deionized water into a beaker; add 286 ml. of concentrate.

Step # 13 - Electroless Copper: ECU-10G, Electroless Copper, supplied as Part "A" and Part "B" concentrates

Pour 100 ml. of Part "A" into a beaker; add 800 ml. of deionized water; add 100 ml. of Part "B" (Mixture is 10% Part "A", 80 % DI water, 10% Part "B"; DO NOT mix parts "A" and "B" directly together).

Step # 15 - Acid Treat: H_2SO_4, Sulfuric Acid, Reagent Grade 95-98 %

Pour 929 ml. of water into a beaker; slowly add 71ml. of Sulfuric Acid.

Step # 16 - Copper Electroplate: CU-5G, Copper Electrolyte

Use as supplied, approximately 1000 ml.

REFERENCES

[1] G. P. Peterson, An Introduction to Heat Pipes, John Wiley & Sons, Inc, New York, NY, 1994.

[2] M. A. Zampino, "Embedded Heat Pipes in Cofired Ceramic Substrates for Enhanced Thermal Management of Electronics", Florida International University, Ph. D. Dissertation, Miami, Fl, 20001.

[3] A. Faghri, Heat Pipe Science and Technology, Taylor and Francis, Washington, DC, 1995.

[4] M. Zampino and W. K. Jones, "Substrate Embedded Heat Pipes Compatible with Cofire Processing", Proc. Int. Sym. Of Microelectronics, IMAPS, Philadelphia, 1997.

[5] S. Kakac, R. K. Shah, and W. Aung, Handbook of Single-Phase Convective Heat Transfer, Wiley, New York, NY, 1987.

[6] G. E. Schneider and R. Devos, "Nondimensional Analysis for the Heat Transport Capability of Axially-Grooved Heat Pipes Including Liquid/Vapor Interaction", A/AA Paper No. 80-0214, 1980.

[7] E. W. Washbum, Physics Review, Vol. 17, 1921, pp. 273.

[8] E. K. Rideal, Phil. Mag., Vol. 44, 1921, pp. 1152.

[9] ASM Handbook Committee, Metal Handbook: Surface cleaning, finishing, and coatings, 9th edition, vol. 5, 1978.

[10] J. E. Seargent and C. A. Harper, Hybrid Microelectronics Handbook, McGraw-Hill, New York, NY, 1995.

[11] Allied Signal Inc, FR404 GOLDLAM Epoxy Laminate and Prepreg / Processing Guide for Multilayers PWB, 1996.

[12] R. H. Clark, Handbook of Printed Circuit, Van Nostrand Reinhold, New York, NY, 1985

[13] Kepro Circuit Systems inc., Instructions for Kepro's BTF-144PTH(E) Plate-Thru Facility, 1997

[14] W. D. Callister, Jr., Material Science and Engineering: an Introduction, 5th edition, John Wiley & Sons, inc., New York, NY, 2000.

[15] TANTEC, CAM-MICRO Series of Contact Angle Meters, Procedure Guide, 1998.

[16] Y. Cao, M. Gao, and E. Pinilla, “Fabrication and Test of Filling Station for Micro/Miniature Devices”, 32nd Intersociety Energy Conversion Engineering Conference, Honolulu, HI, Part 2 (of 4), 1997, pp. 1509.

[17] Hibbit, Karlsson & Sorenson, Inc., “ABAQUS/Standard User’s Manual”, Volume One, Version 6.1, 2